The Greenhouse Effect

Solar radiation powers the climate system.

Some of the infrared radiation passes through the atmosphere but most is absorbed and re-emitted in all directions by greenhouse gas molecules and clouds. The effect of this is to warm the Earth's surface and the lower atmosphere.

Some solar radiation is reflected by the Earth and the atmosphere.

ATMOSPHERE

EARTH

About half the solar radiation is absorbed by the Earth's surface and warms it.

Infrared radiation is emitted from the Earth's surface.

SUN

Cover Photographs

Upper: An idealized model of the natural greenhouse effect [source: IPCC Fourth Assessment Report 2007]

Lower: Canadian Light Source Synchrotron facility, Saskatoon, Saskatchewan, Canada [source: Canadian Light Source Inc.]

SPECTROSCOPIC STUDY OF CHANNEL SPECTRA PHENOMENA IN THE SYNCHROTRON-BASED FTIR SPECTROMETER AT THE CANADIAN LIGHT SOURCE

Amr Ibrahim

B.Sc. in Physics, Cairo University, Beni Suef Campus, Egypt, 2003
M.Sc. in Physics, Beni Suef University, Egypt, 2008

A Thesis

Submitted to the School of Graduate Studies

of the University of Lethbridge

in Partial Fulfilment of the

Requirements of the Degree

Master

Of

Science

Department of Physics and Astronomy

University of Lethbridge

Lethbridge, Alberta, Canada

Abstract

Recently, the high radiance of synchrotron sources was used to enhance FTIR spectrometer performance. However, excessive channel spectra when synchrotron sources are used degrade the quality of retrieved spectral parameters. In the research reported in this thesis, seven different techniques for handling channel spectra were investigated. These techniques were used to reduce channel spectra for a test group of seven samples of CO_2 mixed with air recorded using the synchrotron source at the Canadian Light Source. The increases in signal to noise ratio (SNR) of spectra handled with each technique were calculated. SNR results showed that transmission spectra, produced using synthetic background spectra with simulated channel spectra, achieved the highest SNR improvement. However, when the spectra groups were fitted using nonlinear least square fit algorithm, the technique using channel spectra fitting produced the smallest fitting residual. Moreover, the retrieved intensities and air broadening coefficients of 21 spectral lines showed that the spectral fitting technique produced the most accurate values as compared to the HITRAN 2008 database. Although the spectral fitting technique was accurate in retrieving spectral line parameters, applying the technique at wider spectral ranges was less accurate.

A modification to the channel spectra fitting technique by performing iterations of channel fitting was introduced to process wider spectral ranges. Carbon dioxide laser band I centred at 961 wavenumber was analyzed using 24 spectra recorded under different experimental conditions. The intensity and air-

and self-broadening coefficients were retrieved for 48 spectral lines with average deviations from HITRAN database values of 2.11%, 1.25% and 4.14%, respectively, using the Voigt profile. These average deviations lie within the uncertainty limits listed by the database. The deviation between our results and other results reported in the literature were also examined and it is found to be also within the range of HITRAN uncertainties. The effect of errors in fitting channel spectra parameters was examined and found to be mitigated by the inclusion of channel-free spectra in the multispectral fit.

Acknowledgements

I owe the completion of this thesis to both the help and the support of many individuals. First, I have to thank Dr. Adriana Predoi-Cross for her help in facilitating my transition to the graduate program at University of Lethbridge and also for her guidance, supervision and patience during my thesis work. During my thesis work Dr. Predoi-Cross introduced me to the research laboratory at the Far-Infrared beam in the Canadian Light Source (CLS), which was an important step in building my research abilities and my knowledge of spectroscopic research and its applications. I must also thank my Co-Supervisor Dr. Philippe Teillet for his inspirational teaching of remote sensing, which was my first introduction to this field of science. He was always willing to give me advice to guide my research.

I would like also thank Dr. Brant Billinghurst at the CLS, for his guidance and patience especially when I began my research at the CLS. Also, I wish to thank our group research collaborator Dr. Malathy D. Venkataraman at the College of William and Mary in Virginia, USA for help in answering my many questions about the spectral fitting program even if it is trivial. Last but not least, I would like to thank my colleague Chad Povey for his help in guiding me when I was new to our research group and I would like to thank Sheila Matson our Physics department previous administrative assistant for always being helpful and supportive.

Content

List of Tables

List of Figures

List of Acronym Definitions

ACE-FTS	Atmospheric Chemistry Experiment - Fourier Transform Spectrometer
AFGL	Air Force Geophysics Laboratory (vibrational band notation)
AIRS	Atmospheric Infrared Sounder
CAI	Cloud and Aerosol Imager
CLS	Canadian Light Source
CSR	Coherent Synchrotron Radiation
FOV	Field of View
FTIR	Fourier Transform Infrared Spectroscopy
FTS	Fourier Transform Spectrometer
FWHM	Full Width Half Maximum
GB	Globar source
GEISA	Gestion et d'Etude des Information Spectroscopiques Atmospheriques (Management and Study of Spectroscopic Information)
GOSAT	Greenhouse gases Observing Satellite
HCFC	Hydro-chlorofluorocarbon
HITRAN	High Resolution Transmission
IASI	Infrared Atmospheric Sounding Instrument
IPCC	Intergovernmental Panel on Climate Change
ISAI	Infrared Atmospheric Sounding Interferometer
LabVIEW	Laboratory Virtual Instrument Engineering Workbench
LLGHGs	Long Lived Green House Gases
OCO	Orbiting Carbon Observatory

OPUS	Optical User's Software (Bruker Optics)
ppm	part per million
SCIAMACHY	Scanning Imaging Absorption Spectrometer for Atmospheric Cartography (Greek analogous is "Fighting Shadows")
SNR	Signal to Noise Ratio
SPD	Speed-dependent Voigt Profile
SR	Synchrotron Source
STDV	Standard deviation
SWIR	Short-Wave Infrared
TIR	Thermal Infrared
UHV	Ultra High Vacuum

"Science tells us not only that the climate system is changing, but also that further warming and sea level rise is in store even if greenhouse gases were to be stabilized today. That is a consequence of the basic physics of the system[1]"

R. K. Pachauri/ Chairman of the Intergovernmental Panel on Climate Change (IPCC)

Chapter 1: Spectroscopic remote sensing of greenhouse gases

1.1: Introduction

As expressed in the above quote from the 2007 Nobel peace lecture, it is now an established fact that the Earth's atmospheric composition has changed considerably since the industrial revolution in the 18th century. This striking change became well documented through the study of the permanent polar ice, which has acted as a memory for the Earth's atmosphere by capturing and trapping, for centuries, atmospheric air samples within its layers [1]. The analysis of this chronological record of earth atmosphere has proven that many greenhouse gases concentrations have risen dramatically during the last two centuries of human civilization [see figure (1.1)].

The greenhouse effect is not a new discovery. The discovery of this effect is credited to the research of the French Mathematician Fourier in 1827 [2]. Ironically, Fourier transform spectroscopy is currently one of the main techniques used in monitoring greenhouse gases. However, the effect of greenhouse gases produced by human activities on Earth's climate was not investigated until the end of the 19th century by Swedish physicist Arrhenius [3]. Undoubtedly, such discoveries have

---

[1] From The 2007 Peace Nobel Lecture
"http://nobelprize.org/nobel_prizes/peace/laureates/2007/ipcc-lecture_en.html"

escalated global concerns about different greenhouse gases and their possible effects and have motivated scientists to study the sources of these gases by developing new techniques or enhancing the existing ones to provide an accurate estimation for their diurnal/seasonal variations and long-term changes [4]. Appreciation for this research was evident through the awarding of the 2007 Nobel Prize to the United Nation Intergovernmental Panel on Climate Change (IPCC) and Al Gore for their activities in studying and advocating awareness of climate change.
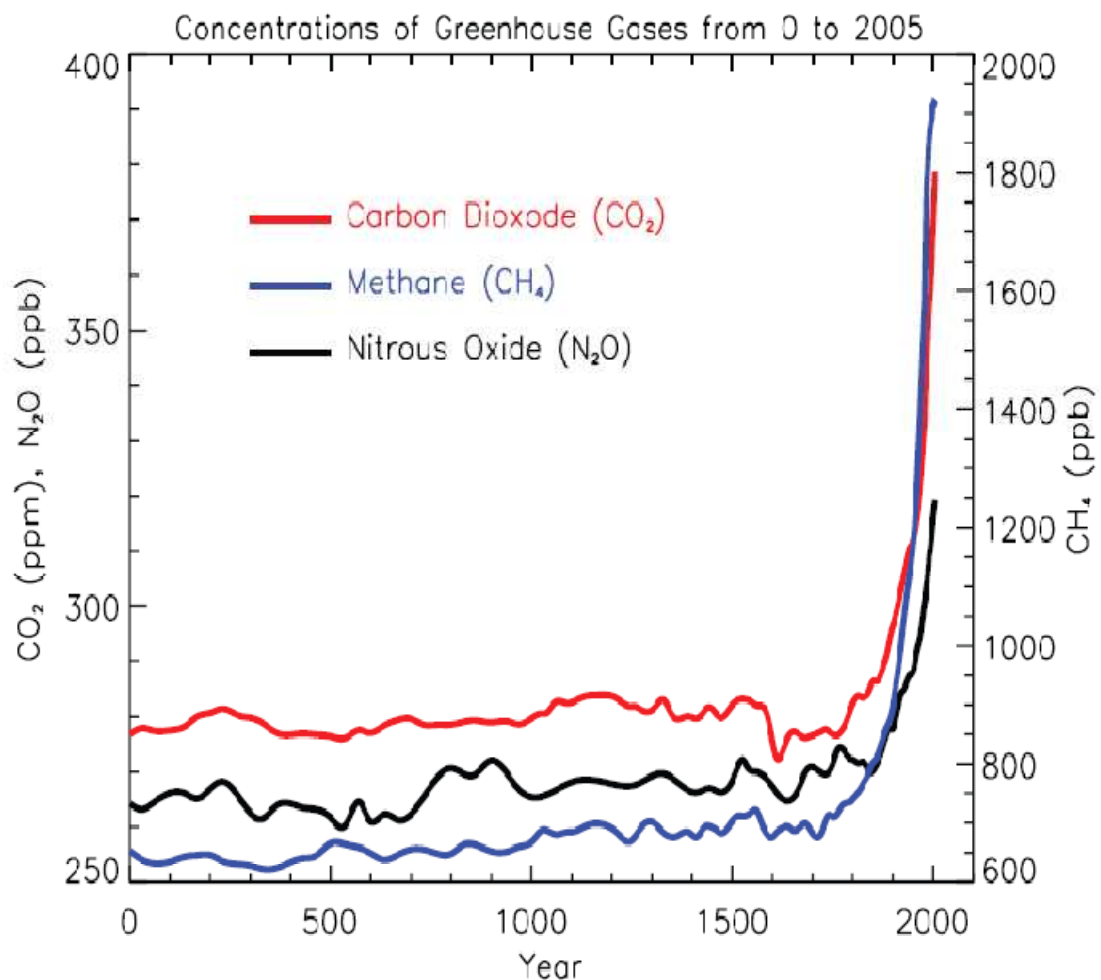
Figure (1.1): Atmospheric concentration for long-lived greenhouse gases (LLGHGs) over the last 2,000 years [5].

The increasing efforts to monitor the atmospheric composition aim to understand the atmospheric system and its changes, such as the increase of greenhouse gases, loss of stratospheric ozone, poor air quality, or acid rain [6]. These studies will eventually help the international community and its decision-making bodies by providing estimates or predictions for this urgent atmospheric issue. This atmospheric monitoring is performed from different platforms (ground-based or space-borne) by employing different techniques. The most widely used technique for atmospheric monitoring is optical remote sensing [6]. The reason for the popularity of these spectroscopic techniques[2] is related to both their accuracy and ability to provide wide temporal and spatial coverage when performed from a space platform. Table (1.1) shows a brief survey of spaceborne instruments capable of measuring greenhouse gases such as carbon dioxide (published by the committee on Methods for Estimating Greenhouse Gas Emissions, National Research Council in 2010) [7].

Optical remote sensing of the atmosphere can be summarized as a technique utilizing the interaction of electromagnetic waves with atoms, molecules or other particles (such as aerosols as an analytical tool for identification and/or quantization of the atmospheric composition [4]. Therefore, the study of spectroscopy aims to develop a better understanding of spectroscopic phenomena and/or to enhance the accuracy of the spectroscopic analysis and measurements. It is of great importance for understanding and quantifying changes in our atmosphere that could affect our lives.

---

[2] Note that optical and spectroscopic techniques are often used interchangeably in literature and in this thesis.

Table (1.1): Specification of spaceborne instruments capable of measuring CO_2 [7].

Specification	OCO[3]	GOSAT[4]	SCIAMACHY[5]	AIRS[6]	IASI[7]
Measured Gases	CO_2, O_2	CO_2,CH_4,O_2, O_3, H_2O	O_3,O_4,N_2O,NO_2 CO,CO_2,H_2O,So_2 HCHO	CO_2,CH_4,O_3, CO,H_2O	CO_2,CH_4,O_3, CO,H_2O, SO_2,N_2O
IFOV[8]/Swath millirad/km	1.29x2.25/ 5.2	FTIR:10.5 /80-790	30x60/960	15/1650	12/2200
Viewing mode	Nadir, glint, target	Nadir, glint, target	Limb, Nadir	Nadir	Nadir
Instrument	3-channel grating spectrometer	CAI, SWIR/TIR FTIR spectrometer	8-channel grating Spectrometer	Grating Spectrometer	FTIR Spectrometer
Wavelength Band pass(μm)	0.757-0.772, 1.59-1.62, 2.04-2.08	0.758-0.775, 1.56-1.72, 1.92-2.08, 5.56-14.3	0.24-0.44, 0.4-1.0, 1.0-1.7, 1.94-2.04, 2.265-2.38	3.74-4.61, 6.20-8.22, 8.80-15.4	3.62-5.0, 5.0-8.26, 8.26-15.5
SNR(Nadir, 5% albedo)	>300@1.59-1.62 μm >240@2.04-2.08 μm	~120@1.56-1.72 μm ~120@1.92-2.08 μm	<100@1.57 μm	~2000@1.56μm ~1400@3.7-13.6μm ~800@13.6-15.4μm	~1000@12μm ~500@4.5μm
Orbit altitude	705km	666km	790km	705km	820km
Samples/day	500,000	18,700	8,600	2,916,000	1,296,000
Revisit time/ orbits	16 days/233 orbits	3 days/72 orbits	35 days	16 days/233 orbits	72days/ 1,037 orbits
Launch date	Failed to launch	January 2009	March 2002	May 2002	October 2006
Nominal life	2 Years	5 years	7+ Years	7+ Years	5 Years
CO_2 Sensitivity	Total Column including near surface	Total Column including near surface	Total Column including near surface	Mid-troposphere	Mid-troposphere
CO_2 Uncertainty[9]	1-2	4	14	1.5	2

AIRS is Atmospheric Infrared Sounder; **ISAI** is Infrared Atmospheric Sounding Interferometer; **CAI** is Cloud and Aerosol Imager; **GOSAT** is Greenhouse gases Observing Satellite; **OCO** is Orbiting Carbon Observatory; **SCIMACHY** is Scanning Imaging Absorption Spectrometer for Atmospheric Cartography; **SWIR** Short-Wave Infrared; **TIR** is Thermal Infrared.

---

[3] Source: references [8, 9]
[4] Source: references [7],[10, 11]
[5] Source: http://envisat.esa.int/instruments/sciamachy/ , and references [12, 13]
[6] Source: references [14, 15]
[7]Source: references [16, 17]
[8] Instantaneous field of view
[9] It represent an estimation of random errors (e.g. detector noise)while systematic errors (e.g., bias caused by cloud and aerosol) are not included or eliminated by validation for more details see ref.[7]

1.2: Optical Remote Sensing Techniques

The term "Remote Sensing" implies that information about an object is collected via a sensor that is not located in proximity to the object. However, the term "Optical" does not necessarily imply that only the visible range of the electromagnetic radiation spectrum is used in such measurements. The term *optical remote sensing* is used in the literature for remote sensing employing infrared (IR), visible and ultraviolet (UV) wavelengths [4]. In all these spectral regions, optical remote sensing utilizes the same principle, which is electromagnetic wave interactions with the target particles or molecules, to infer useful information about the target or its environment. If the targets are greenhouse gases, then in general optical remote sensing techniques use the absorption of electromagnetic radiation for the purposes of identification and quantifying of the absorber.

These absorption spectroscopic measurements not only target absorption line intensities to calculate the concentration of the targeted gas species, but also use the shape of these absorption lines to gather information regarding their environment, such as their temperature and pressure. This multifunction ability makes optical remote sensing not only a vital technique in quantifying atmospheric trace gases[10] but also an equally important technique in gathering information about the pressure and temperature profile of the atmosphere for meteorological applications. Therefore, a knowledge of line parameters such as intensity, broadening and shift is essential for remote sensing of atmospheric trace gases. The accuracy of these parameters is even important throughout different spectral

---

[10] Trace gases are gases that exist with small concentration in the atmosphere, including greenhouse gases.

ranges, otherwise a comparison between different instruments operating with different spectral ranges will be of limited value [6]. For example, the ozone is measured either in the infrared at 10 microns or in the two ultraviolet regions at 300-350 and 253.7 nm, which requires accurate line intensities in both spectral ranges to achieve agreement in retrieved concentrations [18, 19].

Interpretation of observed spectroscopic measurements from either ground or space-based instruments relies on the availability of accurate spectroscopic parameters such as line intensity, line position, self- and air-pressure shift, self- and air-broadening parameters and their temperature dependence. Regardless of the technique used to measure the spectra of the atmosphere, either using natural sources of radiation (sun, moon, star ....) or using artificial sources of radiation (lasers or thermal sources), the analysis of such data is usually similar. A radiative forward model is used to reconstruct the spectra using spectroscopic parameters from databases such as HITRAN [20], ATMOS [21] or GEISA/IASI [22] databases, information about the physical conditions (temperature, pressure, etc.) and settings of the measuring device (path length, field of view, etc). The retrieving of accurate gas concentrations, which is one of the main goals of atmospheric remote sensing, is subjected to the full uncertainty of the employed line intensities. This uncertainty cannot be minimized by a fitting algorithm since line intensity has to be fixed as it is inextricably linked to concentration [23].

1.3: Vibrational-Rotational Spectroscopy

In order to understand the effects of spectral line parameters on retrieving concentrations of greenhouse gases, a brief description of the theory and principles of vibrational-rotational spectroscopy is necessary. The reason that vibrational-rotational spectroscopy is so vital to atmospheric gases monitoring systems stems from the fact that all gas molecules (except diatomic homonuclear ones) have at least one allowed infrared rotational-vibrational band [24]. The interaction of molecules with infrared radiation can be attributed to the vibration of atoms within such molecules. Molecules with N atoms possess 3N degrees of freedom, three representing transitional motions and three representing rotation around the x- , y- and z-axes. The remaining 3N-6 degrees (3N-5 in case of linear molecules since rotating around bond axis do not displace any atoms) are vibrational modes. It can be approximate that the vibration of the atoms is harmonic and potential energy V(r) of this oscillator is a function of the internuclear distance r. If the atoms vibrate in simple harmonic motion, it will follow Hook's law and vibrational energy states will be given by the relation:

$$E_i = hc\omega_i(v_i + {}^1\!/_2) \tag{1.1}$$

where ω_i is the mode fundamental frequency in wavenumbers, v_i is the vibrational quantum number of the ith mode (v_i=0, 1, 2, ...), h is Planck's constant in Joule/sec and c is the speed of light in cm/sec. The transition intensity between vibrational states is proportional to the square of the transition moment between lower and upper states with vibrational wave functions ψ_v'' and ψ_v', respectively, which is given by the following equation:

$$R_v = \int \psi_v'^* \, \mu \, \psi_v'' dx \qquad (1.2)$$

where x is the internuclear displacement from equilibrium and μ is dipole moment. Equation (1.2) introduces the principle that only molecules with non-zero dipole moment have allowed infrared vibrational transitions.

The dipole moment of the molecule changes with diatomic displacement causing the interaction between the incident radiation electric field and the molecule dipole. This change can be expressed in terms of the diatomic internuclear displacement as a Taylor series expansion:

$$\mu = \mu_e + \left(\frac{d\mu}{dx}\right)_e x + \frac{1}{2!}\left(\frac{d^2\mu}{dx^2}\right)_e x^2 + \cdots \qquad (1.3)$$

where e is the equilibrium configuration. Since the internuclear displacements are small it is an acceptable approximation to ignore the higher power terms of internuclear distance x in equation (1.3), which leads to harmonic potential following Hook's law as shown in figure (1.2). Applying this harmonic approximation to equation (1.3) and substituting in equation (1.2) will lead to transition moment:

$$R_v = \left(\frac{d\mu}{dx}\right)_e \int \psi_v'^* \, \mu \, \psi_v'' dx \qquad (1.4)$$

where both ψ_v'' and ψ_v' are the eigenfunctions of the same energy Hamiltonian making equation (1.4) only non-zero if

$$\Delta v = \pm 1 \qquad (1.5)$$

which is the vibrational selection rule. However if equation (1.3) contains higher power terms of the internuclear displacement x, this leads to an anharmonic

8

potential instead of a harmonic one (Hook's law) [see figure (1.2)]. This type of anharmonicity it is called the electrical anharmonicity since it is associated with the electrical dipole moment [25]. This anharmonicity has the effect of modifying the vibrational selection rule to $\Delta v = \pm 1, \pm 2, \pm 3, \dots$ These newly allowed modes are called vibrational overtones. However, as a consequence of the higher powers of x associated with their terms in equation (1.3), their intensity is quite small compared to the main vibrational mode. Another limitation for this harmonic approximation arises from the limitation of Hook's law to small internuclear displacement. At large internuclear displacement the molecule dissociates and the single atoms repel each other due to the charges of the electrons. This effect also causes deviation from the harmonic shape of the potential energy and is called mechanical anharmonicity [25], which also contributes to overtones. Due to this mechanical anharmonicity the vibrational energy states become closer with increasing vibrational quantum number v, in comparison to those of the harmonic oscillator [see figure (1.2)]. Therefore, the vibrational energies described by equation (1.1) are modified to

$$E(v) = \omega_e[(v + 1/2) - x_e\left(v + \frac{1}{2}\right)^2 + y_e(v + \frac{1}{2})^3 + \cdots] \qquad (1.6)$$

where ω_e is the vibration wavenumber for a classical harmonic oscillator and the terms $\omega_e x_e$, $\omega_e y_e$, … are anharmonic constants [25]. The convergence limit of the vibrational energy states with increasing vibrational quantum number is called the dissociation energy D_e. The dissociation energy D_e is the energy at which the molecule dissociates into neutral atoms and energy becomes a continuum while the quantized vibrational states cease to exist. These differences between the idealized

harmonic oscillator potential and that of the actual vibrational potential led to the

introduction of a new potential function given by [26]

$$V(r) = D_e(1 - e^{-\beta(r-r_e)}) \qquad (1.7)$$

where β is a constant characteristic to the particular electronic state of the

molecule, and r and r_e are the internuclear distance and the equilibrium

internuclear distance, respectively.
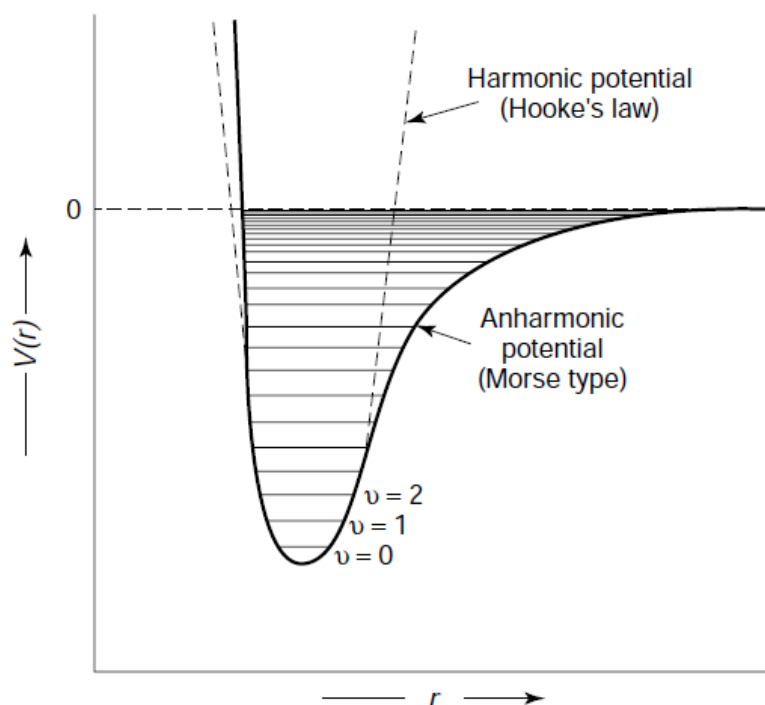
Figure (1.2): Potential energy of diatomic molecule as function of internuclear displacement for harmonic and anharmonic oscillator [27].

When molecules in the gas phase absorb energy and make a transition

between vibrational states, rotational energy transition also occurs. Therefore, the

high resolution absorption spectrum for vibrational transition in low pressure gases

is not a line but rather a resolved group of closely separated lines. For this reason,

the term "absorption line" is reserved for a rotational transition while the

10

vibrational transition takes the "absorption band" term. In order to study this rotational motion like the vibrational one, we start with another useful approximation and assume that the bond length is fixed (rigid rotor approximation). In this case the rotational energy is quantized and given by [25]

$$E_r = \frac{h^2}{8\pi\mu r^2} J(J+1) = BJ(J+1) \qquad (1.8)$$

where J is the rotational quantum number $J = 0,1,2,....$, μ is the reduced mass of the molecule and B is the rotational constant. The transition intensity is proportional to the square of the transition moment, which is similar to that given by equation (1.2), leading to the following selection rule:

$$\Delta J = \pm 1 \qquad (1.9)$$

This selection rule give rise to the P-branch ($\Delta J = -1$) and the R-branch ($\Delta J = +1$) as shown in figure (1.3). However, the selection rule was derived on the assumption that there is no additional vibrational, orbital, or spin angular momentum available. That is, Σ vibronic states are assumed. The complete derivation and description of this selection rule can be found in reference [24, p.171-172]. If there is an additional angular momentum such as in the case of Π vibrational or electronic states [24, p.171-172], there will be a Q-branch located at the band centre between the P-branch and the R-branch as shown in figure (1.3). A close examination of figure (1.4) shows that the lines in the R-branch converge and in the P-branch diverge. However, equation (1.8) and selection rule (1.9) indicate that the line spacing should be constant and equal to 2B.
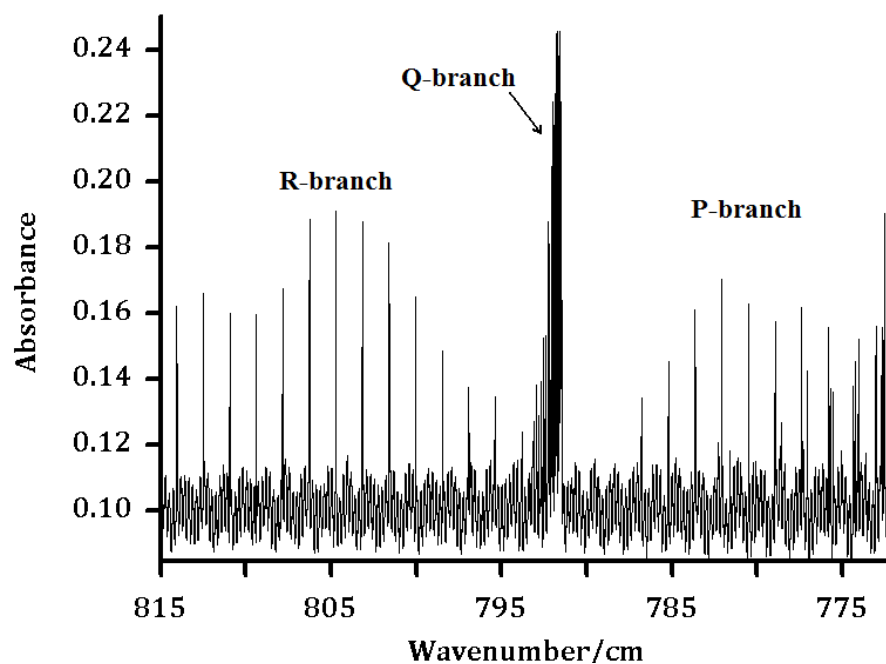
Figure (1.3): Section[11] of CO_2 11101←10002 vibrational band.[12]
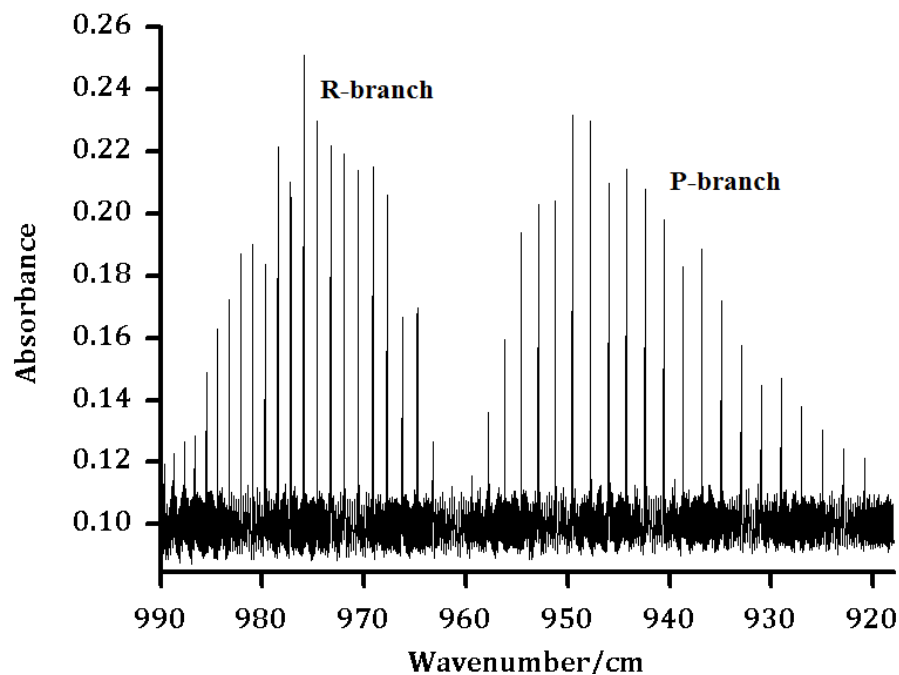
Figure (1.4): Section of CO_2 00011 <------- 10001 vibrational band.

[11] From spectrum recorded at the Canadian Light Source (CLS) Synchrotron.
[12] Band notations follow AFGL CO_2 notation [28] used in HITRAN 2008 database.

This deviation in the observed spectrum from the expected one can be attributed to the limitations of the rigid rotor approximation. The atomic bond is not rigid, so its length changes during vibration, changing the moment of inertia and, consequently, the rotation constant. This change in the bond is also induced by the centrifugal force resulting from rotation especially at high J values [see figure (1.5)]. To account for centrifugal distortion, equation (1.8) is modified to

$$E_r = BJ(J + 1) - DJ^2(J + 1)^2 \qquad (1.10)$$

where D is the centrifugal constant, and both B and D constants are slightly dependent on the vibrational quantum number. The relation between B and the vibrational quantum number v can be approximated by

$$B_v = B_e - \alpha(v + {}^1\!/_2) \qquad (1.11)$$

where B_e is the equilibrium rotational quantum number, which is a hypothetical state at the bottom of the potential curve in figure (1.2) [25] and α is the vibration-rotation interaction constant.
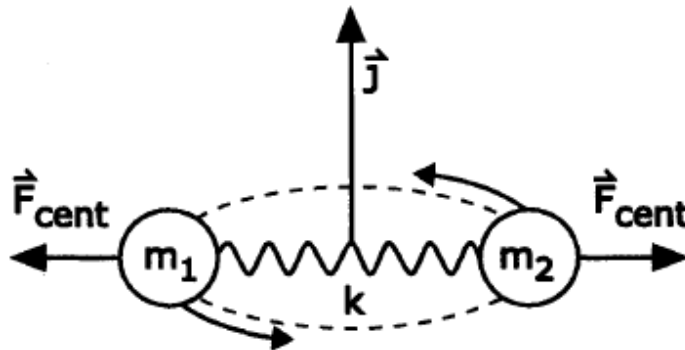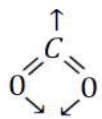
Figure (1.5): Non-rigid diatomic rotor with atoms connected via spring [24, p. 175].

The spectral lines in real molecular spectra rarely follow the predictions of equations (1.10) and (1.6). The deviations from these expected patterns are called by spectroscopists *perturbations* [24, P. 278-280]. For example, CO_2 has 3N-5=4 fundamental modes of vibration, which are described in table (1.2).

Table (1.2): Fundamental vibrational modes of carbon dioxide molecule.

No.	Vibrational mode	Band centre cm^{-1}	Remarks
ν_1	Symmetric stretch $\quad \overleftarrow{O} == C == \overrightarrow{O}$	(1285/1388)	IR-inactive Raman active
ν_2	bending (in the plane of the page) $\begin{array}{c} + \quad - \quad + \\ O= C =O \end{array}$	667	IR-active Raman inactive
ν_2	Bending (out of the plane of the page)	667	IR-active Raman inactive
ν_3	Anti-symmetric stretch $\quad \overleftarrow{O} == C = \overleftarrow{O}$	2349	IR-active Raman inactive

Symmetric stretch mode ν_1 has two band centres due to the accidental energy near-degeneracy between it and the overtone of the bending mode $2\nu_2$ [29]. The weaker overtone borrows intensity from the fundamental mode and two bands of similar intensity appear in the spectrum. Fermi [30] attributed this discrepancy to the fact that $2\nu_2$ and ν_1 have the same symmetry and in turn they have the same anharmonicity, therefore they perturb each other [31]. This kind of perturbation is known as Fermi resonance. A different type of perturbation, called Coriolis coupling, is due to the accidental near-degeneracy of vibration-rotational energies corresponding to the same rotational quantum number but different vibrational modes [24, P. 278-280].

14

The Fermi and Coriolis couplings result in extended notation systems to describe the vibrational transitions [32]. Two common notations which are generally found in literature are Herzberg [33] and American Air Force Geophysics Laboratory (AFGL) [28], with the latter being employed in the HITRAN database. The Herzberg notation for carbon dioxide uses 4 parameters written as (ν_1 $\nu_2^l \nu_3$), where ν_1, ν_2, ν_3 are vibrational quantum numbers and l is the angular momentum of the degenerate state ν_2. The quantum number l can take values ν_2-2, ν_2-4, ..., 1 or 0. The AFGL notation uses five parameters written as (ν_1 ν_2 l ν_3 r), where r is a ranking index. The ranking index is unity for the highest vibrational level of a Fermi resonating group and can take values of 1, 2, ..., ν_1+1. Table (1.3) shows the different notations for some CO_2 bands mentioned in this thesis and a complete list of CO_2 band notations can be found in reference [34].

Table (1.3): Examples of Herzberg and AFGL CO_2 band notations.

Band Centre (cm^{-1})	Herzberg ν_1 $\nu_2^l \nu_3$	AFGL ν_1 ν_2 l ν_3 r
791.447	$11^10 \leftarrow 02^00$	$11101 \leftarrow 10002$
960.959	$00^01 \leftarrow 10^00$	$00011 \leftarrow 10001$
1063.74	$00^01 \leftarrow 02^00$	$00011 \leftarrow 10002$

*Level 02^00 is in Fermi-resonance with level 10^00, therefore it is represented as 10002 in AFGL notation to indicate its resonance with level 10001.

The intensity of the vibrational-rotational lines is governed by the Boltzman distribution of the population in the initial state J'' according to the equation

$$\frac{N_{J''}}{N_0} = (2J + 1)\exp\left[-\frac{hcB''J''(J'' + 1)}{kT}\right] \qquad (1.12)$$

where h is Planck's constant, c is the speed of light in vacuum, k is Boltzmann's constant and T is the absolute temperature.

1.4: Beer's Law

The qualitative analysis of the recorded spectra to interpret and assign its absorption lines is important. However in applications like optical remote sensing, the quantitative analysis of the spectra to determine atmospheric trace gases concentrations is the main target. This target is achieved by employing Beer's law (also known as the Beer-Lambert law and the Beer-Lambert-Bouguer law), which expresses "the most important relationship in absorption spectroscopy" [35]. Pierre Bouguer (1698-1758) and Johann Heinrich Lambert (1728-1777) independently discovered that ''in homogeneous samples, the intensity of plane parallel monochromatic light entering a sample normal to the surface is diminished exponentially as the pathlength increase arithmetically" [35]. Several years later, August Beer (1825 – 1863) and F. Bernard developed the relationship between absorption and concentration independently [35].

To derive Beer's law, consider a volume system with length l [see figure (1.6)], which contain N_0 atoms in the ground state. If a flux of photons $F_0 = I_0/h\nu$ is incident on one side of the system and only absorption and stimulated emission are considered, the change in excited energy level E_1 population is given by [24, p. 19-21]:

$$\frac{dN_1}{dt} = -B_{1\to 0}\rho N_1 + B_{1\leftarrow 0}\rho N_0 \qquad (1.13)$$

where ρ is the radiation density (Joules/m³), and $B_{1\to 0}$ and $B_{1\leftarrow 0}$ are Einstein's coefficient to stimulated emission and absorption, respectively.
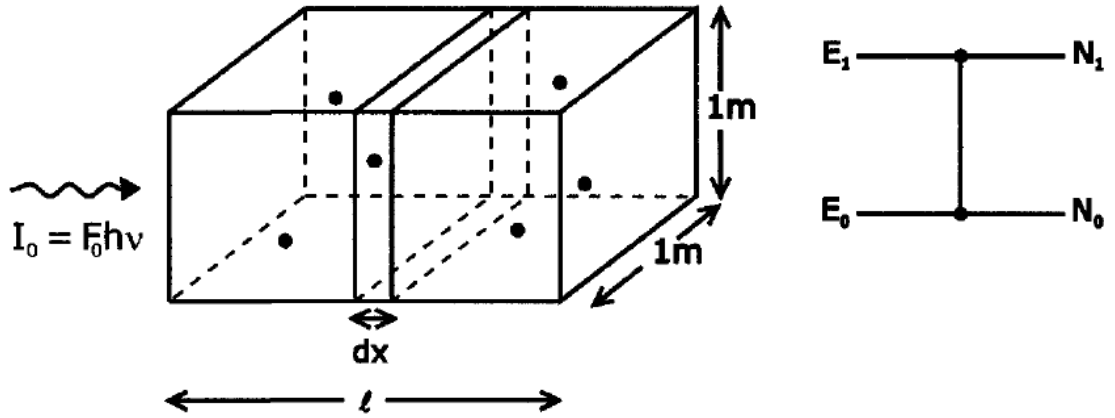
Figure (1.6): A volume system with dimensions 1 m x 1 m x l m [24, p. 19-21].

These coefficients are equal and related to the transition dipole moment μ_{10} by the following relation:

$$B_{1\rightarrow0} = B_{1\leftarrow0} = \frac{2\pi^2}{3\varepsilon_0 h^2}\mu_{10}^2 \tag{1.14}$$

where, ε_0 is the permittivity of free space (C^{-1} N^{-1} m^{-2}) and h is Planck's constant. Spontaneous emission lifetime and energy losses due to collisions cause the molecular absorption line shape to change from the Dirac delta function (infinitely sharp and narrow and with area equal unity) into a real line shape [24, p. 19-21]. For this reason, the expression in equation (1.14) is modified by including the line shape function $g(v - v_{10})$, where v_{10} is the transition frequency. Using the modified version of equation (1.14), we can rewrite equation (1.13) into

$$\frac{dN_1}{dt} = \frac{2\pi^2\mu_{10}^2 v}{3\varepsilon_0 hc}(N_0 - N_1)g(v - v_{10})F = \sigma F(N_0 - N_1) \tag{1.15}$$

where, $\rho = {}^{I}\!/_{c} = hvF/c$ is used, c is the speed of light in vacuum and σ is the absorption cross section given by the equation:

$$\sigma = \frac{2\pi^2\mu_{10}^2}{3\varepsilon_0 hc}vg(v - v_{10}) \tag{1.16}$$

17

with units of m², which indicates its physical interpretation as the "effective area" that the target molecule represents for the incident photons. With equation (1.15) in mind, the change in flux when it passes through a length element dx can be expressed as:

$$dF = -\sigma F(N_0 - N_1)dx \tag{1.17}$$

Upon integration over the absorption path l, this becomes

$$\ln\left(\frac{F}{F_0}\right) = ln\left(\frac{I}{I_0}\right) = -\sigma(N_0 - N_1)l \tag{1.18}$$

which can be rewritten to the more common form

$$I = I_0 e^{-\sigma(N_0 - N_1)l} = I_0 e^{-\alpha(\bar{v})l} \tag{1.19}$$

where $\alpha(\bar{v}) = \sigma(N_0 - N_1)$ is the absorption coefficient for the system. This formula is equivalent to the common decadic formula of Beer's law [24, p. 19-21]

$$I = I_0 10^{-\varepsilon Cl} \tag{1.20}$$

where ε is the molar absorption coefficient (L mol^{-1} cm^{-1}), C is the concentration in mol/L and l is in cm rather than SI units. There are many assumptions that have been made either implicitly or explicitly in the derivation of Beer's law that define the limitations of this law and they can be listed briefly [35]:

1. Incident radiation is monochromatic.

2. Absorbing molecules do not interact with each other.

3. The incident radiation is collimated and perpendicular to the sample surface.

4. The absorbing medium is homogenous and does not scatter light.

5. Incident photon flux is not high enough to cause saturation.

6. Transmittance scale should be linear.

1.5: Line Shape Functions

As discussed earlier, line shape is important in the quantitative analysis of spectra for concentration and physical properties of the target molecules. The deviations from the ideal Dirac delta function that represents an ideal line arise from the uncertainties in the upper energy level of the transition, due to spontaneous emission. This effect is called "natural lifetime broadening", which is a homogenous broadening effect since it has equal effect on all the molecules. This homogenous broadening is represented by the normalized Lorentz line shape profile given by:

$$g_L(v - v_0) = \frac{\gamma}{(\frac{\gamma}{2})^2 + (2\pi)^2(v - v_0)^2} \tag{1.21}$$

The full width at half maximum (FWHM) Δv_L is related to the spontaneous emission lifetime constant τ_{sp} $\left(\gamma = \frac{1}{\tau_{sp}}\right)$ through

$$\Delta v_L = \frac{\gamma}{2\pi} = \frac{1}{2\pi\tau_{sp}} \tag{1.22}$$

which agrees with the Heisenberg time-energy uncertainty principle $\Delta E \times \Delta t \geq \hbar$ that as an equation can be rewritten into

$$\frac{\Delta E}{h} \tau_{sp} \sim \frac{1}{2\pi} \tag{1.22a}$$

This natural line width calculated from the uncertainty principle sets the accuracy limit for measuring the line position.

Every gas molecule at a temperature above absolute zero possesses kinetic energy, since the average kinetic energy of an ideal gas molecule is related to its temperature by

$$\overline{E_k} = \overline{\frac{1}{2}mv^2} = \frac{3}{2}kT \qquad (1.23)$$

where m is molecular mass, v is average molecule speed, k is Boltzmann's constant and T is gas absolute temperature. The gas molecules are not all moving at the same speed or direction but rather move in random fashion described by the Maxwell-Boltzmann distribution function:

$$P_v dv = \left(\frac{m}{2\pi kT}\right)^{1/2} e^{-mv^2/(2kT)} dv \qquad (1.24)$$

Since not all molecules have the same Doppler shift due to the varying velocities, Doppler broadening is inhomogeneous broadening, where FWHM, Δv_D is given by:

$$\Delta v_D = 2v_0 \sqrt{\frac{2kT \ln(2)}{mc^2}} = 7.2 \times 10^{-7} \tilde{v}_0 \sqrt{\frac{T}{M}} \qquad (1.25)$$

where M is the molecular mass in atomic mass units, $\tilde{v}_0$ is transition frequency in cm^{-1} and Δv_D is Doppler FWHM in cm^{-1}. In the case of Doppler broadening, the line profile is described by the Gauss function (see reference [24, p. 28-30] for full derivation) :

$$g_G(v - v_0) = \frac{2}{\Delta v_D} \sqrt{\frac{\ln(2)}{\pi}} e^{-4\ln2\left[\frac{(v-v_0)}{\Delta v_D}\right]^2} \qquad (1.26)$$

Doppler inhomogeneous broadening dominates the line shape at low pressures. However, by increasing the pressure the collisions between the gas molecules increases producing what is known as pressure broadening. Pressure

broadening is homogenous since the collision effects are the same for all molecules; therefore, it can be represented by the Lorentz line shape function with width given by

$$\Delta \nu_P = \frac{1}{\pi T_2} \tag{1.27}$$

where T_2 is the average time between collisions and it is inversely proportional to the pressure, p and the FWHM is related to pressure by

$$\Delta \nu_P = bp \tag{1.28}$$

where b is the pressure broadening coefficient and its quantitative calculation is a difficult theoretical problem [25, p. 28]. Figure (1.7) shows both the Gauss and Lorentzian line shape examples.
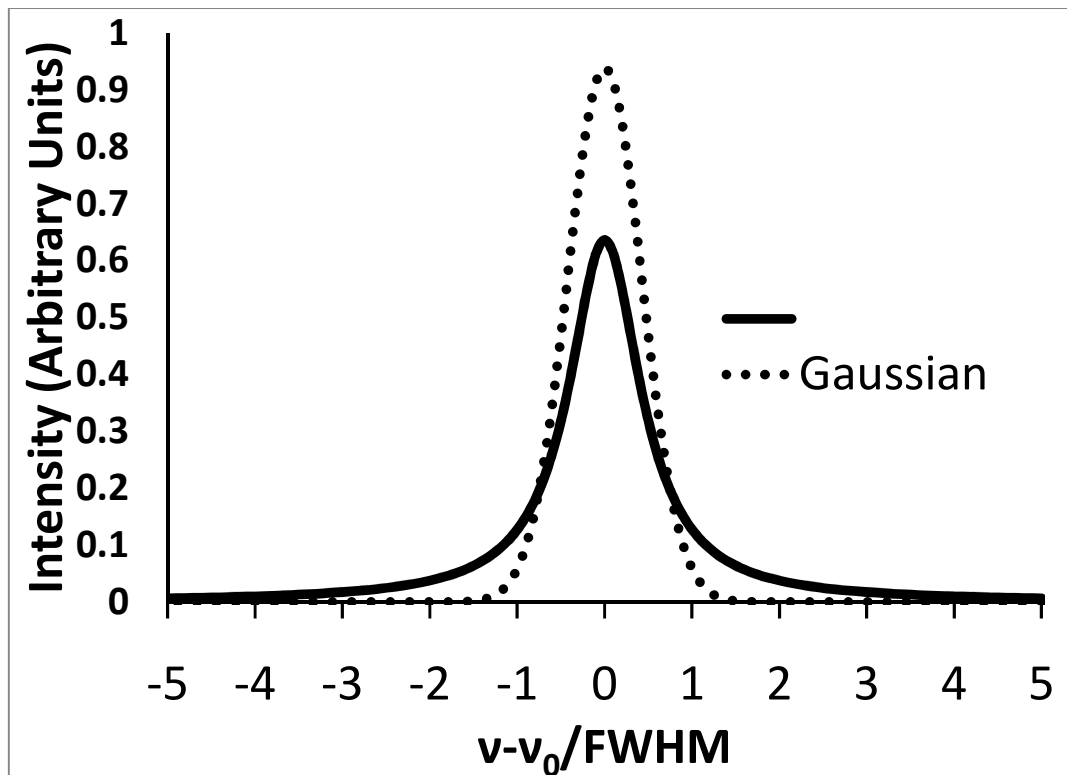
Figure (1.7): Gaussian and Lorentzian line shapes

If both Doppler and pressure broadening FWHMs have the same order of magnitude, a Voigt line profile should be used [25]. The Voigt line profile is a convolution of both the homogenous Lorentz line profile and the inhomogeneous Gauss line profile as expressed by

$$g_V(\nu - \nu_0) = g_L(\nu - \nu_0) \otimes g_G(\nu - \nu_0) \tag{1.29}$$

Therefore, Voigt is a general profile that can be either purely homogenous or purely inhomogeneous as limiting cases. The Voigt profile is difficult to express analytically; however, Liu et al. [36] introduced the following empirical expression to approximate the Voigt function:

$$
\begin{aligned}
g_V(\nu - \nu_0) = C_L \; &\frac{1}{\pi} \frac{\Delta\nu_L}{\Delta\nu_L{}^2 + (\nu - \nu_0)^2} \\
+ C_G \; &\frac{2}{\Delta\nu_D} \sqrt{\frac{\ln(2)}{\pi}} \; e^{-4\ln2\left[\frac{(\nu - \nu_0)}{\Delta\nu_D}\right]^2}
\end{aligned}
\tag{1.30}
$$

where C_L and C_G are weight coefficients for Lorentz and Gauss profiles, respectively.

The Voigt profile assumes that both pressure and the Doppler broadening mechanism are not correlated; however, various molecular spectra deviating from this assumption have been reported in recent studies [25]. In general this deviation results in an unexpected narrower line shape, which could also be asymmetric compared to the Voigt line profile [37]. One explanation for this is provided by Dicke [38], who attributed this deviation to the speed/velocity changing collisions. Dicke's analysis assumed that the collisions do not disturb the molecule's quantum states and that the molecule's mean free path is smaller than the interacting wavelength. These conditions imply that Dicke narrowing has a noticeable effect in the far-

infrared and microwave regions or at relatively low pressures in the infrared region, which is known as the Doppler regime. The Dicke narrowing effect changes the line profile from Gaussian to Lorentzian as given by[38]:

$$g(\nu - \nu_0) = \frac{\frac{2\pi\beta c^2}{\nu^2}}{(\nu - \nu_0)^2 + (\frac{2\pi\beta c^2}{\nu^2})^2} \tag{1.31}$$

where λ is the wavelength of the interacting wave and β is the self-diffusion constant of the gas. The FWHM is equal to $4\pi\beta/\lambda^2$, which is roughly $2.8L/\lambda$ times the Doppler FWHM (L is the mean free path). For this reason, when L is much smaller than the wavelength, the line FWHM is reduced (Dicke narrowing). If the collisions are soft (i.e. the mass of the absorbing molecules is larger than the colliding molecules), the Galatry line profile [39] can be used. In case the collisions are of the hard type (colliding molecules are larger than emitting ones), the Rautian line profile [40]. Examples of molecules whose spectra deviate from Voigt profile are listed in reference [41].

The second explanation for the deviation from the Voigt profile is the dependence of the relaxation rates on the molecular speeds. Berman [42] considered the effect of molecular speed on relaxation and introduced an extension to the Voigt profile known as speed-dependent Voigt profile (SPD). In this profile, the emission line shape for transitions between two optically isolated, non-degenerate radiative levels, assuming the Maxwellian speed distribution[13], can be given by [42]:

---

[13] The speed distribution is for the molecules in their initial state

$$g(\nu - \nu_0) = \frac{(\frac{\Delta\nu_L}{2})}{\pi^{3/2} V_p} \int_{-\infty}^{\infty} \frac{e^{-V^2/V_p^2} dV}{(\frac{\Delta\nu_L}{2})^2 + (\nu - \nu_0 - \tilde{\nu}V)} \qquad (1.32)$$

where $\Delta\nu_L$ is the Lorentzian FWHM

V_p is the most probable velocity for the molecule

ν_0 is the transition frequency and

$\tilde{\nu}$ is the wavenumber $= \nu/c$, c is speed of light in vacuum

If the collision broadening in one of the radiative levels is somewhat larger than that of the other, the modification of the line shape due to the collisions will be accounted for by the replacements [42]

$$\Delta\nu_L \rightarrow \Delta\nu_L + \Gamma_{ab}(V) \text{ and } \nu - \nu_0 \rightarrow \nu - \nu_0 - \delta_{ab}(V) \qquad (1.33)$$

Where $\Gamma_{ab}(V)$ and $\delta_{ab}(V)$ are the speed-dependent broadening and shift, respectively. Using these substitutions and performing the integration will produce the speed-dependent Voigt profile (SPD) (for more details see reference [42]).

1.6: Line mixing

Line mixing has been observed in laboratory spectra for some bands of greenhouse molecules such as CO_2, CH_4 and H_2O. Line mixing happens when transition energies are close and, with broadening effects, the line profiles of these transitions overlaps. The accuracy of retrieved vertical temperature and pressure profiles is degraded when carbon dioxide Q-branches are used without accounting for line mixing effects [43]. Also, Hartman et al. [44] showed that accounting for line mixing is required to achieve accuracy better than 1% in atmospheric CO_2, which is lower than the targeted 0.3% accuracy of the OCO mission. Since the atmospheric

sounders are now operating at significantly higher spectral resolution (such as ACE-FTS[14] [45]), their sensitivity to line mixing has increased [46].

At sufficient separation between spectral lines, the approximation of Rosenkranz [47] can be used. In this approximation, line mixing is included through addition of all contributing lines multiplied by mixing coefficients $Y_l^{gas-X}(T)$ where "gas" is the absorber and X is the perturber molecule causing the broadening [48]. At higher pressures, with significant line mixing effects, it is usually necessarily to use the relaxation matrix in calculating the spectrum [48]. The details of these calculations are shown elsewhere [49]. The diagonal elements of the relaxation matrix are related to the Lorentz line widths b_{Lj} and the pressure-induced shifts δ_j of individual transition by equation [48]:

$$W_{JJ} = b_{Lj} + i\,\delta_j \qquad (1.34)$$

If all off-diagonal elements are set to zero, the line profiles will be reduced to a summation of a number of Lorentz lines that are mixing.

1.7: Concluding Remarks

In this chapter, a brief discussion of the role of optical remote sensing techniques in monitoring greenhouse gases and related spectroscopic theory was presented. The relation between quantitative analysis using Beer's law to retrieve atmospheric concentration and spectral line shape was discussed and explained. The complexities resulting from the different line shape models and line mixing effects show the need for higher spectral resolution measurements. This higher

---

[14] ACE-FTS is Atmospheric Chemistry Experiment - Fourier Transform Spectrometer on SCISAT-1

resolution requirement and the continuous development of satellite missions to achieve higher accuracies in atmospheric gas retrieval require more research on increasing the efficiency of spectroscopic laboratory measurements. Because FTIR spectrometers can achieve the resolution and accuracy requirements and they are common in both field and laboratory, improving FTIR accuracy is important for remote sensing applications. For these reasons, employing synchrotrons as source for FTIR spectrometers to achieve better performance and the challenges of synchrotron as a source will be discussed in the next chapter.

"The deep study of nature is the most fruitful source of mathematical discoveries. By offering to research a definite end, this study has the advantage of excluding vague questions and useless calculations; besides it is a sure means of forming analysis itself and of discovering the elements which it most concerns us to know, and which natural science ought always to conserve."[50]

Joseph Fourier / French Mathematician and Physicist in his honor Fourier transform named.

Chapter 2: Fourier Transform Infrared (FTIR) Spectroscopy using Synchrotron Sources

2.1: Introduction to FTIR

The Michelson interferometer was the first interferometer to be used in FTIR spectroscopy [see figure (2.1)] and is still the corner stone of all current commercial interferometers [51]. However, FTIR spectroscopy has had many significant developments in its technologies and applications since the employment of computers in the 1950s to calculate the Fourier transform of the recorded interferogram [52].
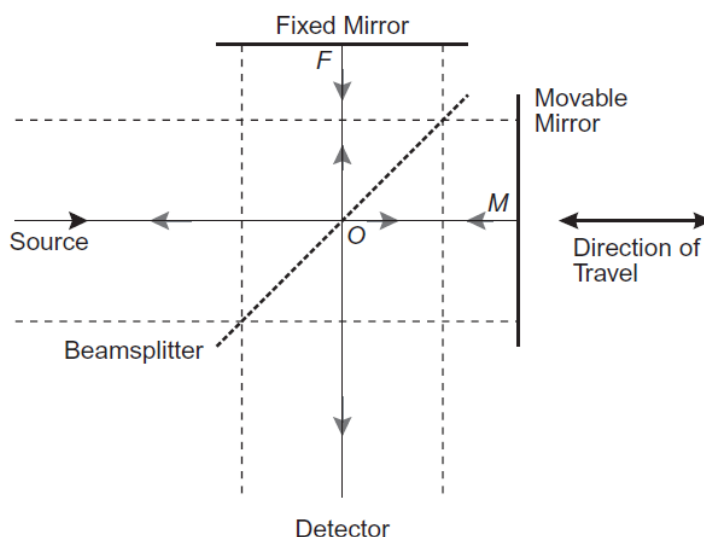
Figure (2.1): Optical layout of Michelson interferometer [53].

In comparison to other dispersive spectroscopic techniques, there are many advantages to FTIR spectroscopy:

1. Its ability to encompass the full wavelength range during a single scan, known as the Fellgett or multiplexing advantage [54].

2. Its ability to utilize the complete intensity of different wavelength components, leading to higher optical throughput, known as the Jacquinot or throughput advantage [55].

3. Its utilization of a monochromatic light source (e.g. He-Ne laser) in the control of the optical path difference acts as an integrated high-precision wavelength calibration, known as the Connes advantage [56].

4. Its ability to allow all incident flux wavelength contributions to the interferogram, while preventing stray light contributions (except in cases of high temperature samples [57]), known as the stray light advantage [58].

2.2: Channel Spectra in FTIR Spectroscopy

In spite of all its advantages, there is one major drawback that can make the signal to noise ratio (SNR) of the recorded spectra decline, namely the phenomenon of channel spectra, sometimes called "fringing". Channel spectra are the result of extra interferences between light beams inside the FTIR spectrometer in addition to the main interference that occurs at the zero path difference (ZPD) position. These additional interferences create extra interference patterns called "spikes" or

"signatures". These problem spikes are generally located near the central interference pattern that occurs when the FTIR spectrometer mirror is at the ZPD position as shown in figure (2.2). As any localized feature in the interferogram space will result in sinusoidal waves in the spectrum space [see figure (2.3)] upon Fourier transformation, these spikes transform into periodic intensity changes in the baseline of the generated spectrum. The presence of channel spectra in our spectrum creates difficulties in analysing and modeling the recorded spectra in order to extract the required spectral parameters accurately. These spikes in the interferograms producing channel spectra can be attributed to two possible sources.

The first source for channel spectra, which is unique to FTIR spectrometers using synchrotron sources, arises from the need to inject electron current into these sources on a regular basis to balance the energy dissipated by the synchrotron radiation. During these current injections, the orbit of the electron beam moves considerably, changing the synchrotron radiation direction. This movement changes the radiation path length and direction in the spectrometer, causing a transient spike in the detector response that is recorded in the interferogram data [59]. The second source can be traced back to extra interferences between beams reflected by any of the spectrometer optical components (windows, beam splitters, etc.) or the optical components of the transfer optics when using external sources (as in the case of synchrotron sources). These extra interferences produce additional interference patterns that have a different ZPD than the spectrometer ZPD; therefore these extra interference patterns (spikes) are located in the vicinity of the main ZPD interference pattern of the spectrometer.
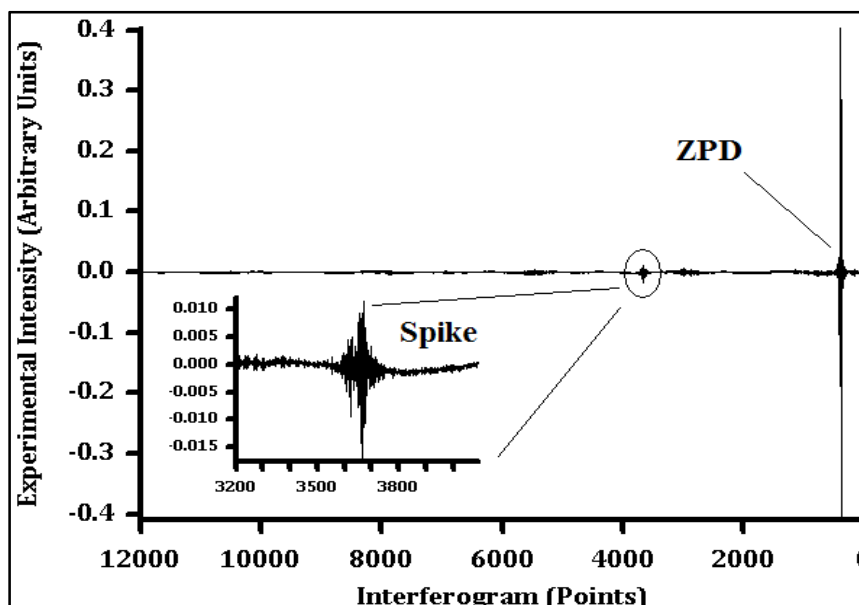
Figure (2.2): FTIR Interferogram[15] and spikes.
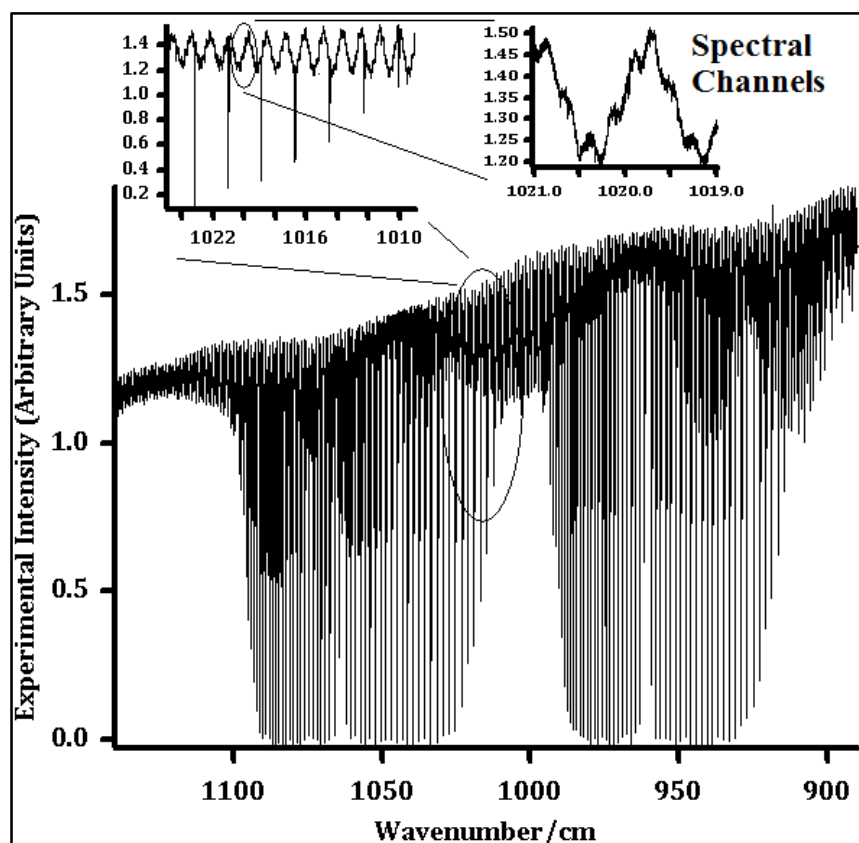
Figure (2.3): FTIR spectrum and the channel spectra.

---

[15] Both interferogram and spectrum belong to the same CO_2 sample recorded at CLS

Figure (2.4) shows the geometry of these interferences, with intensity given by the well-known Airy formula [60, 61]. This formula is extended by Gronholz and Herres [61] to include absorption loss and format it better for Fourier transform

$$S(v) = S_0 + 2S_0 \sum_{k=1}^{\infty} \{R(v)\exp(-ad)\}^k$$

$$\times \cos(4\pi kn(v)d - 2k\varphi(v)) \tag{2.1}$$

with $S_0(v) = B(v)\frac{(1-R(v))^2\exp(-ad)}{1-R^2(v)\exp(-2ad)}$

where $S(v)$ is single channel spectrum, S_0 is channel free spectrum, $R(v)$ is reflectance, $a(v)$ is absorption coefficient, d is the thickness of the plate, $n(v)$ is refractive index, $\varphi(v)$ is the phase change occurring at every internal reflection and $B(v)$ is the empty cell (background) spectrum. Equation (2.1) shows that the FTIR spectrum can be represented as the sum of the fringe-free spectrum and an infinite number of interference terms. Inverse Fourier transformation of equation (2.1) will result in an interferogram that contains spikes at distances $2nkd + 2k\varphi$ on both sides of the central burst [61].
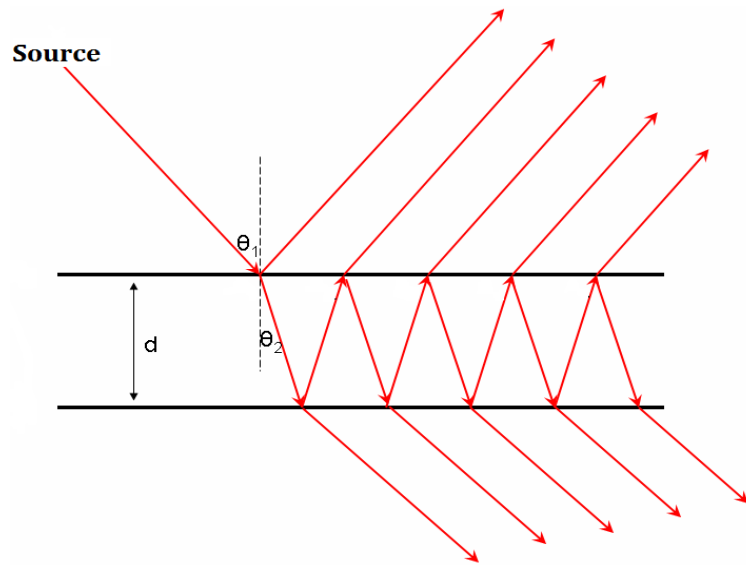
Figure (2.4): Multiple beam interference in parallel plate.

31

2.3: Synchrotron Sources for FTIR Spectrometers

As discussed in chapter one, improvement in the quality of spectroscopic laboratory measurements is essential for acquiring accurate spectroscopic parameters, which in turn improve the efforts for remote sensing of greenhouse gases. The quality of any recorded spectrum is often quantified using the signal to noise ratio (SNR). The intensity signal for any spectroscopic technique is determined by Beer's law. Beer's law relates the absorption of light to the concentration of the absorbing material, which is rewritten here for convenience [62]:[16]

$$I = I_0 e^{-\alpha(\bar{v})lC} \ and \ A = -\ln T = -ln(I/I_0) = \alpha(\bar{v})lC \qquad (2.2)$$

where I is radiation intensity after passing through length l of the sample under study, I_0 is the radiation intensity before passing through the sample (usually the source intensity), $\alpha(\bar{v})$ is the absorption coefficient as a function of wavenumber $\bar{v}$, l is the distance the light travels through the sample, C is the sample concentration and T and A are transmittance and absorbance, respectively. Beer's law formulated in equation (2.1) gives rise to two main approaches in enhancing the SNR of the recorded spectra by increasing the recorded signal. The first approach is to increase the distance that the radiation travels through the medium (optical path length) ℓ. The second approach is to increase the intensity of the radiation source I_0. In practice, one or a combination of both approaches is usually employed. Long optical path lengths are achieved by utilizing multi-pass cells with White [63], Herriott [64]

---

[16] Equation (2.1) is general case of equation (1.19) which are for pure sample (C=1).

or Astigmatic Herriott [65] designs [see figure (2.5)]. These designs are commonly used in spectroscopic experiments, while taking into consideration the appropriate optical alignment satisfying the required long path length [66]. These cells designs prove useful in measuring atmospheric trace gases that have very low concentrations [67]. The drawbacks of the multi-pass designs are the accumulated loss of the signal power due to reflections losses and the existence of interference patterns. However, improvements of the mirror reflectivity used and the ability to realign the cell to avoid the interference patterns [68] continue to improve its performance and make it a popular choice[69].
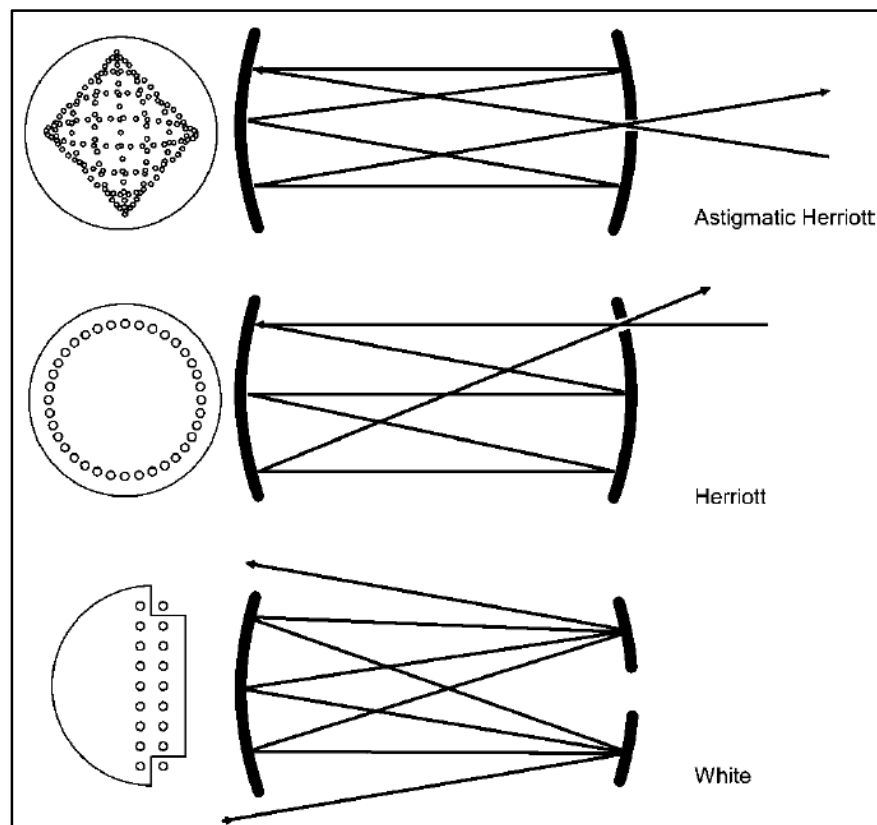
Figure (2.5): White, Herriott and Astigmatic Herriot cell optical layouts with their spot patterns [69].

In contrast to increasing the optical path length, increasing the intensity of infrared sources, especially in the far-infrared spectral region, is not an easy task. Conventional thermal infrared sources like globar or mercury lamps possess a weak spectral density in the far-infrared region [70] . A relatively limited increase in the spectral density of the emitted radiation for these thermal sources can be achieved by increasing the source temperature and/or its emissivity. To illustrate the impact of the source brightness on the SNR, we can refer to equation (2.3) [71, 72] developed for FTIR instruments, which quantitatively relates the SNR of individual scans to the experimental conditions:

$$S/N = \frac{B(\bar{v})\,\delta(\bar{v})\,\Theta\,\zeta\,D^*}{(\Delta f)^{1/2}\,A^{1/2}} \qquad (2.3)$$

where $\bar{v}$ is the wavenumber, $B(\bar{v})$ is the brightness, $\delta(\bar{v})$ is the resolution, Θ is the limiting étendue (sometimes called optical throughput) of the experiment, ζ is the optical efficiency, D^* is the detectivity, Δf is the electronic bandwidth, and A is the area of the detector.

Equation (2.3) shows that the SNR can be boosted by increasing the source brightness (sometimes called brilliance or radiance), which is defined as the power / (area × solid angle). Unfortunately, it is not possible to limit the natural emission solid angle for conventional thermal sources in order to increase its brightness. On the other hand, synchrotron sources have a much smaller source size [71], which leads to smaller emission solid angle than conventional sources. This narrow emission solid angle is the reason synchrotron sources produce a much brighter

beam (not necessarily with higher intensity) than conventional sources. Another advantage of synchrotron sources is the fact that they are absolute sources, in the sense that they do not require any external calibration with respect to a radiometric standard [73]. This calibration-free property results from the dependence of the synchrotron brightness on the storage ring beam current, which can be measured accurately. For example, in the infrared spectral range, where the synchrotron light is diffraction limited, the brightness can be related to the storage ring current by the approximate relation (2.) [71]:

$$B_{SR} \approx 10^{-8} I \, \bar{v}^{-2} \, W \, mm^{-2} \, sr^{-1} \, cm \qquad (2.4)$$

where I is the beam current of the storage ring in Amperes and $\bar{v}$ is wavenumbers (cm^{-1}). To summarize, synchrotron sources offer many advantages over conventional sources as infrared sources such as [70-75]:

1. Brightness orders of magnitude higher than conventional sources.

2. Absolute sources not requiring radiometric calibration.

3. Broadband sources that produce wide spectral range.

4. Highly polarized radiation in the plane of the storage ring and well-defined incidence angle, making them very suitable sources for polarizing FTIR spectrometers.

In spite of all their advantages, synchrotron sources for FTIR spectrometers introduce practical difficulties that do not exist in conventional sources. One of these difficulties arises from the fact that, due to relativistic corrections, the radiation angle of the bending magnet is less than 2π and is wavelength dependent. This

dependence of the radiation angle on wavelength introduces the synchrotron's distinguishing angle, called the "natural opening angle". The natural opening angle is defined as the angle required for transmitting 90% of the emitted beam energy. This natural angle depends on both the radius of the synchrotron bending magnet and the emitted radiation wavelength as shown in equation (2.5) [75, 76]:

$$\theta_{natural}[radiance] \approx 1.66 \left(\frac{\lambda}{\rho}\right)^{1/3} \qquad (2.5)$$

where λ is the wavelength and ρ is the radius of curvature for the synchrotron bending magnet (in the same units as λ). Equation (2.5) shows that large natural opening angles are required to extract radiation at far-infrared wavelengths. For example, a third-generation[17] synchrotron facility such as the Canadian Light Source (CLS), with a bending magnet of 7.1428 m radius, produces radiation that is emitted at 85 millirad full angle for 10 cm^{-1} wavelength [77].

The extraction of radiation at such small angles presents practical difficulties, since it requires wide-angle infrared ports with relatively large area. These port windows need to handle pressure differences between the ultra-high vacuum (UHV) of the storage ring and the usually lower vacuum levels in the transfer optics delivering the light to the spectrometer. These wide-angle ports (usually diamond windows) are difficult to manufacture with a uniform refractive index. This possible lack of refractive index uniformity combined with the possible shifting of the synchrotron beam can lead to a higher probability of generating the troubling channel spectra.

---

[17] Third generation synchrotrons are ones dedicated for researches using beam light and its designs are optimized to produce high brightness beam suitable for research applications.

Another synchrotron source challenge arises from the fact that the synchrotron produces higher energy photon beams (for example X-rays), which have to be removed; otherwise the first optical element will not handle its high power. Removing these photons can be accomplished in two ways, either by using a slot to pass the high energy photons through, or by using a mask to absorb it. Figure (2.6) shows an example of a mask and mirror arrangement used at CLS far-infrared beamline to remove the unwanted radiation. In both situations some effective cooling has to be applied in order to avoid vibrations of the surface mounts that would increase the noise and enhance channel spectra.
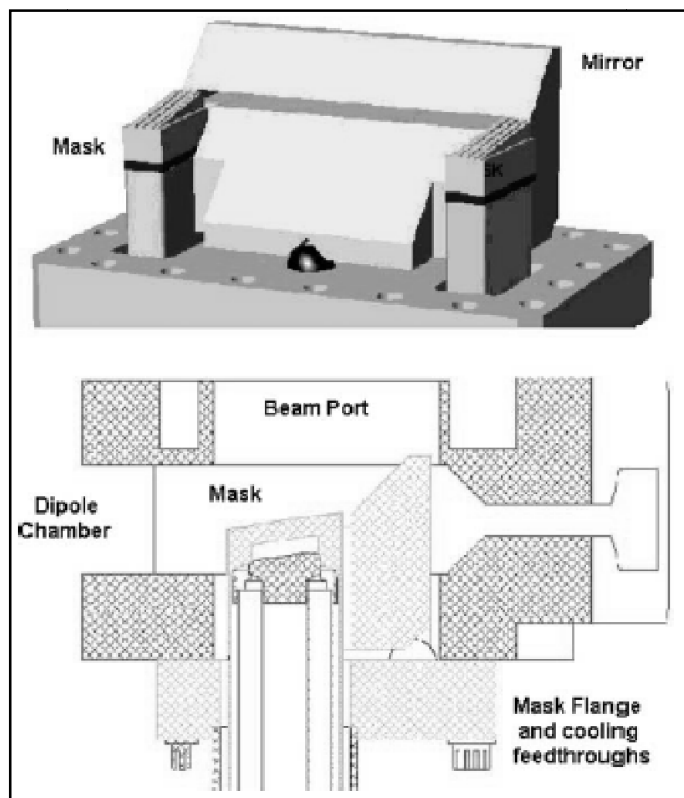
Figure (2.6): Mask and mirror arrangement[18] for far-infrared beamline port at CLS [78].

---

[18] The surface is ribbed and 8° incidence angle to spread heat [78].

Finally, the need for multiple steering mirrors to align and guide the beam into the spectrometer increases the number of possible sources for channel spectra, and complicates the process of tracing and analysing the sources of channel spectra. Figure (2.7) shows the transfer optics at the CLS far-infrared beamline and table (2.1) lists the mirrors used in it.
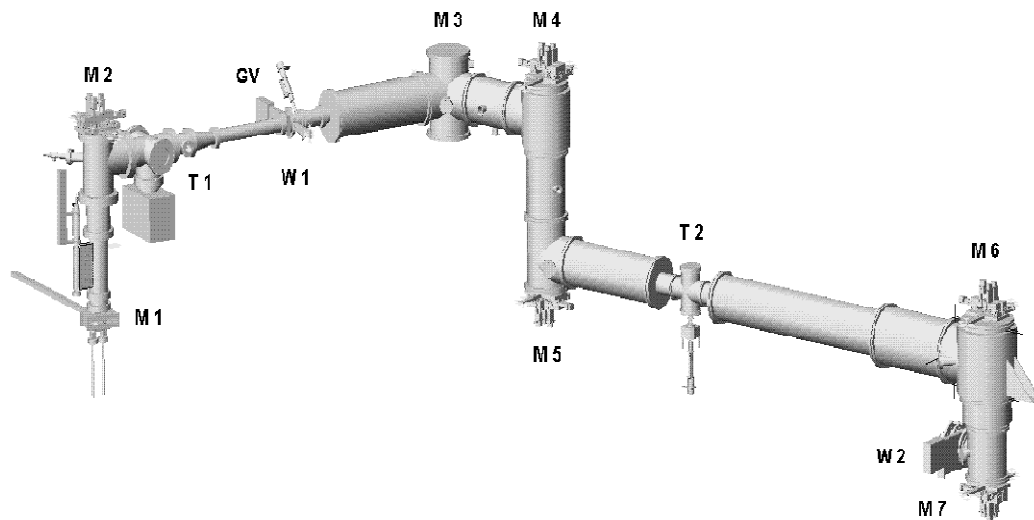
Figure (2.7): The Far IR beampipe at CLS from the source at lower left to spectrometer port W2 at right. Diamond window W1 separates UHV and rough vacuum; alignment targets T1, T2; gate valves GV[79].

Table (2.1): Far-IR beamline transfer optic elements at CLS (dimensions in mm).

Mirror Optic	Type	Radii Major/Minor (window thickness)
M1	Plane	-
M2	Ellipsoidal	2555/1790
Window1	Wedged 1.5°	(0.50)
M3	Plane	-
M4	Ellipsoidal	2464
M5	Plane	-
M6	Ellipsoidal	2298/1532
M7	Plane	-
Window2	Wedged	(6.0)
M8 in FTIR	Plane	-

To demonstrate the effect of channel spectra resulting from transfer optics at synchrotron facilities and to illustrate how much the quality of recorded FTIR spectra declines due to these channels, two spectra of the same sample of CO_2 mixed with air were recorded with both synchrotron and globar sources using the same spectrometer and experimental settings. Figure (2.8) shows clearly the existence of channel spectra in the spectrum recorded with the synchrotron source compared to the one recorded with the globar source.

2.4: Improvements of Synchrotron Sources

Despite difficulties in the use of synchrotron radiation in the far-infrared, further improvements of the SNR ratio for synchrotron sources are explored through different techniques. Examples of these techniques include using edge radiation by extracting the radiation from the extremities of the bending magnets. Edge radiation produces a beam with similar intensity to the bending magnet radiation but with a smaller angular size than the natural opening angle, therefore increasing the beam's brightness [76]. Another technique to increase the SNR is the use of the coherent summation of synchrotron radiation (CSR) operation mode [77]. In the CSR operation mode, the length of synchrotron electron bunches is reduced by varying the parameters of the accelerator so that the bunch length is of the same order as the far-infrared wavelength range leading to the coherent addition of photon bunches. Recent results showed that the CSR mode can increase the beam intensity by four orders of magnitude at the CLS far-infrared beam line [77]. However the effect of increased coherency on increasing the channel spectra has not been studied.

Another approach to enhance synchrotron performance is the use of the top-off operation mode. This mode of operation attempts to compensate the reduction of synchrotron radiation with time due to the decay of the storage ring current. Usually, synchrotron facilities operate in decay mode in which the initial storage ring current decays to near half of it value before a new current injection is made [59]. This usually requires current injection two or three times a day. During this long period between injections (8 or 12 hours), the decaying current and radiation intensity can produce thermal instabilities in the beamline optics. Therefore, top-off mode, in which the electron beam is quasi-continuously injected into the storage ring in order to conserve the ring current value, can reduce these instabilities. However, this mode of operation, as mentioned in section (2.2), could give rise to spikes in the interferogram. Recently, Vernoud et al. [59] proposed using either a feedback mirror to lock the infrared beam into the sample at slow injection rates or a gating system at high injection rates to interrupt interferogram collection during injections. The gating method cannot work effectively at high spectral resolution because the prolonged time required to record the scans is longer than the time interval between current injections.
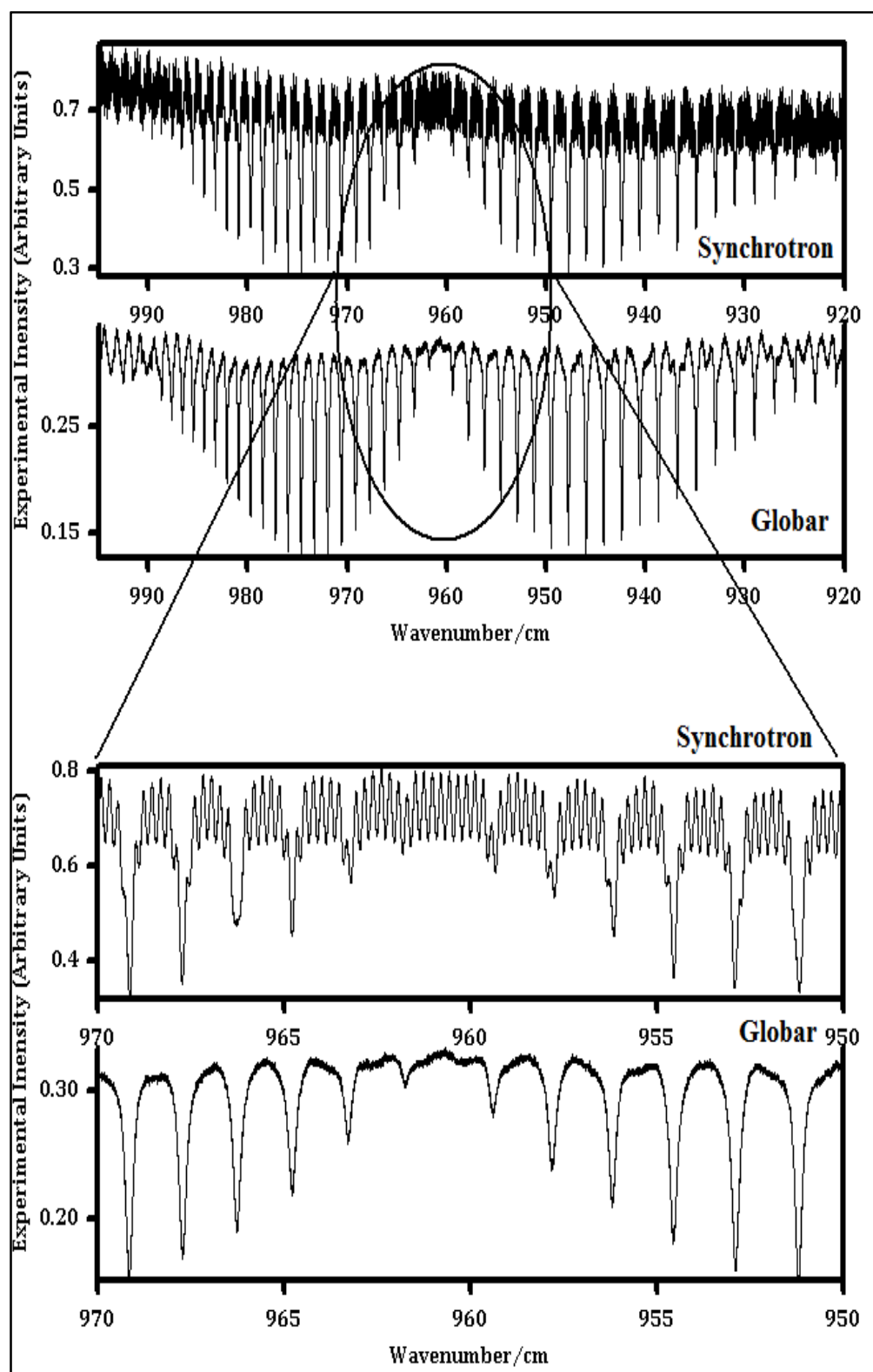
Figure (2.8): Two spectra of CO₂ sample recorded at CLS using synchrotron and globar sources.

2.5: Experimental conditions at the Far-IR beamline at the CLS

The experiments were carried out at the far-infrared beamline at the CLS facility, Saskatoon, Saskatchewan, Canada. CLS is Canada's national synchrotron facility, and it consists of a 250 MeV linac (linear particle accelerator), a 2.0 GeV booster ring, and a compact double-bend achromatic lattice storage ring (with a super-conducting RF cavity) that delivers excellent performance from 1.5 to 2.9 GeV, the latter being the operating energy [80, 81]. The far-infrared port has a wedged 1° window to reduce channel spectra (more details on the design can be found in reference [79]). Although the detailed structure of the port and associated beamline optics will not be discussed, there are two points that are of concern.

First, the port size is given to be 58 mrad by 58 mrad, which is equal to the natural angle at 173 μm (58 cm^{-1}). This relatively large size angle could raise concerns about the uniformity of the refractive index within this port window, as discussed earlier. Second, the high-energy photons (like X-rays) are removed by using a mask in front of the mirror to absorb them. The mirror has to be cooled to avoid vibrations of the mirror mount [78]. As mentioned earlier, this wide window and the masking arrangement could create reflections and vibrations that may introduce more channel spectra into our spectra. The light beam is delivered into the Bruker Optics IFS125HR spectrometer, which can achieve resolutions better than 0.00096 cm^{-1}. The gas sample is contained in a 2-meter multi-pass cell (White design) set at 72 meter optical path length. The cell is equipped with wedged KBr windows. The radiation is detected by cooled Ge:Cu detector with optical filter mounted to it. The cell temperature was monitored by using a T-type thermocouple

mounted inside the cell. The gas pressure was monitored using a 0-1000 torr Baratron MKS gauge. Figure (2.9) shows the experimental set-up at the far-infrared beam line end station at the CLS.
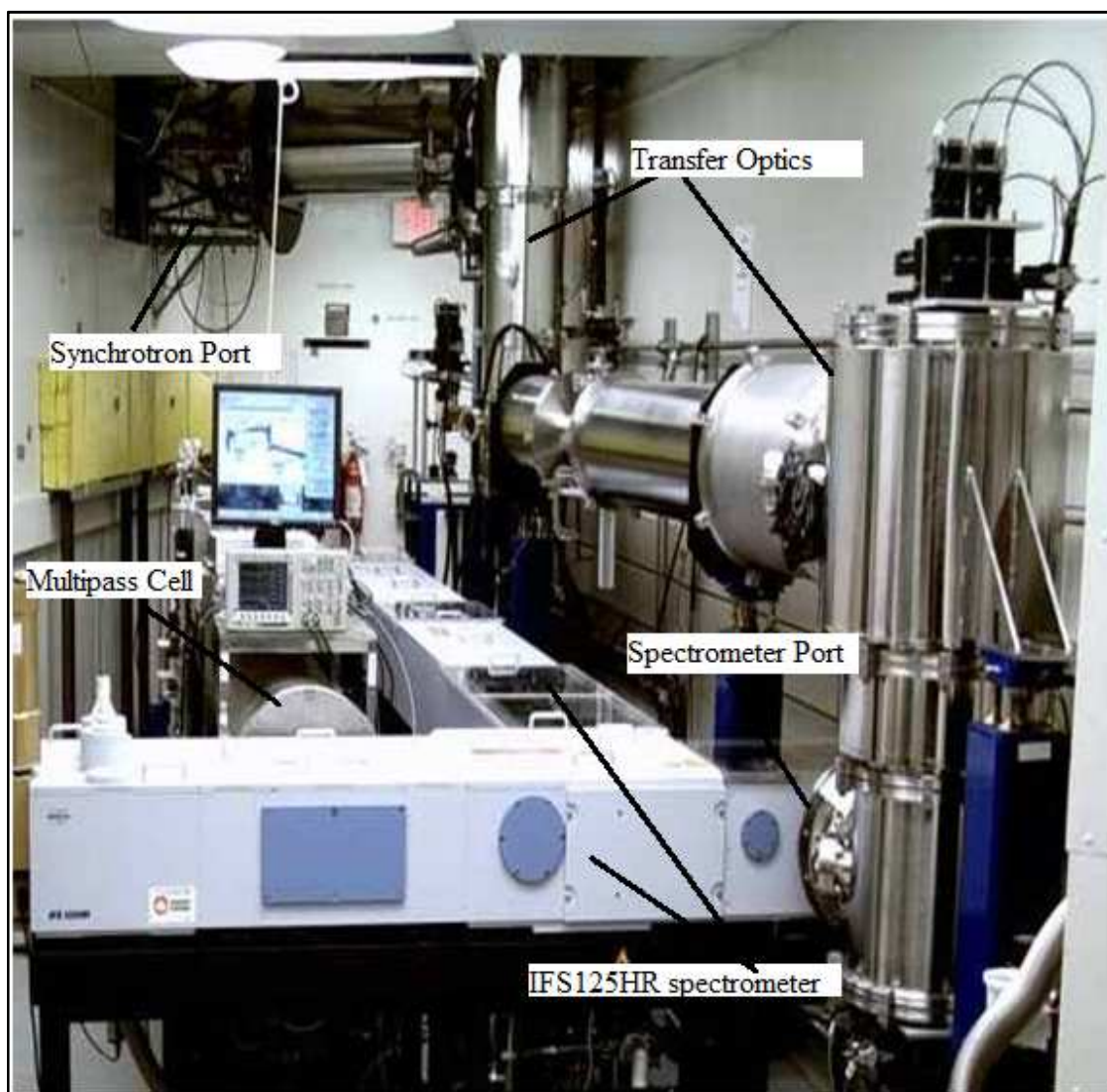
Figure (2.9): Far infra-red beamline end station at CLS showing the transfer optics, mutli-pass cell and the Bruker optics IFS125HR spectrometer.

2.6: Examples of Synchrotron-FTIR Measurements

Since the entrance pupil of the FTIR spectrometer operating at high spectral resolution must be small, the synchrotron source, with its small source size, will not lose a large percentage of its intensity compared to conventional sources. In May 2009, our research group was able to use this advantage to record high spectral resolution spectra of 1,1,1–trifluoroethane, CH_3CF_3 molecule. This molecule is of interest since it could be used to replace hydrochlorofluorocarbon (HCFC) in refrigerators by 2030[19] because it is thought it has no effect on the ozone layer. However, since CH_3CF_3 is a strong greenhouse gas, it was the subject of several spectroscopic measurements. Since CH_3CF_3 has a heavy molecular weight (84.041 g/mol), it has a very small rotational constant and closely separated rotational lines [see equation (1.8)]. Nivellini et al [82] analyzed the spectrum of the ν_4 band (C-C stretching) at 831 cm^{-1} with resolution 0.004 cm^{-1}. The K rotational structure was not resolved in their spectrum. Therefore, high resolution spectra of 0.00096 cm^{-1} were recorded at the CLS far-infrared beamline and the K-transition was observed due the combination of the high resolution and the brilliant synchrotron source [83, 84]. Figure (2.10) shows a comparison between the spectrum reported by Nivellini et al [82] recorded using conventional sources and the CH_3CF_3 spectrum recorded at the CLS and reported by Predoi-Cross et al. [83] who observed K-transition spectral lines. A full description of experimental conditions and results is given in reference [83]. Spectra were also recorded using the conventional globar source at the CLS for comparison and figure (2.11) shows the ability to resolve the Q-branch spectra

---

[19] Environmental Protection Agency (EPA) http://www.epa.gov/ozone/title6/phaseout/hcfc.html

using the synchrotron much better than using the Globar source at the same resolution [83]. Table (2.2) shows a summary of spectra recorded at the CLS and shows that the Globar source's lower SNR motivated us to collect more than double the number of spectra collected using the synchrotron source to improve SNR [see samples 2 and 3 in table (2.2)].

Table (2.2): Experimental setting for CH_3CF_3 spectra recorded at the CLS [83].

No.	Source*	Pressure (mTorr)	Temp. (K)	Path length (m)	Scanning velocity (KHz)	Resolution cm^{-1}	Detector gain	Number of scans averaged
1	SR	85	298.25	24.15	40	0.00096	64x	104
2	SR	200	298.25	72.15	60	0.00096	64x	142
3	GB	200	298.45	24.15	40	0.00096	64x	350
4	SR	301	216.75	24.15	40	0.00096	16x	374

*SR stands for synchrotron source and GB stands for globar source
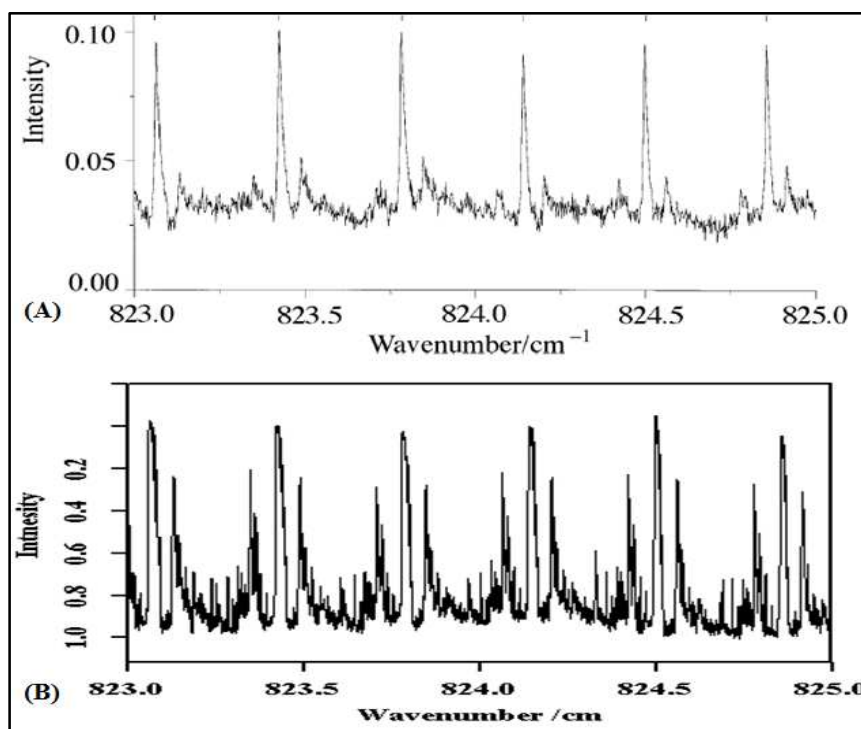
Figure (2.10): Comparison between CH_3CF_3 spectra recorded by Nivellini et al. [82](A) and Predoi-Cross et al.[83](B).
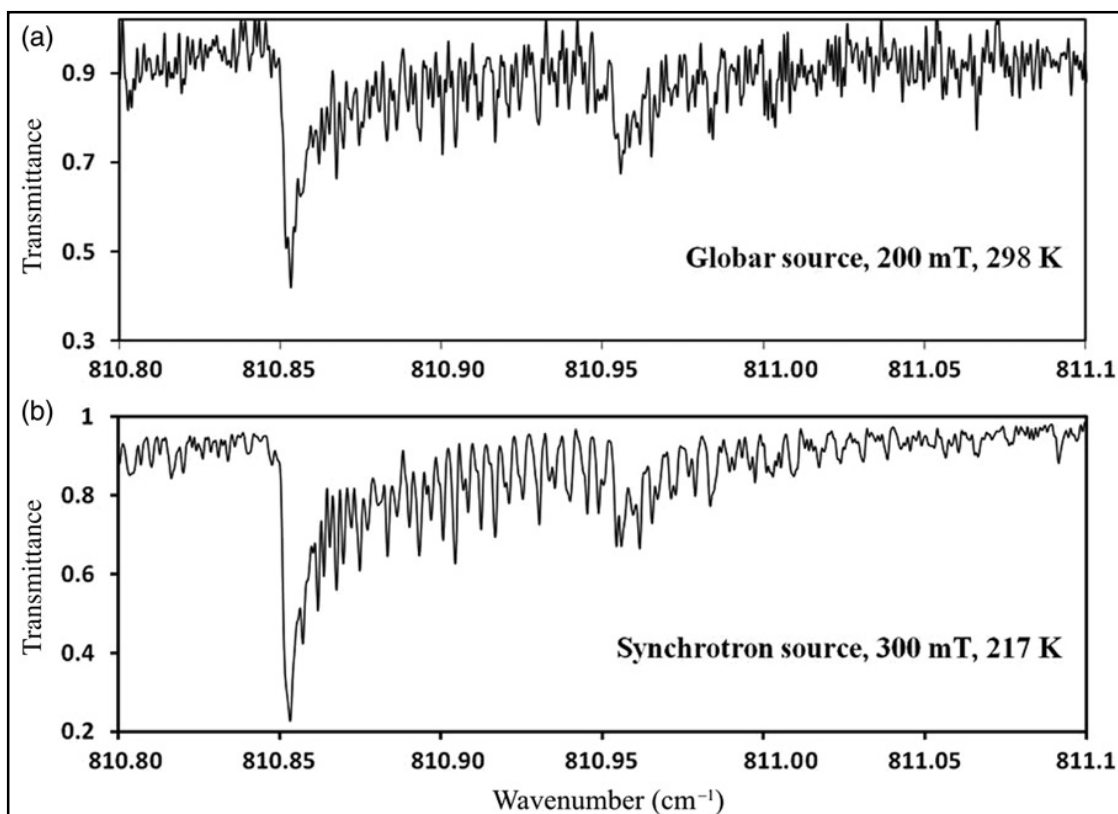
Figure (2.11): Segment of CH₃CF₃ recorded at CLS using (a) globar source and (b) synchrotron source [83].

2.7: Concluding Remarks

Synchrotron radiation employed as a FTIR source produced an increase in SNR in recorded spectra by two (or even more) orders of magnitude compared to conventional sources [85]. The advantage of the synchrotron results from the FTIR spectrometer requirement to reduce the aperture radius when recording high resolution spectra. The small source size of the synchrotron source minimizes the light intensity loss by these small apertures [51, p. 37]. These high resolution spectra with high SNR enable the more accurate study of spectral line shape and line mixing [86, 87] and exploring very weak absorption features which are otherwise at noise level [83]. The main obstacle to utilizing the full power of synchrotron

sources for FTIR is the phenomenon of channel spectra. Although channel spectra are a common problem in all FTIR spectrometers, the nature of synchrotron sources with their high coherency and complicated transfer optics aggravates the problem. In the following chapter, we will attempt to minimize the effect of channel spectra on the quality of the FTIR spectra recorded using synchrotron sources.

"It is sometimes of great use in natural philosophy, to doubt of things that are commonly taken for granted; especially as the means of resolving any doubt, when once it is entertained, are often within our reach. We may therefore say, that any experiment which leads us to investigate the truth of what was before admitted on trust, may become of utility to natural knowledge."[88]

Sir William Herschel /Astronomer and the discoverer of infrared light.

Chapter 3: Channel Spectra Handling Techniques

3.1: Channel Spectra Handling Techniques

The only option left after exhausting all the possible techniques for preventing channel spectra is to try removing them from the recorded spectrum. The term "correcting" would imply that we can remove the channel spectra completely. However, since we are trying to minimize its impact on the quality of spectra, I will be using the term handling instead. The ultimate goal of any handling technique is to minimize these periodic variations in the baseline of the spectra without distortion of the spectral line parameters such as line shapes, positions and intensities.

In this study, we explored two categories of these handling techniques. The first one attempts to remove the channel spectra by modifying the interferogram to remove the spikes causing channel spectra with the least possible impact on the final spectrum. In the second category, signal processing techniques such as filtering, convolution, and fitting are used separately or in combination to separate the contribution to the recorded interferogram or spectrum from the instrument internal reflections and interferences.

3.2: Interferogram Editing Techniques

These handling techniques utilize the fact that the channel spectra result from localized spikes (sometimes called side bursts) in the recorded interferograms. Removing these features from the interferogram will produce a spectrum free of channel spectra upon Fourier transformation. The removal of problem spikes can be achieved by replacing the interferogram segments containing them with zeros or straight line interpolations [89, 90]. However, this approach has the disadvantage of producing sharp discontinuities in the interferogram, which lead to phase errors [89]. It also causes a loss of spectral information in the severed segment. Another approach for removing these spikes is based on the relationship between peak positions of the channel spectra v_m and the refractive index of the optical component producing them [89]:

$$v_m = \frac{m}{2nd} \tag{3.1}$$

where $m = 0, 1, 2, ...,$ and n is the refractive index of the optical component that produces the channel spectra. Equation (3.1) shows that a small change in the sample thickness d will cause a change in the channel spectra peak position, which results from a shift in the spike's position in the interferogram. In cases where the source of the channel spectra can be traced back to the sample (such as for a thin film sample), slight changes to the sample thickness achieved by titling the sample will make these spikes in the interferogram shift. Replacing the spikes with the corresponding segments from a shifted interferogram will account for the missed information in the spike segments. However, this technique cannot be used in gas

spectroscopy because sources of channel spectra cannot be rotated. In addition, when the source of these channel spectra is not the sample itself, this technique cannot be used. Nevertheless, the simple method of replacing the spikes by zeros or straight lines remains a common practice because the removed segment points usually represent a very small percentage of the interferogram points, especially in high-resolution spectroscopy.

On the other hand, many other techniques attempt to avoid the sharp discontinuities resulting from spike removal. For example, a Gauss reduction function could be used to reduce the amplitude of the spikes while reducing the sharp discontinuities at the edges[20]. Following the same principle, we replaced the spikes by polynomial fits of the spikes. The polynomial fit of the spikes produces a very low resolution image of the spike with much lower amplitude. This curved polynomial line can smooth the sharp transition at the spike boundaries.

We also used the technique introduced by Mellau and Winnewisser [91] to remove channel spectra by producing a synthetic background that contains the same channel spectra as the recorded sample spectrum. This was achieved by editing the sample interferogram, replacing all of it with zeros except at the central burst and the spikes. This modified interferogram was FFT'd to produce a background spectrum that has channel spectra similar to the sample spectrum. Then, the channel spectra should cancel out when we use this background to create the transmission spectrum.

---

[20] Based on personnel communication with Dr. David Naylor, Physics and Astronomy department, University of Lethbridge, Lethbridge, Alberta.

3.3: Signal Processing Techniques

The literature includes many other techniques for handling channel spectra, such as frequency filtering [92, 93] and the utilization of convolution methods to remove them [94, 95]. In this work, we utilized a multispectrum fitting technique that allows the user to analyse several spectra simultaneously over a relatively narrow wavelength interval. The multispectrum fitting technique has advantages such as [96]:

(i) Versatility, as spectra recorded by different techniques or recorded with different resolution can be used,

(ii) Analysis of blended line profiles by including a low pressure spectrum with unsaturated or partially resolved lines, enabling retrieval of the positions and intensities of these lines.

Narrow wavelength intervals are used to avoid any significant refractive index changes within the wavelength range, as these changes will cause changes in the peak position and spacings of channel spectra. Also, the amplitudes of channel spectra show considerable change with wavelength, as a direct result of the wavelength dependence of beam splitter reflectance and transmittance. For example, beam splitters that are free-standing, non-absorbing, parallel-sided, and made of thin dielectric materials have a reflectance R_0 and transmittance T_0 given by [70]:

$$R_0 = \frac{2R^2\,(1 - cos\delta)}{1 + R^2 - 2Rcos\delta} \tag{3.2}$$

$$T_0 = \frac{(1 - R^2)}{1 + R^2 - 2Rcos\delta} \tag{3.3}$$

where $\delta = 4\pi \, \bar{\nu} \, n \, d \, (cos\theta_t)$ is the relative phase shift (in radians) between two adjacent emerging rays, $\bar{\nu}$ is the wavenumber, n is the refractive index, d is the thickness of the film, θ_t is the angle between the beam inside the film to the surface normal, and R is the single-bounce reflectance of the material. This wavelength dependence of the channel spectra peak positions, spacings and intensities complicates the modeling of channel spectra over the complete wavelength range of the recorded spectra. Therefore, within narrow wavelength intervals, we can assume that all optical components have relatively constant refractive indices.

A multispectrum nonlinear least square fitting program is used to fit these segments with initial estimates for the spectral line parameters from the HITRAN database. The complete details of this program can be found elsewhere [96, 97]. In this multispectrum program [96], in order to calculate the fitted spectrum S as a function of wavenumber $\bar{\nu}$, the fitted spectrum is calculated from the continuum [100% transmittance level] $B(\bar{\nu})$, channel spectra $C(\bar{\nu})$, gas spectrum convoluted with the instrumental line shape $b(\bar{\nu})$ and zero level offset z as [96]:

$$S(\bar{\nu}) = B(\bar{\nu})C(\bar{\nu})b(\bar{\nu}) + z \qquad (3.4)$$

The change of the fitted spectrum due to the existence of channel spectra is expressed by the derivative of equation (3.4) using finite differences [96]:

$$\frac{\partial S(\bar{\nu}, q)}{\partial q} \cong \frac{S(\bar{\nu}, q + \epsilon) - S(\bar{\nu}, q)}{\epsilon} \qquad (3.5)$$

Here, q is the parameter with respect to which the derivative is to be taken and ϵ the change in the quantity q, which is small enough that the derivative of S with respect to q is not significantly different at q, and $q + \epsilon$, but large enough to avoid precision

errors during mathematical operations. When fitting the channel spectra parameters, the derivative of the spectrum with respect to the channel spectra parameters is expressed as:

$$\frac{\partial S(\bar{v})}{\partial q} = B(\bar{v})b(\bar{v})\frac{\partial C(\bar{v})}{\partial q} \tag{3.6}$$

Both $B(v)$ and $b(\bar{v})$ are calculated for the nominal case. The channel spectra are calculated using equations equivalent to Niple et al. [98]:

$$C(\bar{v}) = \mu(\bar{v})(Re[b(\bar{v})]\cos[\theta(\bar{v})] - Im\,[b(\bar{v})\sin[\theta(\bar{v})]]) \tag{3.7}$$

$$\mu(\bar{v}) = \sqrt{\left\{1 - \sum_{i=1}^{N_{ch}} a_i\,[1 - \cos\frac{2\pi}{P_i}(\bar{v} - \phi_i)]\right\}^2 + \left\{\sum_{i=1}^{N_{ch}} a_i\,\sin\frac{2\pi}{P_i}(\bar{v} - \phi_i)\right\}^2} \tag{3.8}$$

$$\theta(v) = tan^{-1}\left\{\sum_{i=1}^{N_{ch}} a_i\,\sin\frac{\frac{2\pi}{P_i}(\bar{v} - \phi_i)}{1 - \sum_{i=1}^{N_{ch}} a_i\,[1 - \cos\frac{2\pi}{P_i}(\bar{v} - \phi_i)]}\right\} \tag{3.9}$$

where N_{ch} is the total number of channel spectra and a_i, P_i and ϕ_i are the amplitude, period and phase of channel spectra number i, respectively. The derivatives of the channel spectrum $C(\bar{v})$ can be determined from equation (3.7) and used in the fitting process as shown by Benner [96].

3.4: Implementing the Handling Techniques

As mentioned in previous sections, we divided common channel spectra handling techniques into two groups: i) interferogram editing and ii) signal processing techniques. LabVIEW[21] (version 8) software was used to unify the data handling procedures for the different approaches. Although LabVIEW is historically known to be used in instrumentation applications, its graphical programming

---

[21] LabVIEW stands for Laboratory Virtual Instrument Engineering Workbench

environment and library of signal processing tools are making it increasingly popular in signal processing applications. The data were recorded by the Bruker FTS125HR spectrometer and were stored in the OPUS file format. The OPUS software was used to average the recorded scans and to remove the displaced interferograms, which can cause spurious channel spectra [99]. Next, we used the OPUS software to produce single-side interferograms and save them in the standard data point table (dpt) file format, then used LabVIEW code in figure (3.1) to read it as a number array for processing.

The need to process a large number of residual files resulting from the multispectrum fitting program for the signal processing method discussed earlier poses practical challenges. For example, fitting 24 spectra in a wavelength range of 500 wavenumbers (dividing each spectrum into 5 wavenumber segments) would require processing 2400 residual files. The process of selecting the residual files, naming the results files, and displaying the spectra could be quite time consuming. For this reason, the residual files were processed in batches. A LabVIEW code was written to read all files in the batch folder creating a list of the contents, process the contents, display and save the results automatically and also enable the user to cycle the display through the spectra at an appropriate speed. This LabVIEW code is an intrinsic part of the channel spectra analysis program outlined in Appendix A.

In the interferogram editing approach, single-sided interferogram data were used as input for the LabVIEW program used to find the locations of problem spikes manually as shown in figure (3.2). The manual determination of these locations was

chosen to avoid with confidence any problems with identifying the spikes responsible for the channel spectra and to ensure that the same spike locations are used for every technique. The spike positions were used as input to another LabVIEW channel handling program, whose front panel is shown in figure (3.3) and block diagram in Appendix B. This program contains the six sub-programs presented in Appendix B. Each of these sub-programs processes the data with a different technique and then all the resulting spectra are displayed either overlaid in a single graph or stacked in multiple graphs for comparison, as shown in figure (3.3). The six interferogram editing techniques used are:

1. Replacing the spikes with zeros,

2. Replacing the spikes with a straight line interpolation,

3. Replacing the spikes with polynomial fit for the spikes,

4. Reducing the spike amplitude,

5. Reducing the spikes amplitude by a Gauss reduction function, and

6. Replacing the interferogram points with zeros except for the ZPD and spikes.

In the replacing by zeros sub-program, the spike data point segments were separated using the sub-array routine in LabVIEW. These sub-array routines in LabVIEW replace the segments of the interferogram defined by the spike limits with zeros. In the replacement by straight line sub-program, a procedure similar to the one used in the previous sub-program was used. The spike segments were replaced by straight lines interpolated between their limits employing the curve fitting procedure in LabVIEW, whose configuration window is shown in Appendix B7.
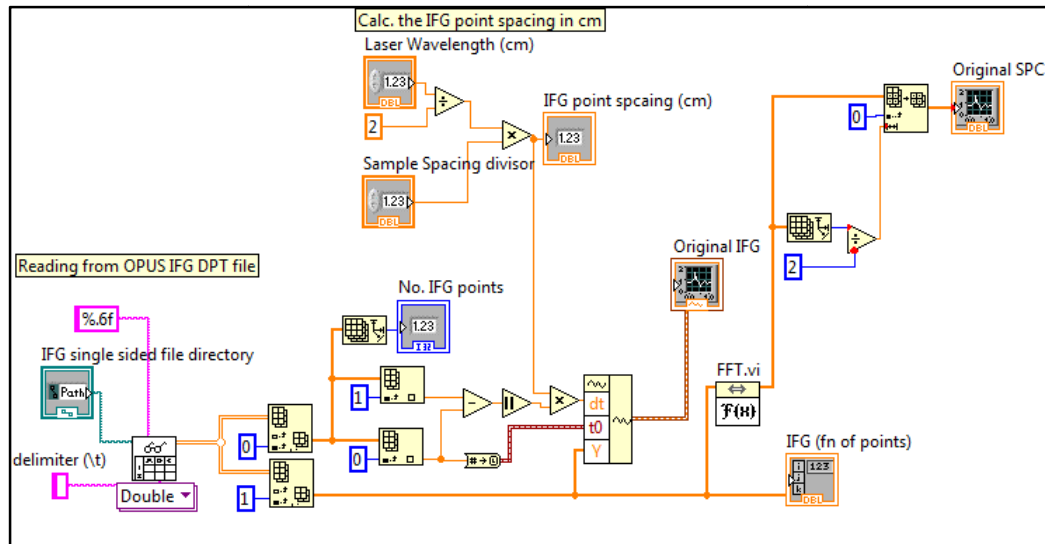
Figure (3.1): The block LabVIEW program used in reading data from OPUS and manually estimating spike locations.
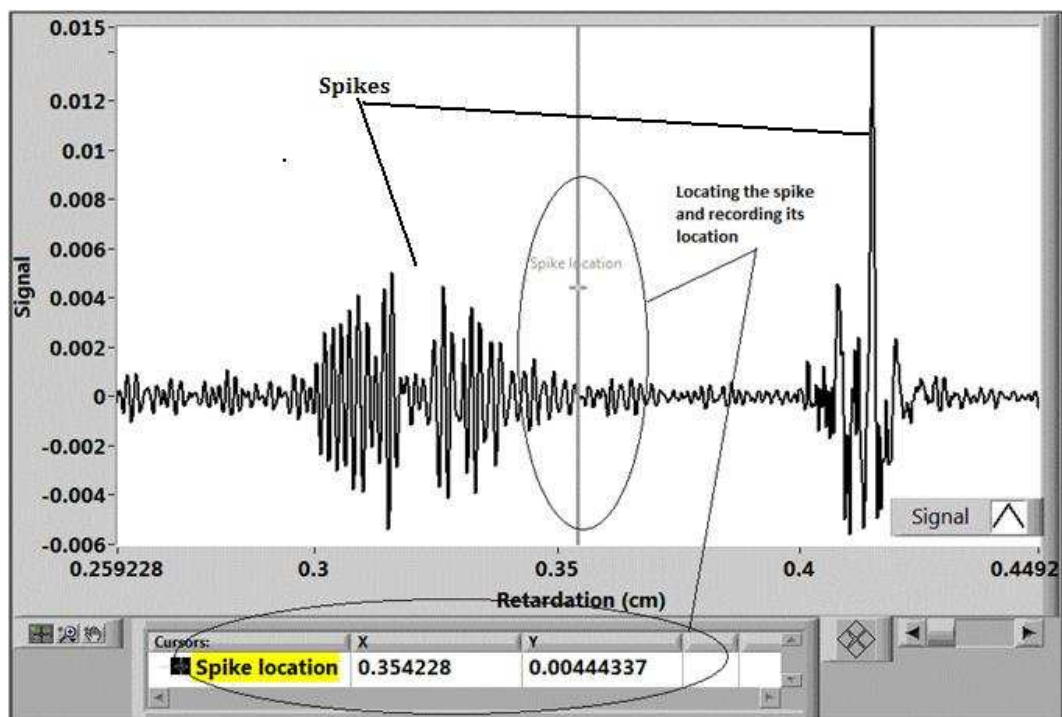
Figure (3.2): Graphical interface of the LabVIEW program used in reading the data file from OPUS and estimating the spike locations manually.

56
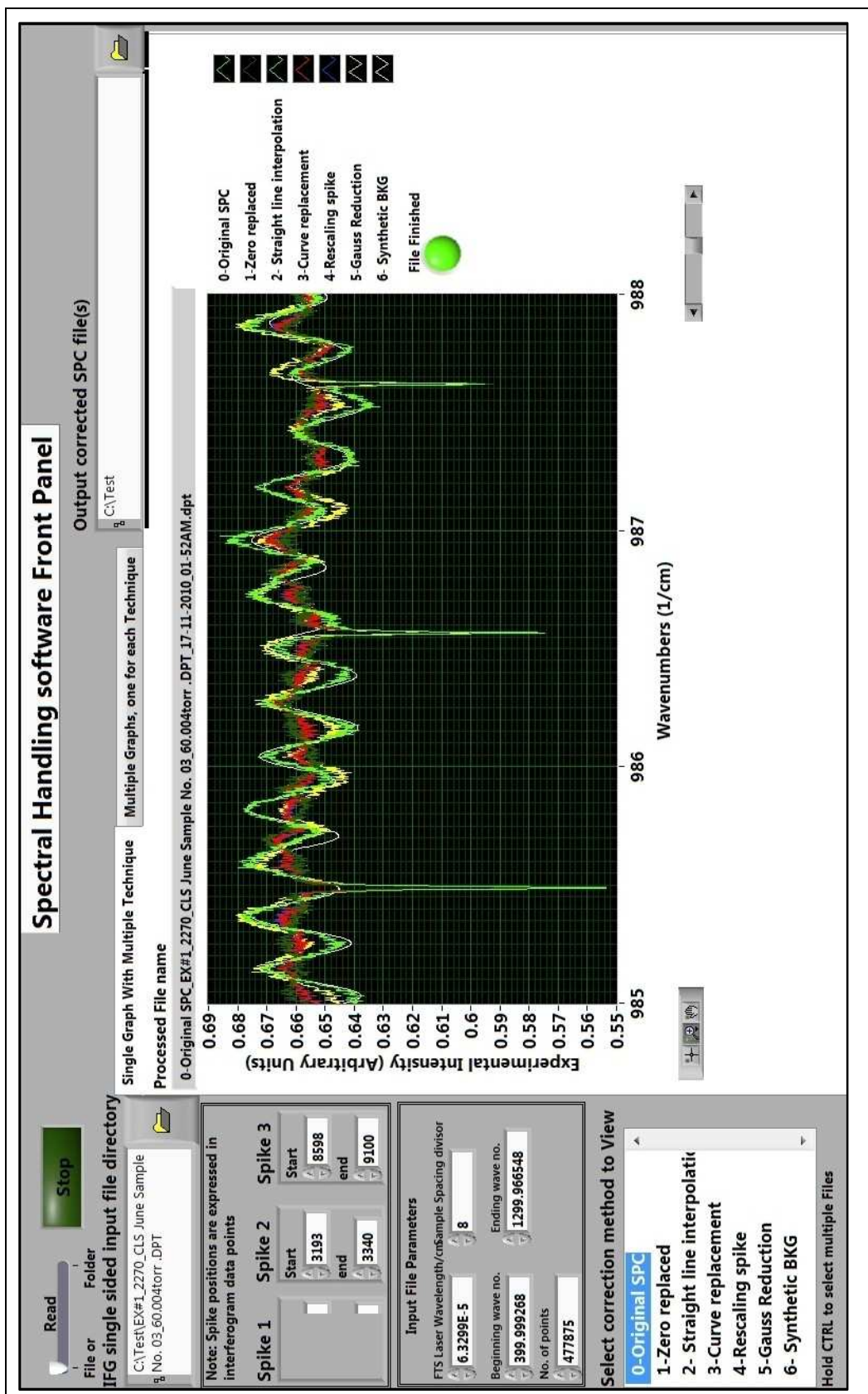
Figure (3.3): Front panel of the LabVIEW channel handling program.

In the polynomial fit sub-program, each problem spike segment was fitted using a polynomial function. Also, the peak-to-peak amplitude of the region around the spike was calculated and averaged and then used to rescale the fitted polynomial curve so that it matched the surrounding interferogram segment. The resulting polynomial fitted curve was used to replace the problem spikes. A similar program to the previous one was used to rescale the spike amplitude and reduce it to the levels of the neighbouring interferogram segment. This rescaled spike replaced the original spike in the interferogram. In the Gauss reduction sub-program, the spike segments were extracted from the interferogram and, using an asymmetrical Gaussian window routine in LabVIEW with the spike segment points X as input, we produced modified segments Y fitted to Gaussian curves using[22]

$$Y_i = X_i\, e^{\left[-\frac{(i-m)^2}{2(\sigma n)^2}\right]} \qquad for\ i = 0, 1, \dots, n-1 \qquad (3.10)$$

where n is the number of elements in X, $m = (n-1)/2$ and σ is the standard deviation of the Gaussian window. The new segment was subtracted from the spike to produce a Gauss reduced spike that replaced the original one. The same steps were applied to all of the problem spikes. An example of a problem spike that was handled by all the previous techniques is shown in figure (3.4). Finally, the synthetic background sub-program produced a background spectrum with identical spikes by replacing the interferogram points, except the ZPD and problem spikes, with zeros. The resulting background spectrum, as shown in figure (3.5), was used to create a transmission spectrum with reduced channel spectra.

---

[22] National Instruments, "Characteristic of Different Smoothing Windows", http://zone.ni.com/reference/en-XX/help/371361B-01/lvanlsconcepts/char_smoothing_windows/
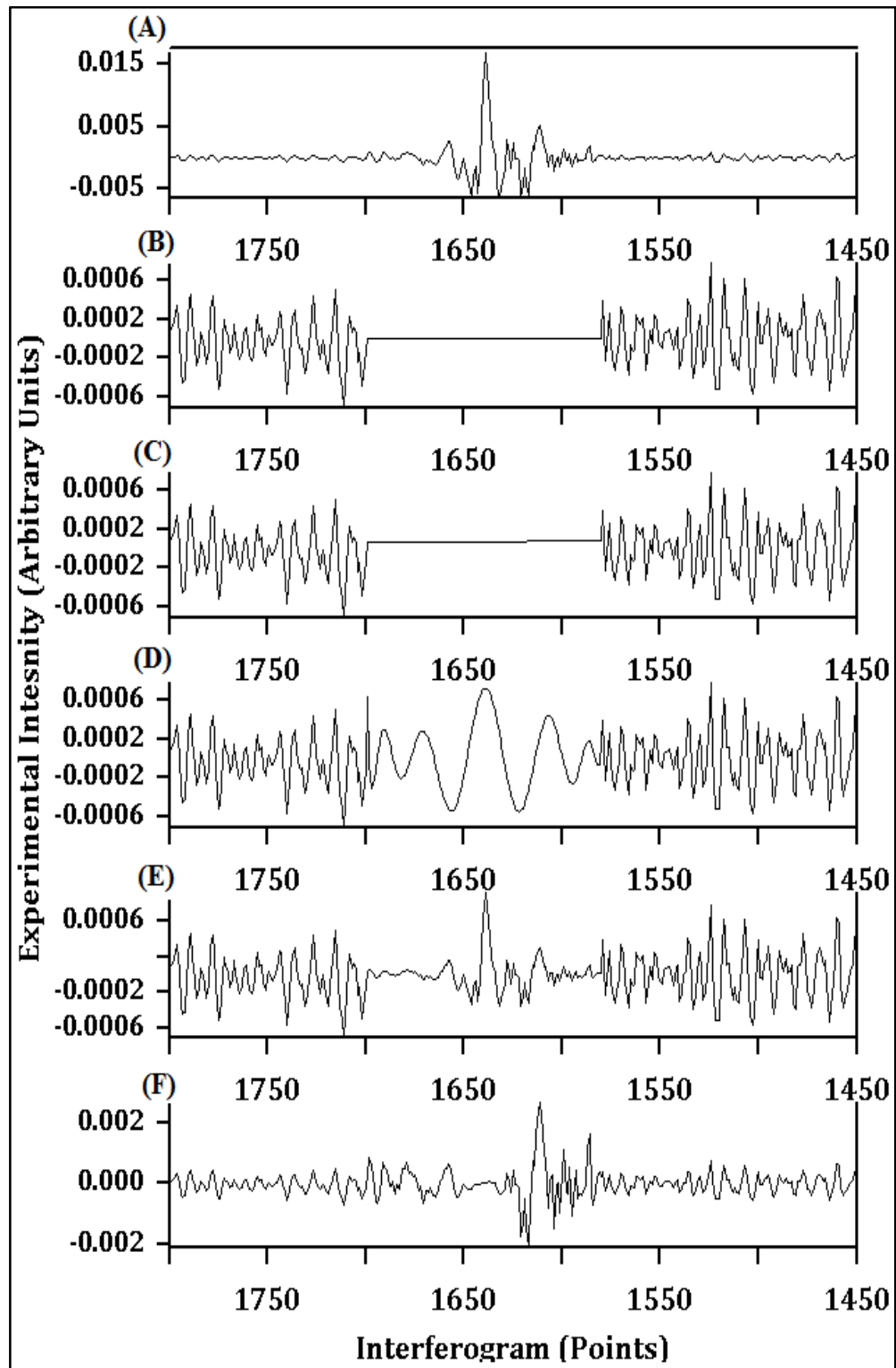
Figure (3.4): (A) Original problem spike, (B) replaced by zeros, (C) replaced by a straight line, (D) replaced by a polynomial curve fit (E)reduced in amplitude and (F) reduced by a Gauss function.
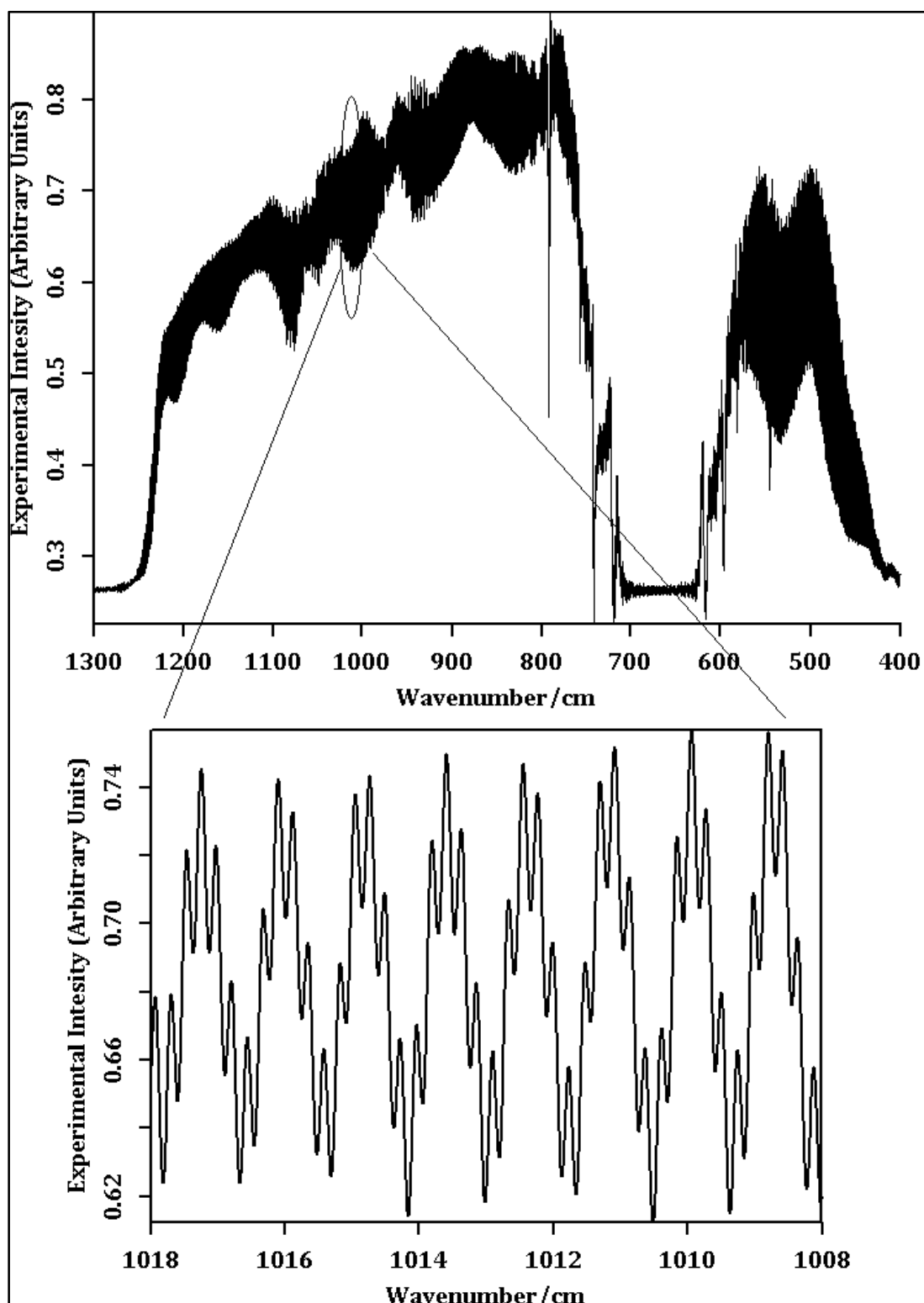
Figure (3.5): Synthetic background produced from the sample interferogram.

60

In the signal processing technique, the data were initially fitted using data from the HITRAN database using the nonlinear least square algorithm described earlier. The resulting fitting residuals have the channel spectra structure. These residual files were analysed using a LabVIEW program that I developed and its interface is shown in figure (3.6). The program uses a sub-program (called "vi" or "virtual instrument" in LabVIEW) that employs a Fast Fourier Transform (FFT) to transform these residuals from the time domain to the frequency domain. Next, the program isolates frequency components with amplitude higher than a user-specified threshold. These threshold limits are used to avoid measuring the noise components, and to limit measurements to channel spectra only. After isolating the targeted frequency components, the LabVIEW subroutine estimates the individual amplitude, frequency, and phase for each channel separately. The phase is expressed in terms of wavenumbers by using a subprogram that simulates the individual channel spectra using the calculated parameters and estimates the beginning of the channel waveform in wavenumbers as the phase of the channel[23]. This LabVIEW program is listed in Appendix A. These estimated parameters were implemented in the fitting program to model the channels and refit the spectrum intervals again, using the corresponding channel parameters for each interval. For convenience, the program writes the output parameters in a folder name with time stamp and in a format compatible with the input file of the fitting program.

---

[23] Based on personal communication with Dr. Chris Benner, Research Associate Professor of Physics, College of William & Mary, Virginia, USA.
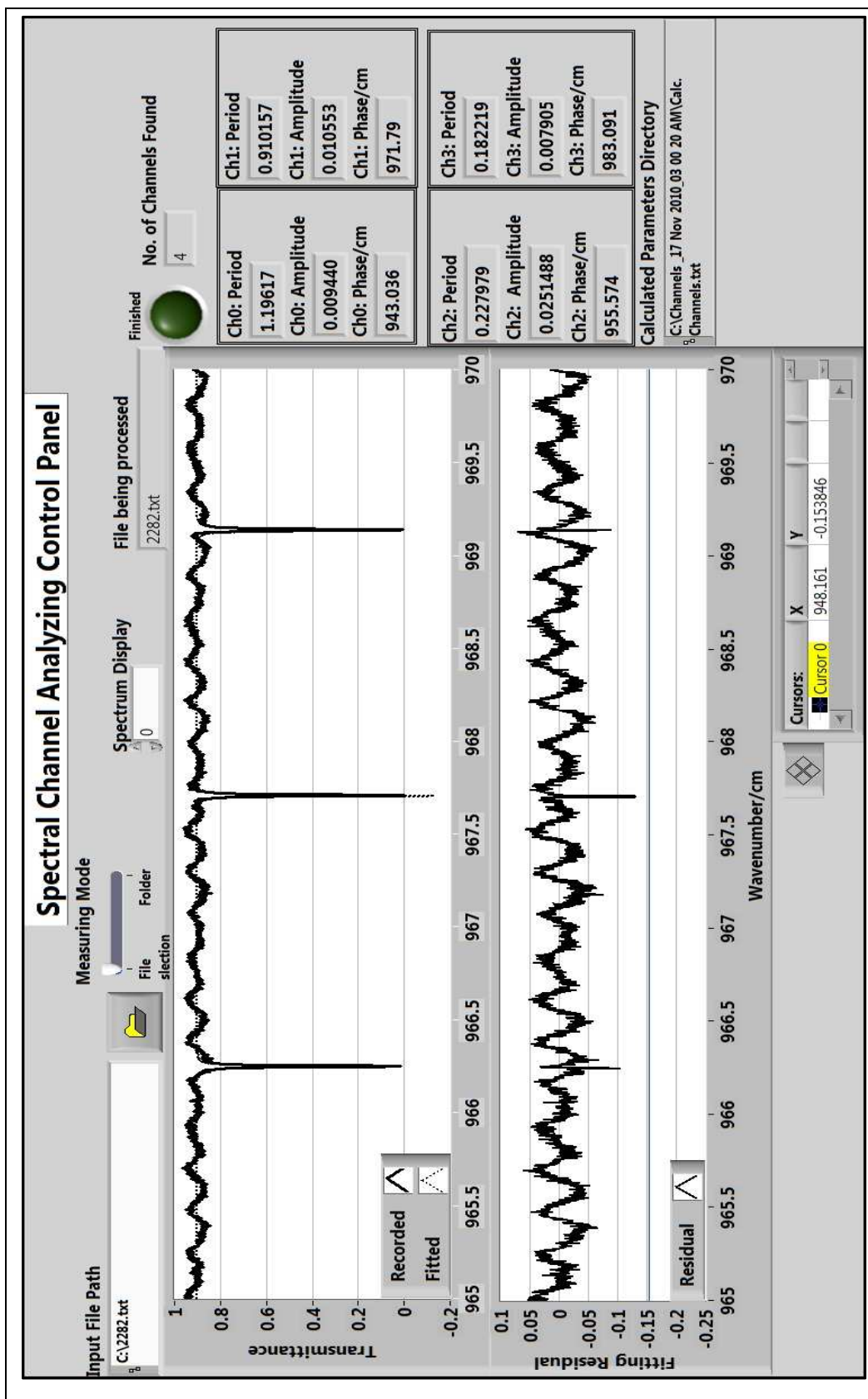
Figure (3.6): Front panel of LabVIEW spectral channel analyzing program.

3.5: Testing and Comparing Handling Techniques

The six different interferogram editing techniques plus the spectral fitting technique discussed in the previous section are listed with brief descriptions in table (3.1). For simplicity, in the following sections, each technique is labelled in the graphs and results with its corresponding technique number.

Table (3.1): Brief description of tested channel handling techniques.

Tech. no.	Method description
0	No channel handling technique is applied
1	Replacing the spikes with zeros
2	Replacing the spikes with a straight-line interpolation
3	Replacing them with a polynomial fit for the spikes
4	Rescaling spikes
5	Reducing spikes by a Gauss function
6	Using synthetic background
7	Fitting channel spectra

3.5.1: Handling technique effects on SNR

As mentioned earlier, the SNR is considered to be an indicator of the quality of the measured spectra. The SNR in any spectrum is related to the noise in the interferogram. This relation between the interferogram noise and the spectrum noise is called Parseval's theorem. It states that energy in a finite signal is the same when calculated in the interferogram space or its reciprocal Fourier space and stated mathematically as

$$E = \int_{-\infty}^{\infty} |B(v)|^2 \ dv = \int_{-\infty}^{\infty} |I(x)|^2 \ dx \qquad (3.11)$$

where $B(v)$ is spectrum as function in wavenumber v and $I(x)$ is interferogram as function in retardation x. However, this work aims to use SNR as an indicator of the

reduction in channel spectra rather than studying noise itself. Therefore, no interferogram domain noise is measured. In order to test the channel handling techniques, we developed a LabVIEW program to calculate the SNR of the spectra handled for channel spectra. The front panel of the program is shown in figure (3.7), while its program code (block diagram) is in Appendix C. To calculate SNR, the program reads the transmission spectra and calculates SNR as the standard deviation of the data at base line points divided by the average of these data within pre-specified intervals. The program calculates the SNR at pre-specified intervals between spectral lines in order to avoid calculation errors when lines broadened at high pressure are included in the SNR interval. Our calculation used the baseline of the transmission as the signal (ideally $= 1$) to study the change of SNR with wavelength. On the other hand, if an absorption line is used as the signal, there is a complicated dependence of SNR on the line intensity and in turn the sample pressure and concentration. This dependence will not allow us to compare SNR throughout the spectral range and between different samples.

In order to study the effect of handling techniques on spectra with different line parameters, seven synchrotron source spectra were chosen for comparisons. A detailed description of these sample spectra is listed in table (3.2) and the experimental settings of the measurements are shown in table (3.3). Because samples #1 and #2 were at lower pressure and, in turn had narrower absorption lines, they were recorded with slightly higher spectral resolution. However, a wider aperture for lower spectral resolution samples enabled us to increase the signal and compensate for attenuation by higher pressure sample absorption. The recorded

scans were averaged after removing faulty scans that can result during the filling of

the Ge:Cu detector with liquid helium, synchrotron electron beam injection or

spectrometer malfunction. The removal of faulty scans and the relatively long scan

time for high resolution, while available synchrotron beam time is restricted[24], are

the reasons for the inconsistency in the number of averaged scans in table (3.2).

Samples with a larger number of averaged scans have higher SNR if all other

conditions are the same. All channel handling techniques (except method #7) were

applied to every spectrum and the SNR before and after channel handling was

calculated. Method #7 was not included in the SNR analysis because it did not

modify or change the original spectrum but helped to better model of it. A section of

sample #1 handled spectra is shown in figure (3.8).

Table (3.2): Description of spectra used in handling technique comparison.

No.	Sample	Recorded mm/yyyy	Pressure (Torr)	Temp. (°C)	Resolution cm^{-1}	Aperture (mm)	No. of scans averaged
1	CO_2+Air	June2008	60.004	23.4	0.003	1.5	289
2	CO_2+Air	June2008	90.010	23.33	0.003	1.5	304
3	CO_2+Air	Nov.2008	201.09	23.31	0.004	1.7	347
4	CO_2+Air	Nov.2008	300.12	23.21	0.004	1.7	423
5	CO_2+Air	Nov.2008	450.42	23.55	0.004	1.7	461
6	CO_2+Air	Nov.2008	525.00	23.82	0.004	1.7	558
7	CO_2+Air	Nov.2008	825.01	23.88	0.004	1.7	472

Table (3.3): Experimental settings used in recoding the CLS spectra[25].

Cell base length [a]	2 m	Detector	Ge:Cu (300-1850 cm^{-1})
Optical path length[b]	72.15 m	Detector filter	490-1190 cm^{-1}
Windows (range)	KBr(400-5000 cm^{-1})	Beam splitter	Ge/KBr (400-4800 cm^{-1})
Spectral range	450-1200 cm^{-1}	Scan velocity	40 KHz

[a]Cell used is of White optical design
[b]Accurate optical path length calculated using reference spectral line[26]

[24] CLS allocates research time for approved proposals each operation cycle (6 months) in advance.
[25] From CLS Far-IR experimental work sheet by Dr. Brant Billinghurst, CLS, Saskatoon, Canada
[26] Personal communication with Dr. Malathy Venkataraman, College of William & Mary, Virginia, USA
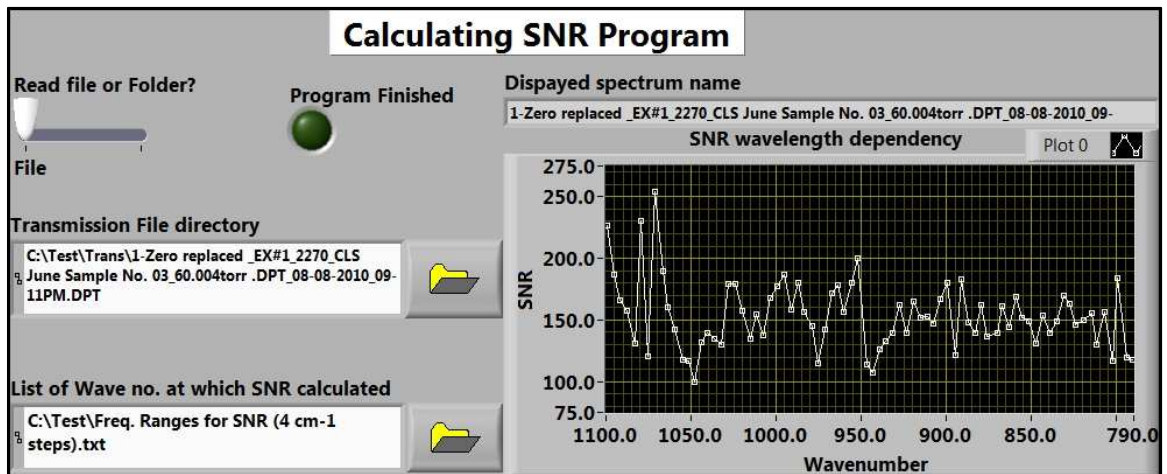
Figure (3.7): Front panel of LabVIEW SNR calculating program.
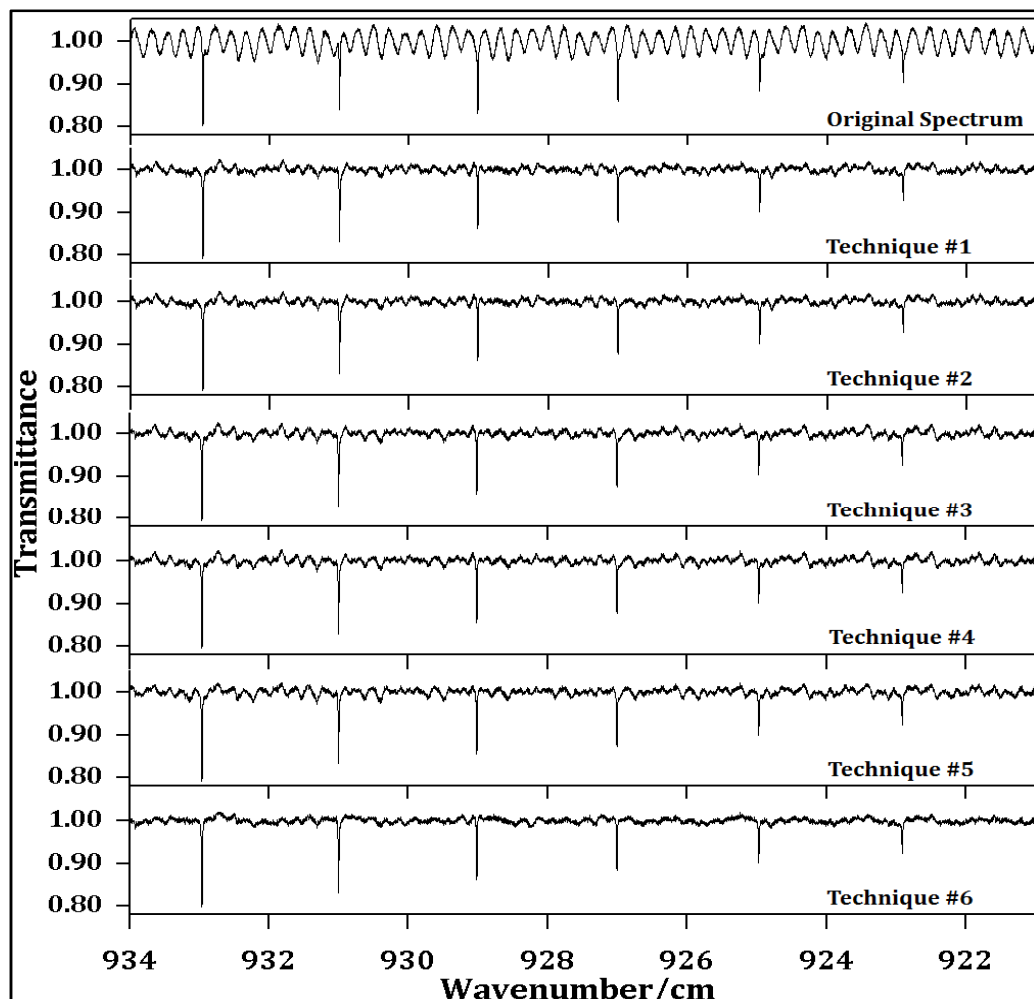
Figure (3.8): Section of the original and handled spectra using interferogram editing techniques #1 to #6.

It is difficult to show the difference between results from the different handling techniques by examining the stacked spectra of sample #1 shown in figure (3.8). However, the ratio change between handled and original spectra SNR [(SNR after handling/SNR before handling)*100] shown in figure (3.9) can provide us with some useful observations. All spectra SNR seem to be dependent on the wavelength, which can be attributed to the channel spectra amplitude dependence on wavelength [see equations (3.1), (3.2) and (3.3)]. Also, figure (3.9) shows that technique #6 (synthetic background) is achieving relatively better improvements compared to the other techniques. For example, the increasing in SNR of example #1 spectrum handled by technique #6 was[27] 18%, 18%, 34%, 33% and 47% higher than techniques #1 to #5, respectively. We can also notice that techniques #1 and #2 produce almost the same results, as expected since they are quite similar techniques. Examining sample #2 to #7 spectra in figures (3.10), (3.11) and (3.12), we see that technique #6 has better SNR improvement in all samples except sample #7. This difference for sample #7 can be attributed to imprecision in the spike locations, which results in a synthetic background with different channels of the sample spectrum. Improvements in technique #6 could be achieved by iteration of changing spike positions and ranges until optimum simulation of the sample channel spectra is achieved by increasing the SNR to maximum value.

Although SNR is an important quantity for measuring the quality of spectra, it does not give any information about the impact these spectral handling techniques have on the retrieved spectral parameters. Since techniques #1 to #6 involve

---

[27] Calculated as: [(tech.#6 SNR increase)-(tech.#1 SNR increase)]*100/(tech.#1 SNR increase)

modifying either the sample or the background interferogram, which alters its information content, another method to compare and test handling techniques with respect to the retrieved spectral parameters was performed.
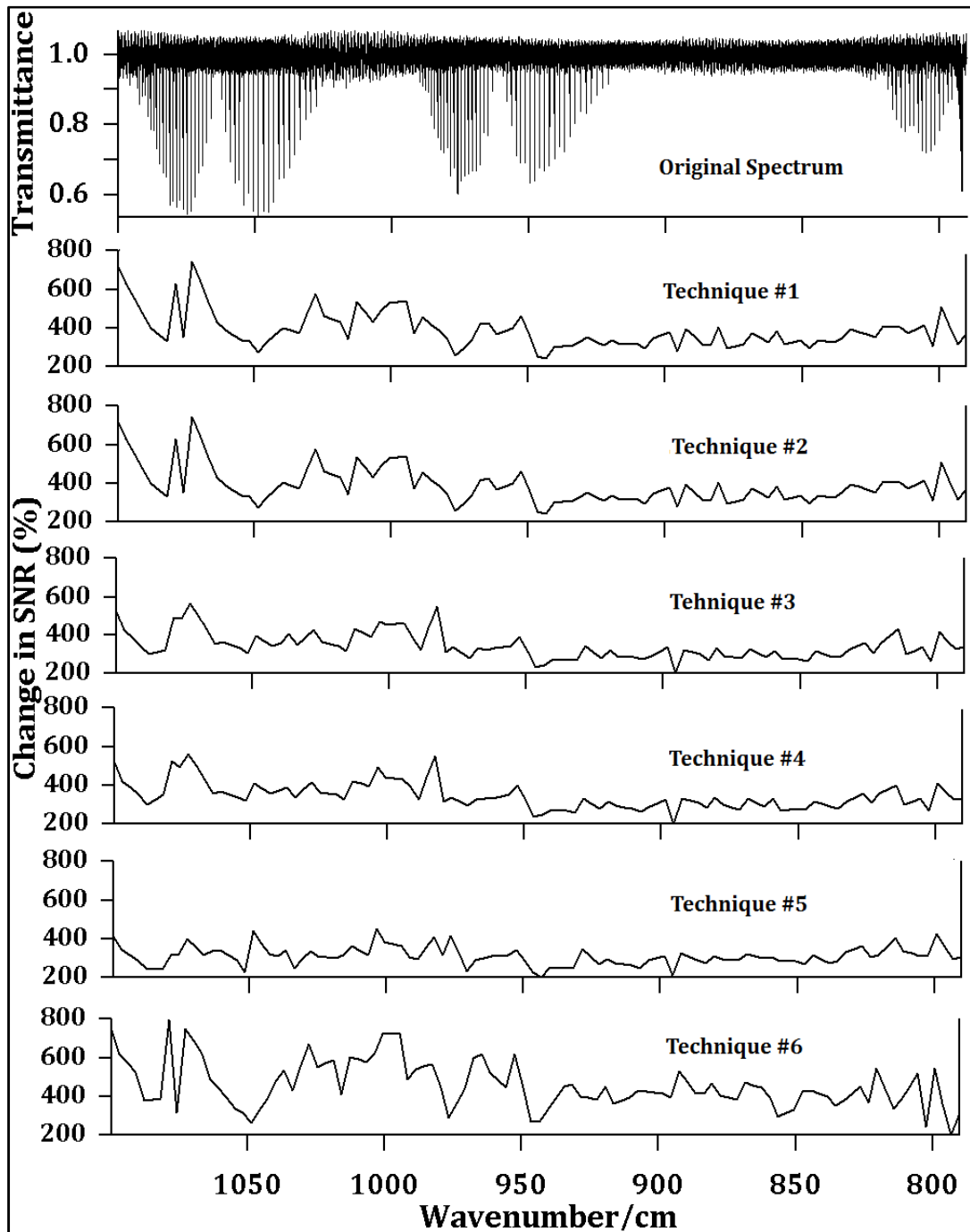
Figure (3.9): Change in the SNR of the spectra of sample #1 handled for channel spectra using interferogram editing techniques.

68
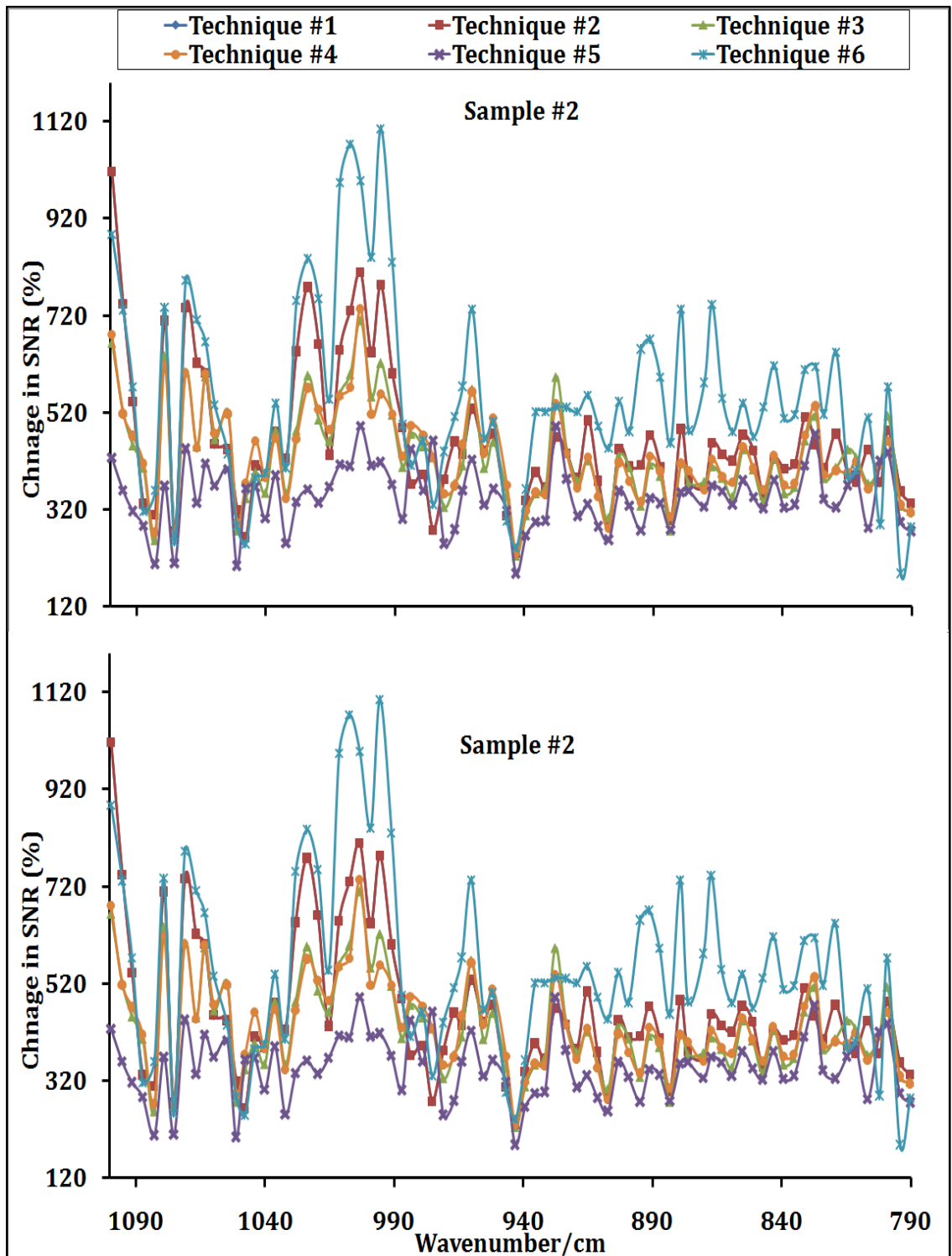
Figure (3.10): Change in SNR with interferogram editing techniques for sample #2 and sample #3.
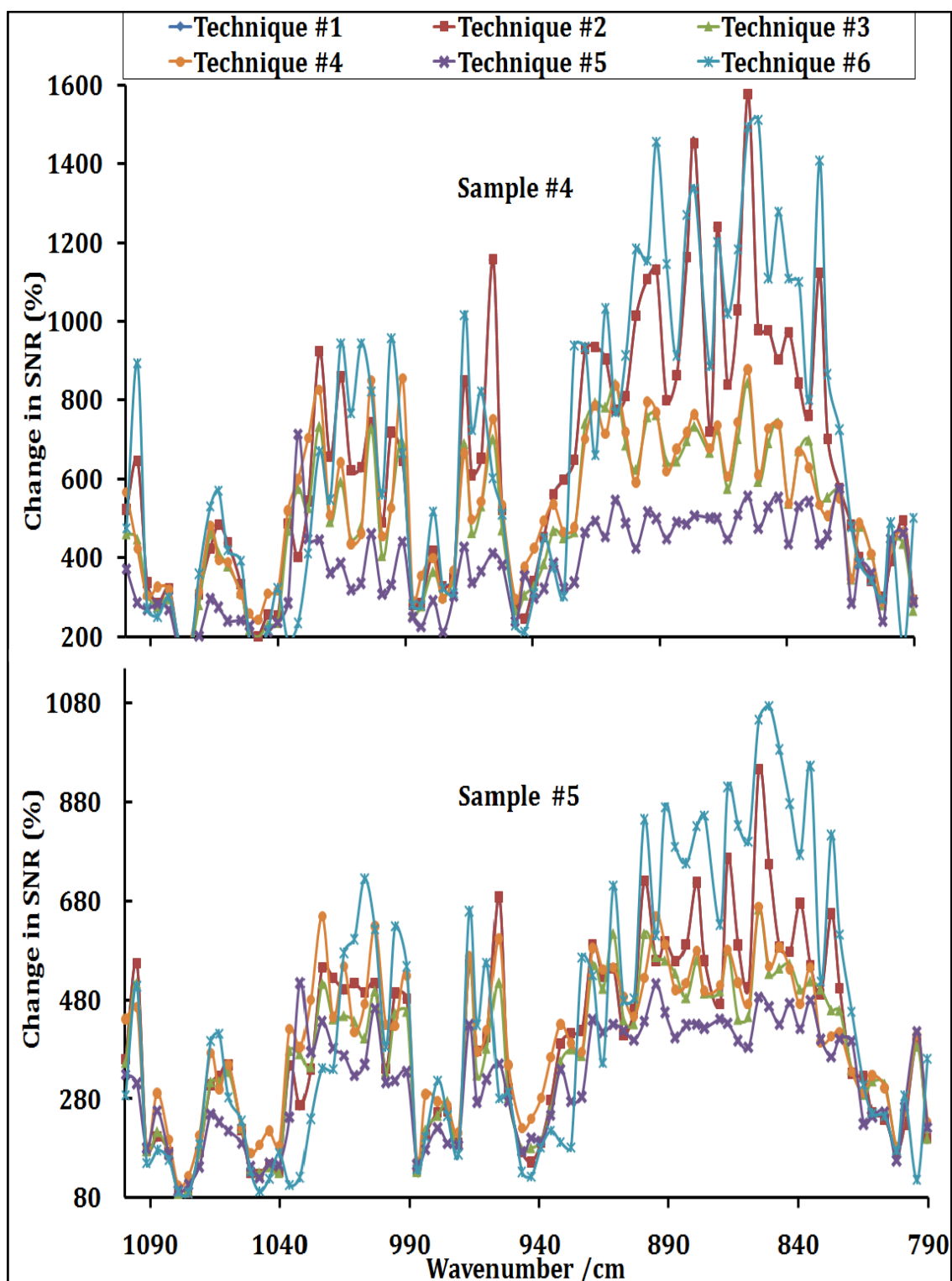
Figure (3.11): Change in SNR with interferogram editing techniques for sample #4 and sample #5.
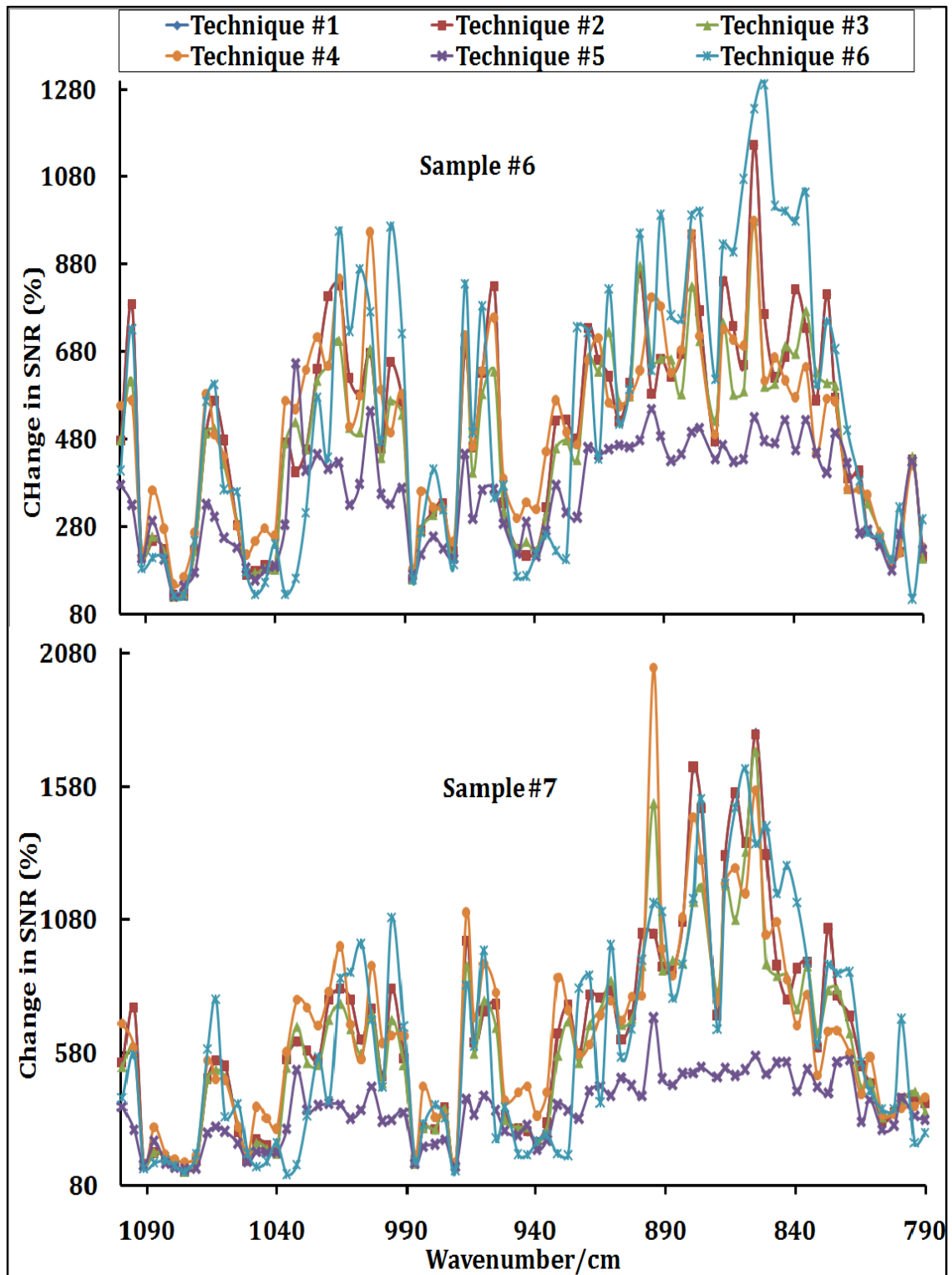
Figure (3.12): Change in the SNR with interferogram editing techniques for sample #6 and sample #7.

3.5.2: Handling technique effects on spectral parameters

Measured spectra are usually used in multispectrum fitting software to retrieve spectral parameters. The fit quality and accuracy of retrieved parameters can be used as an estimate of the impact of the handling techniques on the spectra. In order to compare all handling techniques, eight different groups of spectra were created, each containing the same seven spectra in table (3.2) but processed with a different channel spectra handling technique. The first group (#0) contains the seven original spectra; the second to the seventh groups (#1 to #6) contain the same samples handled with techniques #1 to #6 consecutively [see table (3.1)]. Group seven (#7) contains again the original spectra but fitted using channel spectra parameters calculated from the program in Appendix A as detailed in section (3.3). Since fitting a wide spectral range for channel spectra is difficult, the full spectral range (794.9 to 827.3 cm^{-1}) of interest was divided into six small spectral ranges (~5.4cm^{-1} each) and fitted separately. The fit quality is represented by the standard deviation (STDV) of the measured spectra from the modeled fit solutions listed in table (3.4) and the residuals for region #1 shown in figure (3.13). Both indicate that technique #7 has much lower STDV and therefore has better fit.

Table (3.4): STDVs of spectral fits in different channel handling techniques.

Group / Range	Range #1 (794.9-800.5)/cm	Range #2 (800.5-806)/cm	Range #3 (805.5-811.5)/cm	Range #4 (811.4-816.5)/cm	Range #5 (816.3-821.5)/cm	Range #6 (821.4-827.5)/cm	Full Range STDV
Group #0	2.189%	2.166%	2.122%	2.109%	2.062%	2.074%	2.138%
Group #1	1.045%	1.053%	0.877%	0.830%	0.663%	0.583%	0.872%
Group #2	1.045%	1.053%	0.877%	0.830%	0.633%	0.583%	0.872%
Group #3	1.053%	1.029%	0.807%	0.868%	0.706%	0.647%	0.876%
Group #4	0.997%	1.037%	0.811%	0.838%	0.722%	0.677%	0.873%
Group #5	0.992%	1.187%	0.911%	0.981%	0.737%	0.719%	0.941%
Group #6	1.068%	1.114%	0.860%	0.785%	0.596%	0.526%	0.890%
Group #7	0.521%	0.594%	0.517%	0.561%	0.523%	0.487%	0.622%
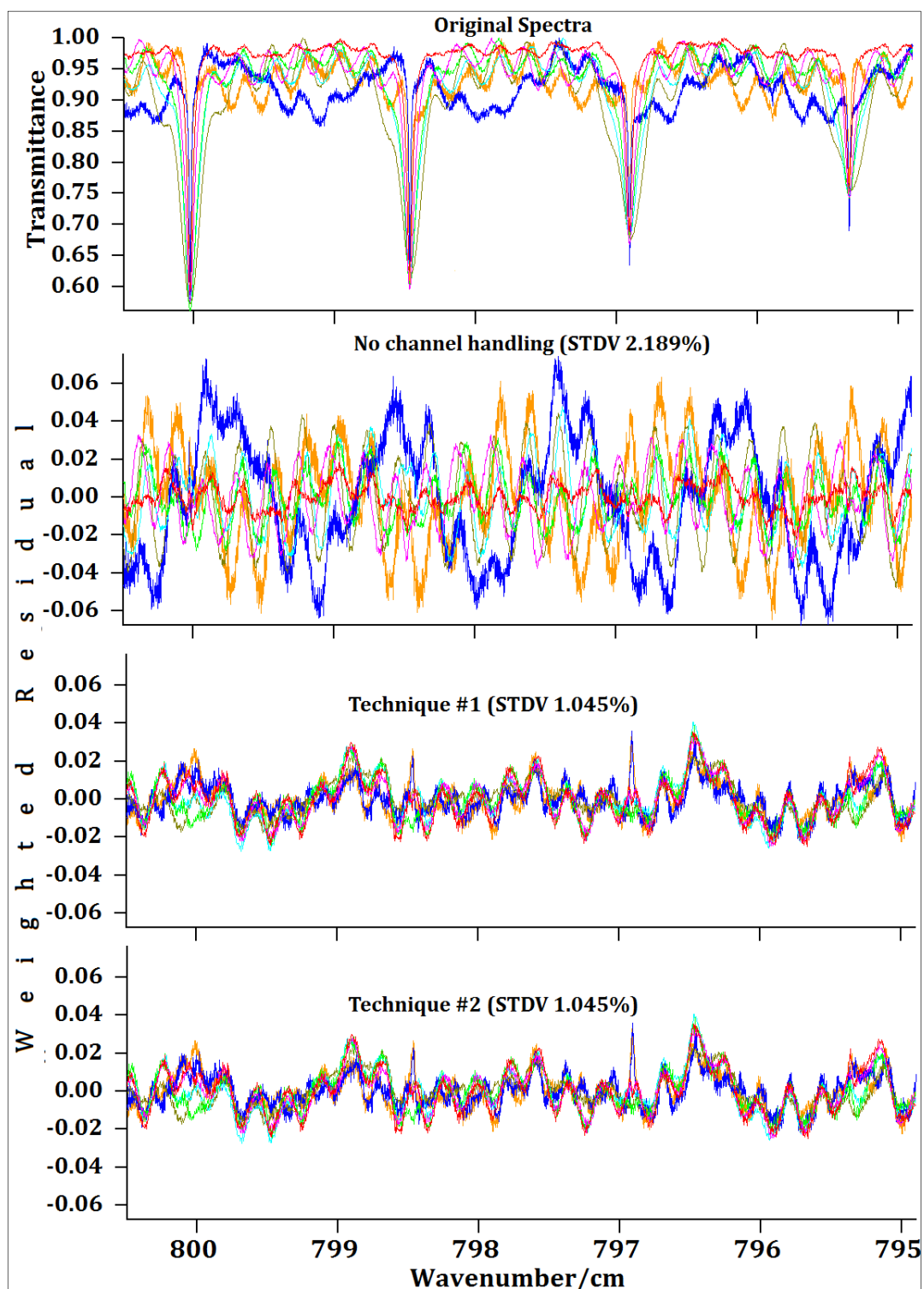
Figure (3.13): (A) Seven original spectra and their fitting residuals when techniques #1 and #2 are used to handle channel spectra.
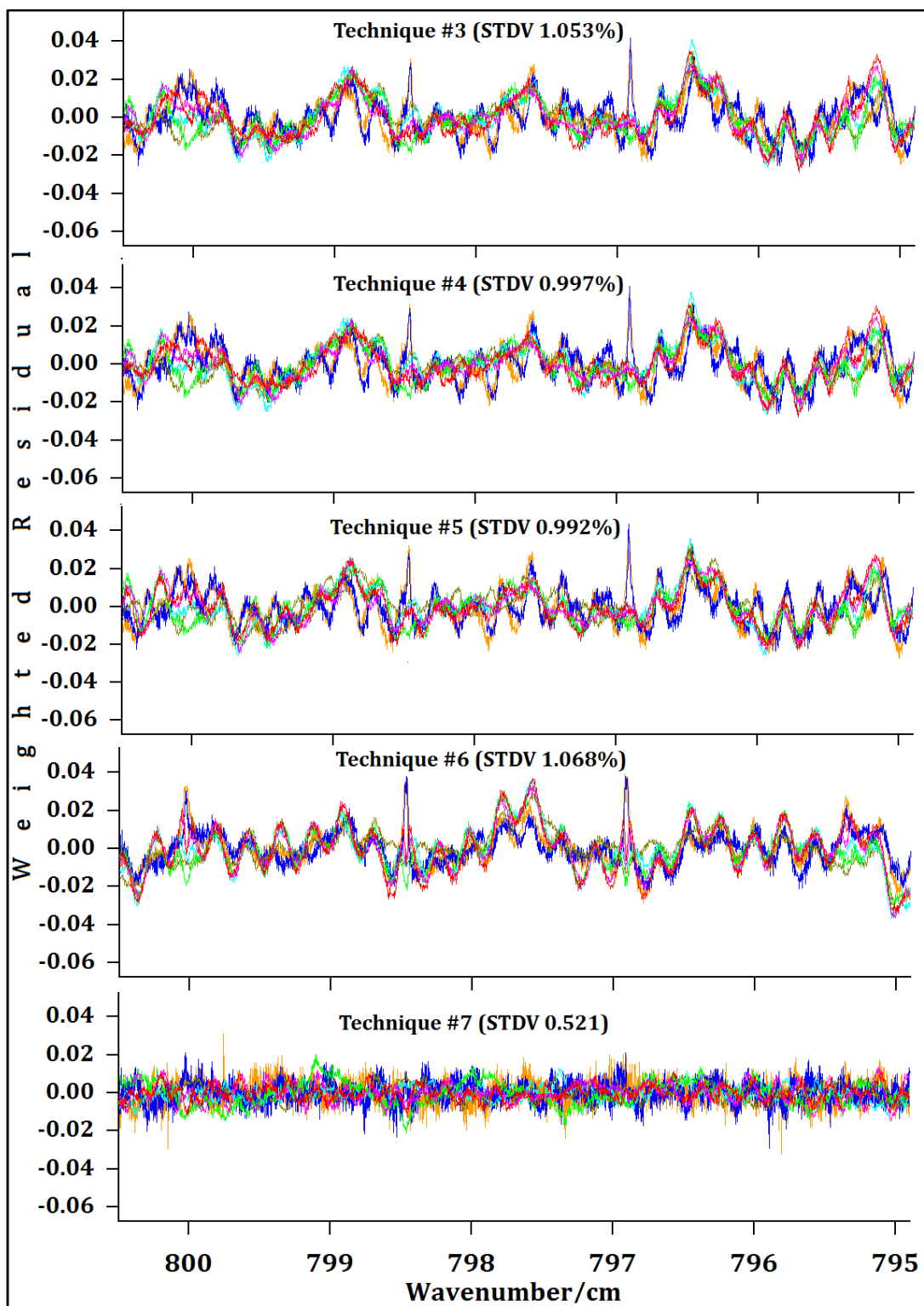
Figure (3.13): (B) Fitting residuals[28] spectra handled by techniques #3 to #7.

---

[28] Residuals are calculated as observed – calculated

The percentage changes between the fit residual STDV for spectra handled for channel spectra from original spectra fit residual STDV in each of the six ranges considered in our discussion are presented in table (3.5) and figure (3.14). Technique #7 (fitting channel spectra) shows the largest reduction in the STDV of the modeled solution, indicating that this technique reproduces the original spectra better than other techniques. Figure (3.14) also shows that the amount by which the fit STDV is reduced can vary considerably with the spectral range for all techniques except for technique #7. For all techniques, the STDV values plotted in Figure (3.14) vary in a sinusoidal fashion similar to channel spectra, which could be an indication of residual channel spectra.   However, the accuracies of the retrieved line parameters, such as line position, intensity and air broadening, are the main objective of the fit. The average percentage deviations from HITRAN values for line positions, intensities and air-broadening coefficients retrieved using spectra handled by each technique are listed in Table (3.5).

Line positions did not show noticeable changes from HITRAN08 values and retrieved values for individual lines are listed in table (3.6). However, for intensity and air broadening, there are changes from HITRAN08, which are listed in tables (3.7) and (3.8), respectively. Regarding intensity, retrieved lines using technique #7 spectra was the most accurate and in average deviating 3.28% from HITRAN. Similarly retrieved air broadening using technique #7 spectra were the most accurate to HITRAN with 4% average deviation.   Knowing that HITRAN08's uncertainty limits for intensities are $\geq 2\%$ and $< 5\%$, and $\geq 5\%$ and $< 10\%$ for air-broadening, these results indicate that the channel handling technique did not cause

any degradation in the quality of retrieved spectral parameters. The deviation of individual lines retrieved intensity and air-broadening from HITRAN values using different channel spectra handling techniques are shown in graph (3.15). An examination of table (3.5) and figure (3.15) indicates that all techniques reduce the retrieved intensity considerably with exception of technique #7, which also produced air-broadening coefficients that are more accurate compared to HITRAN.
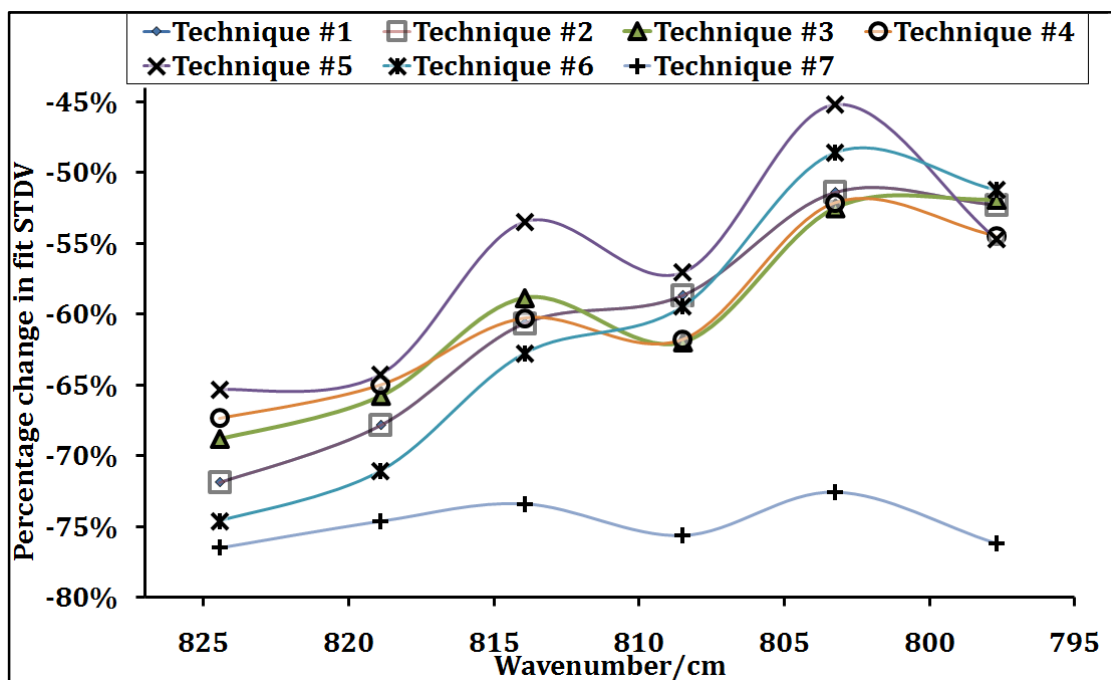
Figure (3.14): Percentage change[29] in the fits STDV for different channel handling techniques from no channel handling case in all spectral ranges.

Table (3.5): Average deviation of retrieved line parameters from HITRAN values.

Parameter	Average of [(Retrieved line −HITRAN)/HITRAN]*100							
Technique no.	#0(%)	#1(%)	#2(%)	#3(%)	#4(%)	#5(%)	#6(%)	#7(%)
Position ×10^{-5}	704	855	855	680	858	779	425	400
Intensity	5.23	35.4	35.4	35.1	34.3	34.5	34.1	3.29
Air broadening	8.09	12.4	12.4	12.3	14.4	15.7	12.7	4.01

[29] Percentage change is calculated as [[STDV(channel handled)-STDV(no channel handling)]/ STDV(no channel handling)] *100 for each spectral range

Table (3.6): Retrieved line positions.

Assignment	HITRAN08 /cm	Technique #0 /cm	Technique #1 /cm	Technique #2 /cm	Technique #3 /cm	Technique #4 /cm	Technique #5 /cm	Technique #6 /cm	Technique #7 /cm
R4	795.35038(1)	795.35121(34)	795.3492(32)	795.3492(32)	795.34948(32)	795.34967(30)	795.35003(29)	795.34999(34)	795.34998(8)
R6	796.91035(1)	796.91107(26)	796.90975(27)	796.90975(27)	796.90989(26)	796.90972(25)	796.91017(25)	796.90976(29)	796.90961(6)
R8	798.46973(1)	798.47045(22)	798.46956(24)	798.46956(24)	798.46954(23)	798.46945(22)	798.46965(22)	798.46919(25)	798.46941(5)
R10	800.02852(1)	800.02925(19)	800.02887(21)	800.02887(21)	800.02877(21)	800.02876(20)	800.02884(20)	800.02817(22)	800.02823(5)
R12	801.58677(1)	801.58604(17)	801.58702(19)	801.58702(19)	801.587(19)	801.58704(19)	801.58672(22)	801.58664(20)	801.58666(5)
R14	803.14451(1)	803.14398(17)	803.14531(19)	803.14531(19)	803.14538(19)	803.14535(19)	803.14511(22)	803.14486(19)	803.14448(4)
R16	804.70181(1)	804.70088(17)	804.70174(18)	804.70174(18)	804.70191(18)	804.702(18)	804.70181(21)	804.70196(19)	804.70138(4)
R18	806.25873(1)	806.25855(17)	806.25843(14)	806.25843(14)	806.25841(13)	806.25846(13)	806.25876(15)	806.25841(14)	806.25835(4)
R20	807.81536(1)	807.81519(17)	807.81511(15)	807.81511(15)	807.81511(14)	807.81502(14)	807.81541(15)	807.81497(15)	807.81493(4)
R22	809.37177(1)	809.37195(17)	809.3713(17)	809.3713(17)	809.3712(15)	809.3712(15)	809.37142(17)	809.37123(16)	809.3715(4)
R24	810.92809(1)	810.92862(19)	810.92844(16)	810.92844(16)	810.92823(15)	810.92788(15)	810.92826(17)	810.92808(16)	810.92782(4)
R26	812.48442(1)	812.48403(19)	812.48533(18)	812.48533(18)	812.48512(18)	812.48495(18)	812.48465(21)	812.48457(16)	812.48424(5)
R28	814.04089(1)	814.04007(21)	814.04185(19)	814.04186(19)	814.04184(20)	814.04183(19)	814.04192(23)	814.04118(18)	814.04059(5)
R30	815.59764(1)	815.59704(24)	815.59799(20)	815.59801(20)	815.59826(22)	815.59829(21)	815.59832(25)	815.598(19)	815.5973(6)
R32	817.15481(1)	817.15485(30)	817.15512(19)	817.15512(19)	817.15496(20)	817.15502(21)	817.15545(22)	817.15505(17)	817.15448(7)
R34	818.71258(1)	818.71313(36)	818.71264(22)	818.71264(22)	818.7124(23)	818.71236(23)	818.71299(24)	818.71267(20)	818.71224(8)
R36	820.2711(1)	820.27262(38)	820.26932(30)	820.26932(30)	820.26903(30)	820.26906(31)	820.26973(30)	820.26991(26)	820.27088(8)
R38	821.83057(1)	821.83144(42)	821.82925(32)	821.82925(32)	821.83028(33)	821.82982(34)	821.82931(34)	821.82973(30)	821.83(11)
R40	823.39117(1)	823.39081(44)	823.39057(35)	823.39058(35)	823.39066(37)	823.39033(38)	823.38971(41)	823.39076(30)	823.39055(12)
R42	824.95312(1)	824.95291(52)	824.95215(48)	824.95216(48)	824.95301(57)	824.95144(59)	824.95153(67)	824.95142(39)	824.95273(16)
R44	826.51662(1)	826.51625(72)	826.51404(54)	826.51405(54)	826.5149(65)	826.51434(72)	826.51406(91)	826.51539(46)	826.51633(20)

The uncertainties in parentheses are one standard deviation of the last digit quoted.

Table (3.7): Change of retrieved line intensities from HITRAN08 database.

Assignment	Technique #0	Technique #1	Technique #2	Technique #3	Technique #4	Technique #5	Technique #6	Technique #7
R4	4.360%	-43.14%	-43.14%	-44.31%	-43.52%	-43.52%	-34.36%	-2.095%
R6	4.004%	-32.76%	-32.76%	-32.11%	-33.13%	-34.94%	-17.20%	-4.359%
R8	1.324%	-31.00%	-31.00%	-32.03%	-31.52%	-32.17%	-19.94%	-1.127%
R10	-5.302%	-41.56%	-41.56%	-42.53%	-41.41%	-41.30%	-35.35%	-2.233%
R12	1.066%	-34.57%	-34.57%	-33.30%	-34.68%	-33.98%	-39.24%	2.498%
R14	3.895%	-32.84%	-32.84%	-32.82%	-32.08%	-32.22%	-37.28%	2.229%
R16	-0.9365%	-38.48%	-38.48%	-38.28%	-37.79%	-37.72%	-40.89%	-0.805%
R18	-0.7336%	-40.43%	-40.43%	-39.10%	-40.36%	-40.25%	-41.69%	-0.875%
R20	4.577%	-36.14%	-36.14%	-36.79%	-36.02%	-36.64%	-34.33%	-0.480%
R22	3.149%	-35.37%	-35.37%	-35.69%	-34.75%	-36.64%	-29.35%	1.622%
R24	-4.544%	-34.79%	-34.80%	-34.56%	-35.98%	-37.09%	-37.84%	-2.200%
R26	0.7637%	-41.01%	-41.07%	-37.85%	-37.71%	-35.86%	-39.88%	1.078%
R28	7.628%	-40.50%	-40.48%	-39.47%	-38.55%	-39.79%	-40.12%	0.703%
R30	-2.460%	-36.66%	-36.63%	-35.49%	-34.34%	-38.30%	-37.12%	1.697%
R32	-6.533%	-34.49%	-34.50%	-35.51%	-37.68%	-35.52%	-37.26%	-3.943%
R34	10.84%	-37.73%	-37.73%	-37.53%	-38.03%	-36.75%	-39.31%	2.698%
R36	13.83%	-30.15%	-30.15%	-31.32%	-27.32%	-33.09%	-22.09%	5.486%
R38	-7.499%	-37.75%	-37.75%	-38.52%	-39.34%	-41.01%	-21.00%	-1.357%
R40	-4.185%	-42.81%	-42.83%	-41.06%	-47.42%	-42.81%	-38.48%	-4.841%
R42	18.48%	-24.70%	-24.71%	-22.18%	-16.22%	-14.15%	-35.24%	14.03%
R44	3.737%	-16.44%	-16.42%	-16.54%	1.649%	0.943%	-37.33%	12.71%

The difference is calculated as $[(Intensity)_{fit} - (Intensity)_{HITRAN}]/(Intensity)_{HITRAN}$.

Table (3.8): Change of retrieved air-broadening coefficients from HITRAN08 database.

Assignment	Technique #0 (%)	Technique #1 (%)	Technique #2 (%)	Technique #3 (%)	Technique #4 (%)	Technique #5 (%)	Technique #6 (%)	Technique #7 (%)
R4	15.91	-1.284	-1.284	-2.367	-2.391	-3.486	11.81	1.107
R6	9.392	-14.7	-14.7	-11.23	-10.91	-8.688	-36.39	2.211
R8	1.975	-17.7	-17.7	-13.84	-14.54	-13.23	-30.95	-1.525
R10	-6.038	-7.615	-7.603	-4.077	-5.013	-6.41	-15.92	-1.833
R12	0.5249	-15.94	-15.94	-16.01	-15.33	-17.34	-6.496	-5.223
R14	3.775	-18.65	-18.65	-19.59	-19.73	-22.16	-11.16	-3.963
R16	3.896	-9.905	-9.891	-10.99	-11.34	-13.83	-6.812	-2.616
R18	5.90	-5.831	-5.845	-6.801	-5.97	-6.953	-5.055	-2.992
R20	11.16	-13.91	-13.91	-12.61	-12.88	-11.84	-15.83	-2.496
R22	5.966	-24.26	-24.26	-19.96	-21.19	-18.27	-27.43	-3.949
R24	-6.605	-15.17	-15.16	-13.45	-13.02	-10.33	-10.49	-0.1146
R26	-2.717	-5.289	-5.448	-8.497	-8.338	-12.17	-3.974	-3.613
R28	4.716	-5.808	-5.837	-7.70	-9.127	-10.23	-5.473	-2.926
R30	3.085	-6.769	-6.827	-10.09	-11.58	-9.167	-6.667	-4.854
R32	2.907	-3.862	-3.847	-3.818	-1.131	-5.771	-1.953	1.645
R34	23.22	-4.204	-4.204	-1.681	-1.888	-1.652	-2.021	-5.369
R36	15.37	-28.42	-28.43	-21.66	-25.47	-14.16	-30.83	-4.778
R38	-11.45	-7.641	-7.641	-0.6825	1.068	5.875	-29.26	0.6825
R40	-18.3	2.842	2.857	4.717	11.34	6.652	0.7143	3.571
R42	-8.373	-26.66	-26.66	-35.73	-42.13	-51.91	-6.731	-14.96
R44	-8.516	-23.97	-23.99	-33.21	-57.23	-79.58	1.784	-13.7
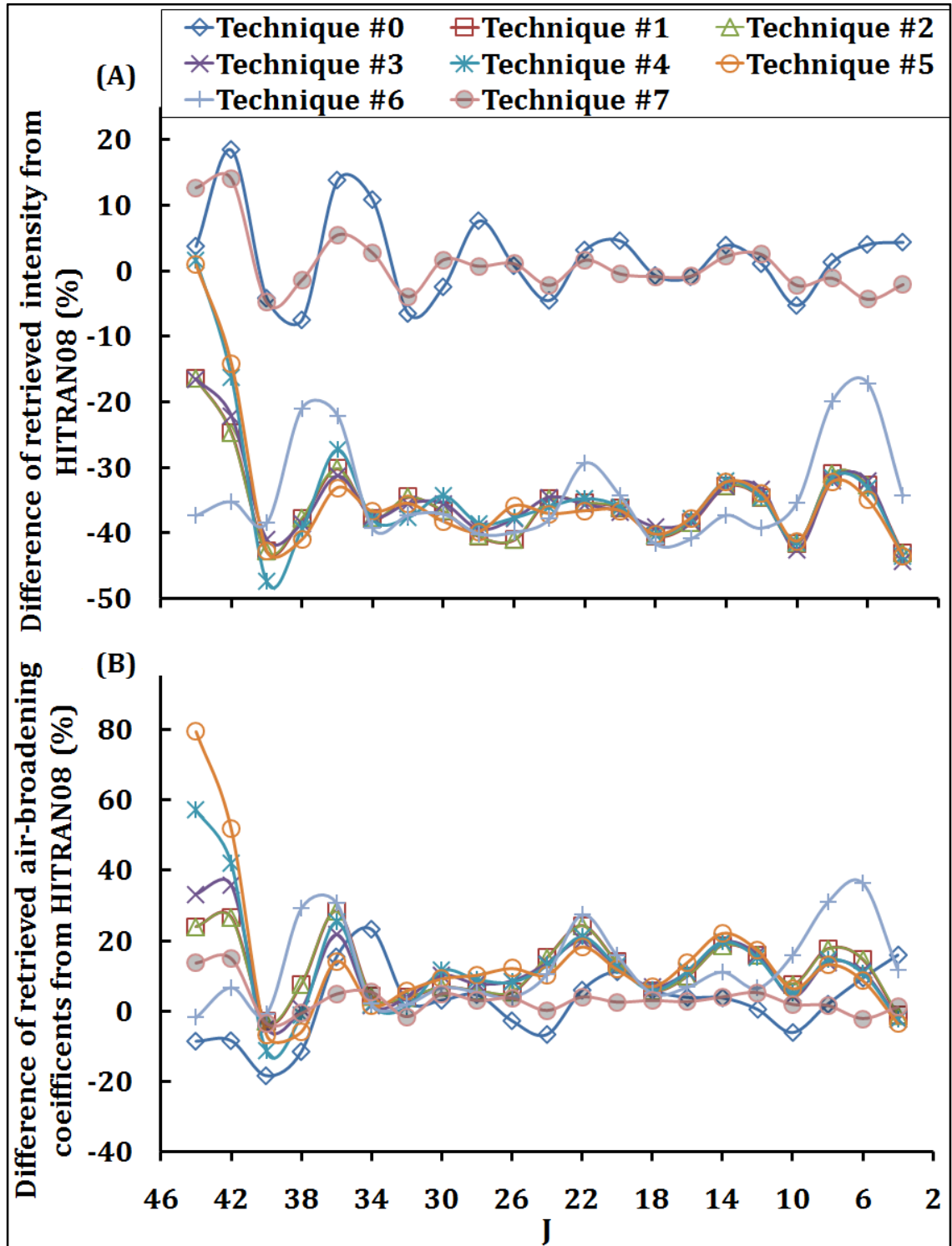
Figure (3.15): Difference between results retrieved using different channel handling techniques and HITRAN08 data listed spectral line rotational quantum number J for line A) intensity and B) air-broadening coefficient.

3.6: Concluding Remarks

In this chapter, different spectral channel handling techniques were introduced and discussed. Seven carbon dioxide spectra recorded at the CLS synchrotron facility were used to test seven different channel handling techniques. Six of these techniques used interferogram editing, and were tested using a LabVIEW program designed to calculate the SNR of the channel handled spectra. The results showed that using a synthetic background produced from the sample interferogram to simulate the channel spectra yielded a greater increase in SNR when compared to other interferogram editing techniques. However, testing the different handling techniques using a nonlinear least square multispectrum fitting program showed that technique #7 (channel spectra fitting) resulted in fitting quality significantly better and consistent throughout the spectral range [see Table (3.4) and Figures (3.13) and (3.14)]. The intensities retrieved from the fits when compared to HITRAN08 values showed that all interferogram editing techniques cause significant reduction in the retrieved line intensities. Technique #7 provides intensities different by 3.29% from the HITRAN08 values. Since the HITRAN08 database lists the uncertainty in line intensities for this band to be $\geq$ 2% and < 5%, these results that are in agreement with the HITRAN08 database [see table (3.5)]. Also, using spectra handled by technique #7 produced air-broadening results that differ by 4.01 % from HITRAN08 values, which are within the listed uncertainty in HITRAN08 ($\geq$ 2% and < 5%), as shown in table (3.5).

Since technique #7 (channel spectra fitting) using narrow spectral ranges produces better fits and line parameters, compared to HITRAN, than other

techniques, it is the recommended technique. However, the narrow spectral range requirement could be laborious when wide ranges need to be analyzed for a large number of spectra. For example, the CO_2 laser band I from 920 cm^{-1} to 993 cm^{-1} would be divided into 13 sections and, if the fit has 24 spectra, hence over 300 spectral files. The more serious effect of this limited range requirement arises from the inability to analyze the complete band and use constraints to model the band instead of individual line parameters, which is useful in retrieving parameters for weak bands [100]. Therefore, improvements for technique #7 to widen the spectral requirement while keeping its channel reduction and accurate retrieval of spectral parameters would be valuable.

"Every day you may make progress. Every step may be fruitful. Yet there will stretch out before you an ever-lengthening, ever-ascending, ever-improving path. You know you will never get to the end of the journey. But this, so far from discouraging, only adds to the joy and glory of the climb."[101]

Sir Winston Churchill / UK prime minister during WWII
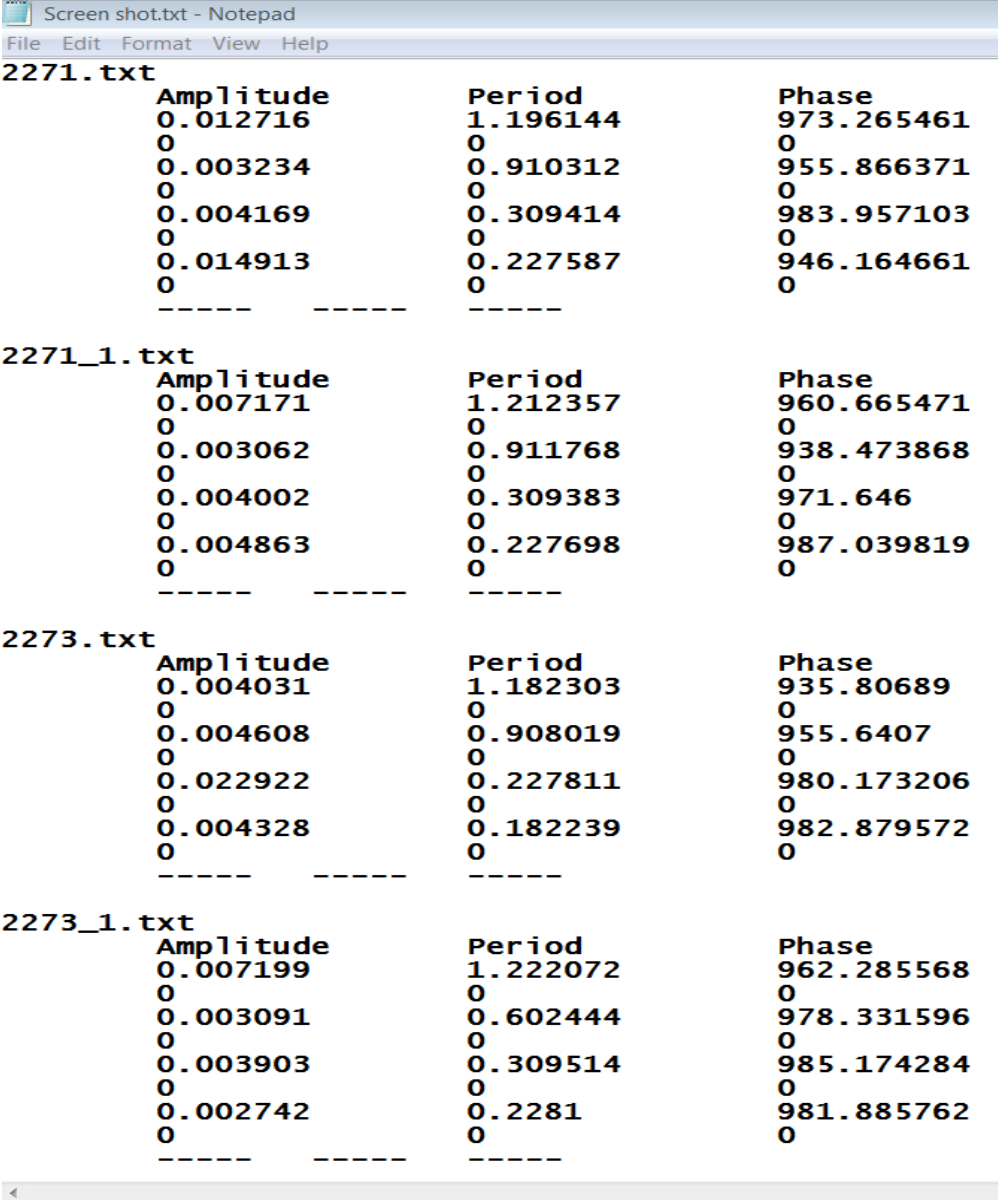
Chapter 4: Line Shape Study of Carbon Dioxide Laser band I

4.1: Improving Channel Spectra Fitting Technique

From the analysis in the previous chapter, it appears that the main drawback of the channel fitting technique is the need to apply it for a narrow spectral range. This requirement stems from the difficulty in simulating channel spectra over wide spectral ranges. Since channel spectra are the result of the summation of different sinusoidal waves (channels) in the background spectra, it should be possible to simulate it by using a larger number of channels in the spectral fit. This simulation of the complicated channel spectra patterns can be achieved by applying an iterative process of fitting channel spectra, measuring new channel spectra in the residual fit and then including the new channel spectra in the fit, and so on. The aim of this procedure is to produce satisfactory simulation of the channel spectra and remove them from the entire spectral range.

Unfortunately, the non-linear least square fitting algorithm developed by Benner et al. [96] and used in this study cannot be integrated into our LabVIEW code. Therefore, the LabIVEW code was modified to produce an output file that can be used in the input of the fitting algorithm, instead of entering channel parameters individually. Since a spectral fit with tens of spectra could require over a hundred

channels, each defined by three parameters (amplitude, period and phase), it could

be a very time-consuming task with iterations. Figure (4.1) shows an example of the

LabVIEW program output file. The LabVIEW program is also able to read all spectral

residuals files in a folder at once.

Figure (4.1): Screen shot of channel spectra analysis program[30].

---

[30] Channel phase is expressed as the location of the first minimum as used by spectral fitting program

4.2: Fitting Carbon Dioxide Laser band I

The carbon dioxide laser band I (00011 ← 10001) centred at 10.4 μm (961 cm^{-1}) is one of the two hot bands (the other one is centered at 9.4 μm) that share the ν_3 vibrational state as their upper transition state and have Fermi resonance states $2\nu_2$ and ν_1 as their lower transition state [102]. They are commonly known as laser bands because they form the basis of CO_2 laser operation. In limb sounding satellite measurements, where the decreasing tangent angle results in stronger emitted radiance, laser band I is present in recorded spectra [103]. For these reasons, many spectroscopic studies of laser bands [102, 104-107] have been undertaken to obtain accurate knowledge of spectral line parameters. In one of these studies, Dana et al. [105] were faced with channel spectra problems and they introduced an analysis of the channels that assumes that channel spectra result only from optical reflection at the beam splitter. However, in my work, the spectra were recorded with a synchrotron source that has a more complicated optical pipeline [see figure (2.6)] and it is difficult to make the same assumption.

Because laser bands are relatively well studied, we decided to use them to test our channel handling technique of choice (channel spectra fitting) to determine if it can be used to fit a complete band. Twenty four spectra were used in this fit, 11 pure CO_2 and 13 carbon dioxide mixed with air at a mixing ratio of 5%. All spectra were recorded using the Bruker optics IFS125HR spectrometer with 8 spectra recorded using the globar source and 16 using the synchrotron source. All samples were measured in a temperature-stabilized 2-m Herriott cell with a 72.15 m optical

path length. The remaining experimental details are the same as mentioned in section (2.5).

Table (4.1): Experimental conditions of the spectra used laser band fit.

No.	Sample	Source	Pressure (Torr)	Temperature (°C)	Pathlength (m)	Resolution (cm^{-1})
1	CO_2	GB	0.26	23.44	72.15m	0.0015
2	CO_2	GB	16.34	23.58	72.15m	0.0015
3	CO_2	GB	29.99	23.60	72.15m	0.0020
4	CO_2	SR	39.89	23.35	72.15m	0.0030
5	CO_2	GB	50.44	23.51	72.15m	0.0040
6	CO_2	SR	65.12	23.35	72.15m	0.0030
7	CO_2	GB	75.74	23.58	72.15m	0.0040
8	CO_2	GB	85.01	23.70	72.15m	0.0030
9	CO_2	GB	94.80	23.71	72.15m	0.0040
10	CO_2	SR	99.07	20.85	72.15m	0.0030
11	CO_2	GB	149.00	23.95	72.15m	0.0015
12	CO_2+Air	SR	40.07	23.65	72.15m	0.0030
13	CO_2+Air	SR	60.00	23.44	72.15m	0.0030
14	CO_2+Air	SR	70.00	23.42	72.15m	0.0030
15	CO_2+Air	SR	80.23	23.13	72.15m	0.0030
16	CO_2+Air	SR	90.01	23.33	72.15m	0.0030
17	CO_2+Air	SR	99.20	23.70	72.15m	0.0030
18	CO_2+Air	SR	201.09	23.31	72.15m	0.0040
19	CO_2+Air	SR	300.12	23.21	72.15m	0.0040
20	CO_2+Air	SR	450.42	23.55	72.15m	0.0040
21	CO_2+Air	SR	525.00	23.82	72.15m	0.0040
22	CO_2+Air	SR	600.46	23.56	72.15m	0.0040
23	CO_2+Air	SR	750	23.63	72.15m	0.0040
24	CO_2+Air	SR	825.01	23.88	72.15m	0.0040

SR stands for synchrotron source and GB stands for globar source.

Line parameters for the laser band I of pure carbon dioxide and carbon dioxide mixed with air published in the HITRAN08 database were used as "initial estimates" in the modelling of spectra and the channel spectra were calculated using the LabVIEW program given in Appendix A. The channels were added one or two at a time, from lower to higher pressure spectra, in order to obtain accurate line positions. After all spectra with channelling were fitted, a second round of channels

was added by using the new residuals keeping the parameters of the first set of channels fixed. After fitting the second iteration channels, the first iteration channels were floated again and fitted. In order to avoid divergence of the solution, the channels were floated on two steps, first the amplitude, then the period and phase. After fitting iteration, the residual and standard deviation (STDV) of the spectra were inspected and, in case one of the channels changed drastically from the initial value, causing a larger STDV of the spectrum, they were replaced and re-fitted separately. All synchrotron spectra needed spectral channels to be fitted and only four out of the eight globar ones needed to have spectral channels added. Eventually, 142 spectral channels were added to the fit to get a channel-free residual of the fit. Figure (4.2) shows a screen shot of the channel fitting program. The details of formulas used in retrieving spectral parameters are given in [106, 107].

```
labfitqw - [Dialogue Window]
    File   Edit   View   State   Window   Help
Option:   x

Fit      8515
There are currently      370 spectral lines
There are currently   24 spectra
There are currently no constraints
Type:

   I    to reset number of iterations                   25
   P    for exponential pressure shift temperature model
   D    to map residuals
   A    to add a spectrum
   E    to edit spectrum parameters
   B    to list spectrum numbers currently in the solution
   +    to add a spectral line
   S    to edit default spectral line parameters
   C    to change the background polynomial order
   J    to edit full line mixing
   H    to edit absorption cutoff for wings of lines
   Y    to use Lorentz TDL line shape
   L    to modify spectral line lists
   -    to delete a spectral line
  nn    to edit spectral line nn
   &    to edit auxillary parameters
   @    to edit constraints
   *    to write reinput file and exit
   X    to begin the solution

Option:   x
There are        24 spectra in the solution
There are       370 spectral lines in the solution
There are       554 unconstrained parameters.
There are an additional       0 parameters constrained to unconstrained parameters
                  Background      52 Ch Ampltd       142
Channel            Period          0    Phase          0
                  Zero Level       0 Eff Apodz         0
        TDL Time Constant          0 FTS Phase        24
                   Position       48 Intensity        48
Lorentz Halfwidth     Foreign      48     Self         48
T Dep Lor Hwidth      Foreign       0     Self          0
Pressure Shift        Foreign      48     Self         48
T Dep Pressure Shift Foreign        0     Self          0
            Molecular Mass          0     E"            0
                     Dicke          0 Rosnkranz        48
Mix Foreign Real     at 296K        0 T expnent         0
Mix Self     Real    at 296K        0 T expnent         0
                     Speed          0 Auxiliary         0
Derivatives of run     2026
```

Figure (4.2): Screen shot of the multispectrum fitting program used in fitting channel spectra.

4.3: Data Analysis

Data analysis was preformed by simultaneously fitting 24 spectra [table (4.1)]. The individual line intensities, S_i, were retrieved by fitting the relation [28]:

$$S_i = \frac{v_i}{v_0} \frac{S_V}{Q_r} L_i \exp\left(\frac{-C_2 E_i''}{T}\right)\left[1 - exp\left(\frac{-C_2 v_i}{T}\right)\right] \times F \qquad (4.1)$$

where v_i is the centre position of the ith spectral line in cm^{-1}, v_0 is band origin in, S_V is the vibrational band intensity, Q_r is the lower state rotational partition function at temperature T, L_i is the Hönl-London factor, E_i'' is the lower state rotational energy, C_2 is the second radiation constant $= hc/k$; h is Planck's constant, c is the speed of light , k is the Boltzmann constant and F is a factor accounting for non-rigid behaviour. Since the CO_2 laser band I is a Σ to Σ band, there is no Q-branch and the Hönl-London factor, L_i is given by [108]:

$$L_i = \frac{m^2 - l''^2}{|m|} \qquad (4.2)$$

where m is quantum number index, $m = J'' + 1$ for the R-branch, and $m = -J''$ for P-branch, J'' is the lower state rotational quantum number and l'' is lower state vibrational angular momentum quantum number.

The F factor describes the deviation of line intensities from the rigid-rotor model due to Coriolis and/or Fermi couplings and centrifugal distortion [see section (1.3)]. Toth [109] derived the F-factor expression for the CO_2 parallel band, as Σ to Σ type ($\Delta l = 0$, no contribution from vibration angular momentum) [107], as :

$$F = [1 + A_1 m + A_2 m^2 + A_3 m_3]^2 \text{ for P and R branches} \qquad (4.3)$$

Each line in the band was fitted assuming either Voigt or (speed dependent voigt) SPD line shape convolved with the FTS instrumental line shape appropriate to the Bruker IFS125HR FTS. In the least-square solution, the Doppler broadening of the spectra was fixed to a value calculated by equation (1.25), rewritten here for convenience:

$$\Delta\tilde{\nu}_D = 7.2\text{x}10^{-7}\tilde{\nu}_0\sqrt{\frac{T}{M}} \tag{4.4}$$

where, $\tilde{\nu}_0$ is the position of the line centre in wavenumber, T is the gas temperature in K and M is the molecular weight in atomic mass units for the gas. The nonlinear least square fitting program [96] used the following expressions to determine the shift and broadening coefficients [110, 111]:

$$\tilde{\nu} = \tilde{\nu}_0 + p \times [\delta^0(\text{air})(1-\chi) + \delta^0(\text{self}) \times \chi] \tag{4.5}$$

$$b_L(p,T) = p \times \left[b_L^0(\text{air})(p_0,T_0) \times (1-\chi) \times \left(\frac{T_0}{T}\right)^{n_a} \right. \tag{4.6}$$
$$\left. + b_L^0(\text{self})(p_0,T_0) \times \chi \times \left(\frac{T_0}{T}\right)^{n_s} \right]$$

where $\tilde{\nu}$ and $\tilde{\nu}_0$ are the line positions at p and zero pressures, respectively,

$\delta^0(\text{air})$ and $\delta^0(\text{self})$ are air and self pressure line shifts coefficients, respectively,

χ is the ratio of partial pressure of CO_2 to the total sample pressure,

$b_L(p,T)$ is the Lorentz half-width at pressure p and temp. T,

$b_L^0(p_0,T_0)$ is the Lorentz half-width at reference pressure p_0 and temp. T_0,

n_a and n_s are the temperature dependence exponents of air- and self-broadened half-width, which are listed in the HITRAN database [106].

A more detailed description on retrieving spectral parameters from the spectra can be found in references [110, 111].

4.4: Fitting Results

A segment of the fitted spectra listed in table (4.1) and their residuals in the cases of channels not fitted and fitted is shown in figure (4.3). The residual in the case of handling (fitting) channels have no visible channel structure. The fit standard deviation was reduced from 1.72% to 0.569% as result of including channel handling in the fit.
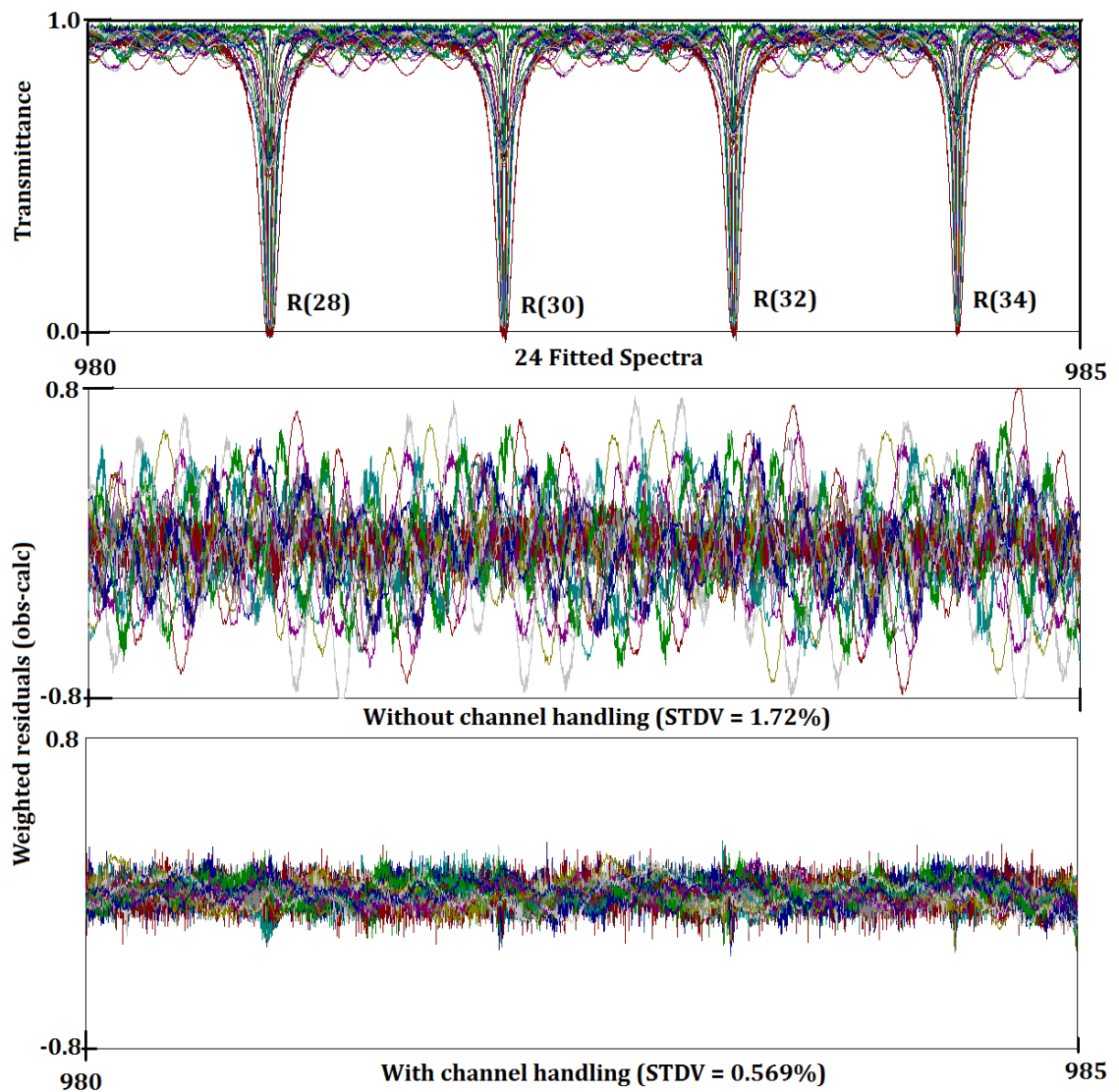
Figure (4.3): Segment of CO_2 laser band I with residual of the fit with and without channel handling.

The average percentage difference between retrieved line parameters using Voigt and speed-dependent (SPD) profiles, and HITRAN08 values are listed in table (4.2), while individual line parameters are listed in table (4.3). The retrieved parameters using channel handling techniques are in agreement with the HITRAN database. HITRAN 2008 lists an uncertainty in intensity of $\geq$ 2% and < 5% and an uncertainty in air- and self-broadening coefficients as $\geq$ 5% and < 10%. Therefore, parameters retrieved using channel handling, are in agreement with HITRAN.

The best improvement in parameter accuracy to HITRAN was the air-broadening. Retrieved air-broadening coefficients also have the best accuracy to HITRAN compared with retrieved intensity and self-broadening with the latter being the worst in accuracy. The reason for this accuracy difference is that air-broadening coefficients were retrieved using 13 air-broadened synchrotron spectra which have much higher SNR than the 8 self-broadened globar spectra used in retrieving self-broadening coefficients. This SNR difference between synchrotron and globar spectra is noticeable in their fitting residuals shown in figure (4.4).

Table (4.2): CO_2 laser retrieved parameters deviation from HITRAN08.

Parameter ⟍ Profile	Average deviation* from HITRAN08 values			
	Voigt with channel handling%	SPD with channel handling%	Voigt without channel handling %	SPD without channel handling %
Intensity	2.11	2.28	2.41	3.01
Air-broadening	1.25	2.70	4.69	7.46
Self-broadening	4.14	3.68	4.66	5.05

$$\textbf{*Average deviation} = \sum\nolimits_{\textbf{all lines}} \left\| \frac{[(\textbf{Retrieved value}) - (\textbf{HITRAN})]}{(\textbf{HITRAN})} \textbf{x100} \right\|$$

Table (4.3): CO_2 laser band I retrieved: (A) intensity.

Assignment	HITRAN08 × 10^{-24}	Voigt × 10^{-24}	SPD × 10^{-24}	No channel handling Voigt × 10^{-24}	No channel handling SPD × 10^{-24}	Voigt diff.	SPD diff.	No channel handling Voigt diff.	No channel handling SPD diff.
P 44e	2.33(5)	2.31(0)	2.33(0)	2.26(1)	2.28(1)	-0.939%	-0.0729%	-3.10%	-2.28%
P 42e	3.11(6)	3.10(0)	3.11(1)	3.10(1)	3.10(2)	-0.351%	0.106%	-0.0901%	-0.0966%
P 40e	4.06(8)	4.08(1)	4.10(1)	4.16(2)	4.30(2)	0.374%	0.940%	2.49%	5.91%
P 38e	5.22(10)	5.31(1)	5.37(1)	5.17(2)	5.28(3)	1.74%	2.84%	-0.853%	1.10%
P 36e	6.58(13)	6.70(1)	6.74(2)	6.82(3)	6.81(4)	1.80%	2.40%	3.58%	3.44%
P 34e	8.16(16)	8.33(1)	8.31(2)	8.44(4)	8.47(5)	2.16%	1.84%	3.45%	3.91%
P 32e	9.91(20)	9.96(1)	9.88(2)	9.66(4)	9.56(4)	0.467%	-0.348%	-2.54%	-3.59%
P 30e	11.82(24)	12.00(1)	11.94(2)	12.46(4)	12.43(5)	1.53%	0.990%	5.43%	5.12%
P 28e	13.82(28)	13.92(1)	13.87(2)	13.65(4)	13.65(5)	0.702%	0.376%	-1.26%	-1.25%
P 26e	15.83(32)	15.80(2)	15.72(2)	16.18(4)	16.19(5)	-0.202%	-0.701%	2.19%	2.27%
P 24e	17.75(36)	17.94(2)	17.89(2)	17.97(4)	17.98(5)	1.07%	0.811%	1.22%	1.30%
P 22e	19.46(39)	19.68(2)	19.64(2)	19.94(5)	19.90(5)	1.14%	0.930%	2.48%	2.28%
P 20e	20.84(42)	21.08(2)	21.05(2)	21.17(5)	21.18(6)	1.17%	0.984%	1.57%	1.65%
P 18e	21.76(44)	22.02(2)	21.98(2)	22.36(5)	22.42(6)	1.19%	1.03%	2.77%	3.01%
P 16e	22.09(44)	22.29(2)	22.25(2)	22.26(5)	22.27(6)	0.901%	0.711%	0.765%	0.819%
P 14e	21.74(43)	22.25(2)	22.24(2)	22.43(5)	22.40(5)	2.35%	2.29%	3.16%	3.02%
P 12e	20.64(41)	20.77(2)	20.70(2)	20.66(5)	20.65(6)	0.625%	0.276%	0.116%	0.0436%
P 10e	18.76(38)	19.21(2)	19.19(2)	19.29(5)	19.27(6)	2.41%	2.28%	2.82%	2.70%
P 8e	16.12(32)	16.22(2)	16.15(2)	16.18(4)	16.10(5)	0.633%	0.211%	0.391%	-0.118%
P 6e	12.79(26)	12.77(1)	12.67(2)	12.90(4)	12.86(5)	-0.172%	-0.946%	0.868%	0.547%
P 4e	8.88(18)	9.08(1)	9.06(1)	9.34(4)	9.45(5)	2.16%	1.94%	5.14%	6.32%
P 2e	4.56(9)	4.56(0)	4.57(1)	4.61(1)	4.61(2)	0.154%	0.331%	1.22%	1.21%
R 0e	2.30(5)	2.28(0)	2.28(0)	2.32(1)	2.32(1)	-0.792%	-0.648%	0.940%	0.970%
R 2e	6.81(14)	6.86(1)	6.88(1)	7.02(3)	7.10(4)	0.728%	1.04%	3.05%	4.27%
R 4e	11.03(22)	11.44(1)	11.51(2)	11.36(4)	11.37(5)	3.69%	4.32%	3.00%	3.07%
R 6e	14.78(30)	15.29(2)	15.31(2)	15.29(4)	15.34(6)	3.45%	3.58%	3.46%	3.80%
R 8e	17.91(36)	18.36(2)	18.33(2)	18.14(5)	18.00(5)	2.52%	2.36%	1.26%	0.503%
R 10e	20.32(41)	20.58(2)	20.56(2)	20.58(5)	20.54(5)	1.27%	1.17%	1.28%	1.10%
R 12e	21.95(44)	22.58(2)	22.74(2)	23.05(5)	23.36(6)	2.85%	3.60%	5.02%	6.40%
R 14e	22.80(46)	23.32(2)	23.37(2)	23.62(5)	23.75(6)	2.28%	2.49%	3.58%	4.18%
R 16e	22.90(46)	23.50(2)	23.47(2)	23.70(5)	23.83(6)	2.61%	2.48%	3.49%	4.04%
R 18e	22.34(45)	23.01(2)	22.97(2)	22.80(5)	22.79(6)	2.99%	2.82%	2.06%	2.03%
R 20e	21.22(42)	22.27(2)	22.42(2)	21.90(5)	21.99(6)	4.97%	5.65%	3.21%	3.61%
R 22e	19.67(39)	20.32(2)	20.28(2)	19.87(5)	19.80(5)	3.32%	3.10%	1.03%	0.641%
R 24e	17.82(36)	18.48(2)	18.45(2)	17.91(4)	17.85(5)	3.68%	3.52%	0.499%	0.185%
R 26e	15.80(32)	16.65(2)	16.80(2)	16.24(4)	16.42(5)	5.40%	6.34%	2.78%	3.90%
R 28e	13.71(27)	14.12(1)	14.04(2)	13.50(4)	13.27(5)	2.99%	2.37%	-1.56%	-3.19%
R 30e	11.67(23)	12.26(1)	12.34(2)	11.63(4)	11.58(4)	5.04%	5.72%	-0.360%	-0.763%
R 32e	9.73(19)	10.19(1)	10.24(2)	9.72(4)	9.65(4)	4.63%	5.17%	-0.157%	-0.872%
R 34e	7.97(16)	8.30(1)	8.31(2)	7.91(3)	7.79(4)	4.12%	4.28%	-0.774%	-2.19%
R 36e	6.40(13)	6.63(1)	6.61(1)	6.42(3)	6.27(4)	3.50%	3.23%	0.256%	-2.14%
R 38e	5.05(10)	5.27(1)	5.31(1)	5.34(3)	5.34(3)	4.34%	5.17%	5.81%	5.69%
R 40e	3.91(8)	4.03(1)	4.05(1)	4.20(2)	4.41(3)	2.93%	3.51%	7.45%	12.7%
R 42e	2.98(6)	3.08(0)	3.12(1)	3.14(1)	3.18(2)	3.34%	4.78%	5.38%	6.89%
R 44e	2.23(4)	2.27(0)	2.30(0)	2.31(1)	2.38(1)	1.97%	3.19%	3.77%	7.03%
R 46e	1.64(3)	1.66(0)	1.68(0)	1.72(1)	1.78(1)	1.16%	2.31%	5.14%	8.64%
R 48e	1.18(2)	1.19(0)	1.20(0)	1.20(1)	1.21(1)	0.498%	1.41%	1.17%	2.01%
R 50e	0.84(2)	0.83(0)	0.83(0)	0.83(0)	0.83(1)	-1.86%	-1.62%	-1.49%	-1.50%

*Intensity cm^{-1}/(molecule × cm^{-2}) at 296 K (in natural abundance)

**The uncertainities listed in parentheses are one standard deviation in units of the last quoted digit

Table (4.3): CO₂ laser band I retrieved: (B) Air-broadening coefficient.

Assignment	Air broadening Coefficient (cm⁻¹ atm⁻¹ at 296 K)					Voigt diff.	SPD diff.	No channel handling Voigt diff.	No channel handling SPD diff.
	HITRAN08	Voigt	SPD	No channel handling Voigt	No channel handling SPD				
P 44e	0.0668(33)	0.0674(4)	0.0710(5)	0.0627(11)	0.0659(14)	0.838%	6.29%	-6.18%	-1.38%
P 42e	0.0671(34)	0.0660(3)	0.0675(5)	0.0650(9)	0.0651(12)	-1.59%	0.611%	-3.19%	-3.03%
P 40e	0.0673(34)	0.0666(3)	0.0684(4)	0.0668(7)	0.0758(13)	-0.996%	1.56%	-0.698%	12.6%
P 38e	0.0675(34)	0.0674(2)	0.0702(5)	0.0646(6)	0.0694(12)	-0.119%	4.04%	-4.28%	2.81%
P 36e	0.0677(34)	0.0694(2)	0.0709(4)	0.0683(6)	0.0680(9)	2.51%	4.70%	0.842%	0.428%
P 34e	0.0679(34)	0.0691(2)	0.0684(3)	0.0698(5)	0.0711(11)	1.80%	0.766%	2.86%	4.64%
P 32e	0.0682(34)	0.0675(2)	0.0655(3)	0.0659(4)	0.0632(8)	-1.07%	-3.97%	-3.39%	-7.30%
P 30e	0.0686(34)	0.0689(1)	0.0674(2)	0.0715(4)	0.0705(7)	0.423%	-1.69%	4.18%	2.74%
P 28e	0.0690(35)	0.0691(1)	0.0682(2)	0.0671(4)	0.0670(6)	0.188%	-1.16%	-2.72%	-2.84%
P 26e	0.0695(35)	0.0684(1)	0.0669(2)	0.0715(3)	0.0716(7)	-1.65%	-3.78%	2.94%	3.01%
P 24e	0.0701(35)	0.0699(1)	0.0691(2)	0.0709(3)	0.0710(6)	-0.257%	-1.47%	1.08%	1.26%
P 22e	0.0708(35)	0.0706(1)	0.0699(2)	0.0721(3)	0.0713(5)	-0.240%	-1.26%	1.84%	0.749%
P 20e	0.0717(36)	0.0713(1)	0.0706(2)	0.0724(3)	0.0724(5)	-0.558%	-1.56%	0.907%	1.00%
P 18e	0.0728(36)	0.0724(1)	0.0718(2)	0.0750(3)	0.0760(6)	-0.549%	-1.35%	3.01%	4.38%
P 16e	0.0740(37)	0.0736(1)	0.0728(1)	0.0734(3)	0.0734(5)	-0.541%	-1.58%	-0.851%	-0.757%
P 14e	0.0754(38)	0.0760(1)	0.0757(1)	0.0762(3)	0.0756(4)	0.809%	0.358%	1.05%	0.225%
P 12e	0.0771(39)	0.0763(1)	0.0750(2)	0.0767(3)	0.0762(6)	-1.05%	-2.74%	-0.545%	-1.12%
P 10e	0.0790(40)	0.0796(1)	0.0791(2)	0.0796(3)	0.0791(7)	0.785%	0.152%	0.810%	0.0886%
P 8e	0.0811(41)	0.0805(1)	0.0791(2)	0.0792(4)	0.0775(7)	-0.715%	-2.52%	-2.32%	-4.50%
P 6e	0.0836(42)	0.0815(2)	0.0791(3)	0.0834(5)	0.0824(8)	-2.56%	-5.37%	-0.263%	-1.48%
P 4e	0.0863(43)	0.0868(2)	0.0861(3)	0.0928(7)	0.0961(14)	0.614%	-0.197%	7.52%	11.3%
P 2e	0.0893(45)	0.0901(3)	0.0908(5)	0.0947(10)	0.0946(13)	0.885%	1.65%	5.99%	5.95%
R 0e	0.0949(47)	0.0950(7)	0.0958(8)	0.1000(20)	0.0995(22)	0.126%	0.991%	5.37%	4.88%
R 2e	0.0877(44)	0.0871(2)	0.0880(4)	0.0912(7)	0.0951(14)	-0.673%	0.388%	4.03%	8.40%
R 4e	0.0849(42)	0.0855(2)	0.0873(4)	0.0833(5)	0.0834(8)	0.742%	2.83%	-1.88%	-1.79%
R 6e	0.0823(41)	0.0831(1)	0.0834(3)	0.0856(4)	0.0867(9)	0.984%	1.28%	4.01%	5.29%
R 8e	0.0800(40)	0.0795(1)	0.0788(2)	0.0775(3)	0.0750(6)	-0.637%	-1.51%	-3.14%	-6.23%
R 10e	0.0780(39)	0.0772(1)	0.0768(2)	0.0768(3)	0.0762(5)	-1.00%	-1.59%	-1.50%	-2.29%
R 12e	0.0762(38)	0.0776(1)	0.0801(2)	0.0799(3)	0.0849(6)	1.80%	5.14%	4.86%	11.4%
R 14e	0.0747(37)	0.0748(1)	0.0755(2)	0.0768(3)	0.0791(6)	0.0937%	1.11%	2.82%	5.88%
R 16e	0.0734(37)	0.0740(1)	0.0737(1)	0.0759(3)	0.0781(6)	0.804%	0.354%	3.39%	6.36%
R 18e	0.0722(36)	0.0728(1)	0.0724(1)	0.0726(3)	0.0727(5)	0.803%	0.291%	0.609%	0.734%
R 20e	0.0713(36)	0.0723(1)	0.0747(2)	0.0704(3)	0.0723(6)	1.43%	4.78%	-1.32%	1.37%
R 22e	0.0704(35)	0.0706(1)	0.0701(2)	0.0695(3)	0.0684(5)	0.241%	-0.412%	-1.31%	-2.81%
R 24e	0.0698(35)	0.0705(1)	0.0703(2)	0.0680(3)	0.0673(5)	1.00%	0.731%	-2.55%	-3.65%
R 26e	0.0692(35)	0.0712(1)	0.0743(2)	0.0706(3)	0.0741(7)	2.90%	7.43%	2.02%	7.01%
R 28e	0.0687(34)	0.0682(1)	0.0667(2)	0.0638(3)	0.0597(6)	-0.742%	-2.95%	-7.07%	-13.1%
R 30e	0.0684(34)	0.0698(1)	0.0719(3)	0.0653(4)	0.0642(6)	2.11%	5.12%	-4.47%	-6.11%
R 32e	0.0681(34)	0.0689(2)	0.0703(3)	0.0647(4)	0.0630(8)	1.12%	3.23%	-5.04%	-7.47%
R 34e	0.0678(34)	0.0680(2)	0.0684(3)	0.0632(5)	0.0601(7)	0.236%	0.885%	-6.84%	-11.3%
R 36e	0.0676(34)	0.0682(2)	0.0678(3)	0.0640(6)	0.0592(8)	0.932%	0.266%	-5.34%	-12.4%
R 38e	0.0674(34)	0.0671(2)	0.0690(5)	0.0684(7)	0.0684(11)	-0.519%	2.43%	1.42%	1.41%
R 40e	0.0672(34)	0.0674(3)	0.0689(5)	0.0709(8)	0.0824(16)	0.223%	2.50%	5.55%	22.6%
R 42e	0.0670(34)	0.0644(3)	0.0691(5)	0.0657(9)	0.0700(13)	-3.90%	3.19%	-1.88%	4.42%
R 44e	0.0667(33)	0.0645(4)	0.0690(5)	0.0633(10)	0.0748(15)	-3.31%	3.51%	-5.11%	12.1%
R 46e	0.0664(33)	0.0718(6)	0.0769(7)	0.0940(20)	0.1187(30)	8.16%	15.8%	41.5%	78.8%
R 48e	0.0661(33)	0.0691(7)	0.0728(9)	0.0850(26)	0.0900(33)	4.49%	10.1%	28.6%	36.2%
R 50e	0.0658(33)	0.0659(10)	0.0672(11)	0.0763(33)	0.0726(32)	0.122%	2.19%	15.9%	10.3%
The uncertainities listed in parentheses are one deviation in units of the last quoted digit									

Table (4.3): CO₂ laser band I retrieved: (C) Self-broadening coefficient.

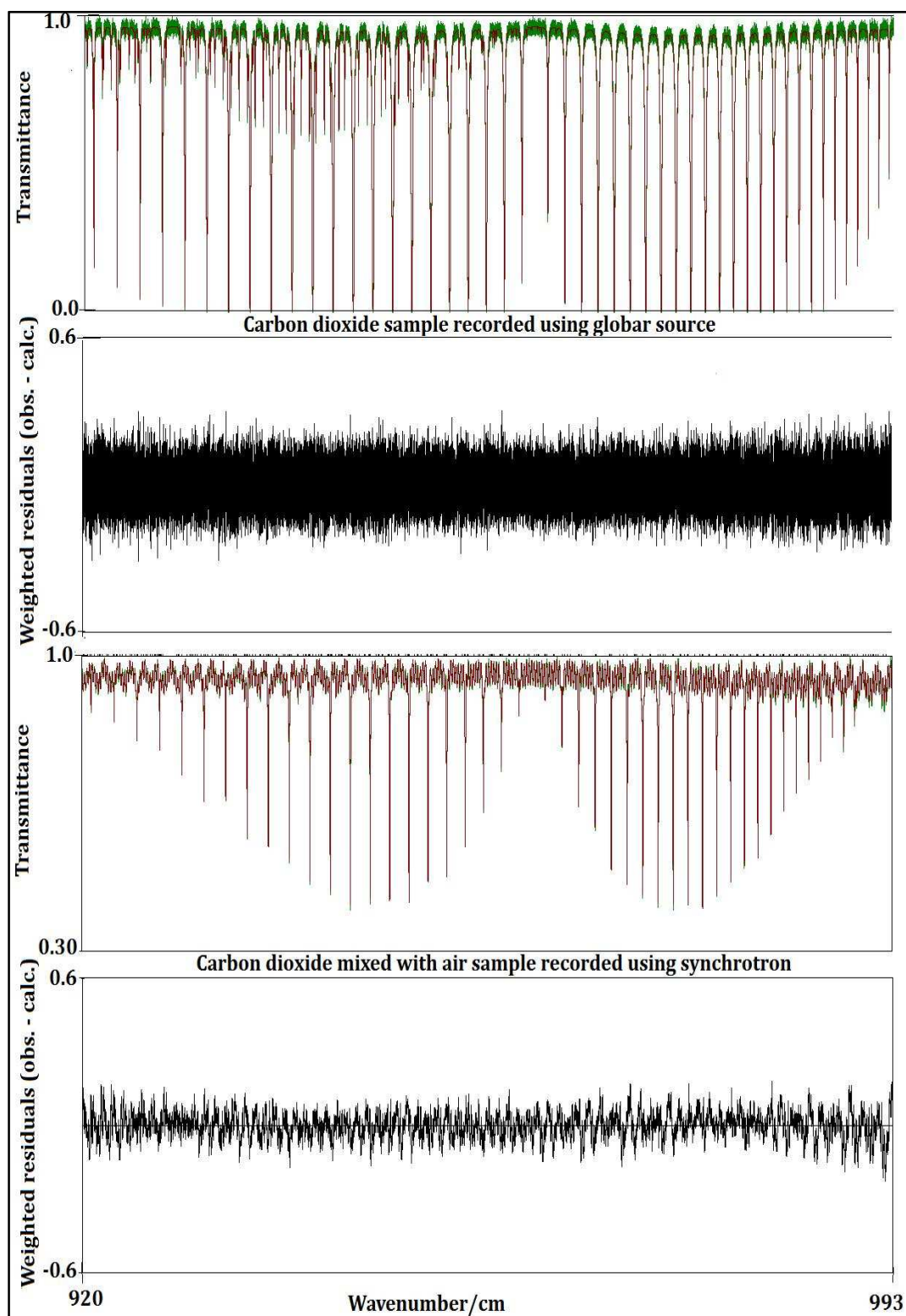| Assignment	Self broadening Coefficient ($cm^{-1} atm^{-1}$)					Voigt diff.	SPD diff.	No channel handling Voigt	No channel handling SPD Diff.
	HITRAN08	Voigt	SPD	No channel handling Voigt	No channel handling SPD				
P 44e	0.0760(38)	0.0716(2)	0.0738(3)	0.0708(5)	0.0729(7)	-5.78%	-2.84%	-6.80%	-4.11%
P 42e	0.0780(39)	0.0719(2)	0.0725(2)	0.0684(5)	0.0684(6)	-7.83%	-7.03%	-12.3%	-12.3%
P 40e	0.0800(40)	0.0745(2)	0.0750(2)	0.0746(5)	0.0758(6)	-6.84%	-6.25%	-6.80%	-5.24%
P 38e	0.0810(41)	0.0759(2)	0.0762(2)	0.0806(6)	0.0810(6)	-6.36%	-5.98%	-0.543%	0.0370%
P 36e	0.0830(42)	0.0776(2)	0.0777(2)	0.0734(5)	0.0734(5)	-6.46%	-6.41%	-11.6%	-11.5%
P 34e	0.0840(42)	0.0805(2)	0.0807(2)	0.0808(5)	0.0809(5)	-4.14%	-3.95%	-3.77%	-3.75%
P 32e	0.0860(43)	0.0849(2)	0.0851(2)	0.0890(5)	0.0891(5)	-1.28%	-1.08%	3.50%	3.59%
P 30e	0.0880(44)	0.0857(2)	0.0858(2)	0.0799(4)	0.0799(4)	-2.66%	-2.56%	-9.26%	-9.24%
P 28e	0.0900(45)	0.0883(1)	0.0884(1)	0.0928(4)	0.0927(4)	-1.89%	-1.80%	3.06%	3.03%
P 26e	0.0920(46)	0.0924(1)	0.0924(1)	0.0878(4)	0.0876(4)	0.380%	0.478%	-4.60%	-4.82%
P 24e	0.0930(47)	0.0929(1)	0.0929(1)	0.0940(4)	0.0939(4)	-0.140%	-0.108%	1.05%	0.978%
P 22e	0.0960(48)	0.0947(1)	0.0947(1)	0.0914(3)	0.0915(3)	-1.41%	-1.40%	-4.75%	-4.74%
P 20e	0.0980(49)	0.0968(1)	0.0968(1)	0.0972(3)	0.0971(3)	-1.23%	-1.22%	-0.847%	-0.908%
P 18e	0.1000(50)	0.0977(1)	0.0977(1)	0.0940(3)	0.0938(3)	-2.32%	-2.31%	-6.05%	-6.20%
P 16e	0.1020(51)	0.0999(1)	0.0999(1)	0.1013(3)	0.1013(3)	-2.03%	-2.02%	-0.676%	-0.735%
P 14e	0.1040(52)	0.1004(1)	0.1004(1)	0.0980(3)	0.0980(3)	-3.42%	-3.46%	-5.76%	-5.78%
P 12e	0.1070(54)	0.1042(1)	0.1042(1)	0.1050(4)	0.1050(4)	-2.66%	-2.64%	-1.84%	-1.90%
P 10e	0.1090(55)	0.1044(1)	0.1044(1)	0.1033(4)	0.1032(4)	-4.18%	-4.20%	-5.24%	-5.31%
P 8e	0.1120(56)	0.1084(2)	0.1084(2)	0.1096(5)	0.1095(5)	-3.25%	-3.25%	-2.17%	-2.20%
P 6e	0.1140(57)	0.1117(2)	0.1117(2)	0.1118(5)	0.1118(6)	-2.06%	-2.01%	-1.94%	-1.93%
P 4e	0.1190(60)	0.1104(2)	0.1104(2)	0.1047(6)	0.1043(7)	-7.24%	-7.26%	-12.0%	-12.3%
P 2e	0.1230(62)	0.1168(2)	0.1171(3)	0.1162(6)	0.1162(7)	-5.08%	-4.78%	-5.50%	-5.56%
R 0e	0.1280(64)	0.1226(2)	0.1232(4)	0.1235(7)	0.1235(11)	-4.26%	-3.72%	-3.54%	-3.48%
R 2e	0.1200(60)	0.1146(2)	0.1147(2)	0.1126(7)	0.1128(7)	-4.51%	-4.46%	-6.16%	-6.00%
R 4e	0.1150(58)	0.1089(2)	0.1087(2)	0.1093(6)	0.1092(6)	-5.33%	-5.45%	-5.00%	-5.05%
R 6e	0.1130(57)	0.1077(2)	0.1076(2)	0.1071(5)	0.1069(5)	-4.71%	-4.79%	-5.25%	-5.39%
R 8e	0.1100(55)	0.1058(1)	0.1058(1)	0.1081(4)	0.1082(4)	-3.78%	-3.82%	-1.73%	-1.64%
R 10e	0.1080(54)	0.1048(1)	0.1048(1)	0.1069(4)	0.1070(4)	-2.95%	-2.97%	-1.04%	-0.972%
R 12e	0.1050(53)	0.1016(1)	0.1015(1)	0.0991(3)	0.0989(3)	-3.25%	-3.37%	-5.59%	-5.77%
R 14e	0.1030(52)	0.1010(1)	0.1010(1)	0.0989(3)	0.0988(3)	-1.93%	-1.98%	-4.02%	-4.04%
R 16e	0.1010(51)	0.0978(1)	0.0978(1)	0.0955(3)	0.0954(3)	-3.19%	-3.13%	-5.49%	-5.54%
R 18e	0.0990(50)	0.0959(1)	0.0960(1)	0.0972(3)	0.0972(3)	-3.10%	-3.00%	-1.86%	-1.80%
R 20e	0.0970(49)	0.0940(1)	0.0939(1)	0.0960(3)	0.0962(3)	-3.14%	-3.15%	-1.000%	-0.876%
R 22e	0.0950(48)	0.0922(1)	0.0923(1)	0.0948(3)	0.0950(3)	-2.92%	-2.80%	-0.232%	-0.0526%
R 24e	0.0930(47)	0.0900(1)	0.0902(1)	0.0946(4)	0.0947(4)	-3.20%	-3.06%	1.71%	1.87%
R 26e	0.0910(46)	0.0882(1)	0.0882(1)	0.0916(4)	0.0916(4)	-3.08%	-3.04%	0.681%	0.648%
R 28e	0.0890(45)	0.0862(1)	0.0864(1)	0.0919(4)	0.0921(4)	-3.13%	-2.91%	3.26%	3.53%
R 30e	0.0870(44)	0.0828(1)	0.0829(1)	0.0892(5)	0.0892(5)	-4.80%	-4.77%	2.49%	2.53%
R 32e	0.0850(43)	0.0821(2)	0.0821(2)	0.0871(5)	0.0872(5)	-3.41%	-3.36%	2.46%	2.62%
R 34e	0.0840(42)	0.0785(2)	0.0786(2)	0.0827(5)	0.0830(5)	-6.55%	-6.49%	-1.51%	-1.25%
R 36e	0.0820(41)	0.0765(2)	0.0767(2)	0.0773(6)	0.0775(6)	-6.66%	-6.50%	-5.78%	-5.45%
R 38e	0.0800(40)	0.0753(2)	0.0755(2)	0.0719(6)	0.0721(6)	-5.85%	-5.66%	-10.1%	-9.90%
R 40e	0.0790(40)	0.0710(2)	0.0713(2)	0.0654(5)	0.0651(6)	-10.1%	-9.73%	-17.2%	-17.7%
R 42e	0.0770(39)	0.0720(2)	0.0739(2)	0.0693(5)	0.0708(6)	-6.48%	-4.04%	-9.99%	-8.03%
R 44e	0.0760(38)	0.0723(2)	0.0756(3)	0.0757(5)	0.0852(8)	-4.82%	-0.526%	-0.434%	12.2%
R 46e	0.0740(37)	0.0708(2)	0.0744(3)	0.0754(5)	0.0872(10)	-4.30%	0.554%	1.82%	17.8%
R 48e	0.0730(37)	0.0685(2)	0.0715(4)	0.0687(5)	0.0712(11)	-6.15%	-2.11%	-5.93%	-2.45%
R 50e	0.0720(36)	0.0658(2)	0.0662(5)	0.0652(6)	0.0651(10)	-8.64%	-8.04%	-9.50%	-9.65%
The uncertainities listed in parentheses are one standard deviation in units of the last quoted digit									

Figure (4.4): Example of globar and synchrotron spectra and their fitting residuals.

The retrieved intensities, air- and self-broadening coefficients were compared to values published in literature and to HITRAN08 values and shown in graphs (4.5), (4.6) and (4.7), respectively. The parameters retrieved using the Voigt profile are in better agreement with similar published values than the speed-dependent ones. The spectral line intensities retrieved using the Voigt profile have average deviations of 2.05%, 2.13%, 2.23% and 3.01% from values reported by HITRAN08[20], Dana et al. [105], Johns &Noel [102] and Devi et al. [106, 107], respectively. Figure (4.5) shows that our results have some shift either up or down relative to values published in the literature. These patterns observed in our results can be attributed to the different calibrations of the pressure and temperature gauges used in individual studies. The air-broadening coefficients are more accurate than intensity as their average deviations are 1.23%, 1.28% and 1.72% from HITRAN08 [20], Devi et al. [112] and Devi et al. [106, 107], respectively. The new self-broadening coefficients have the least accuracy when compared to the literature since the average deviations are 4.37%, 3.53% and 4.92% from HITRAN08 [20], Dana et al. [105] and Devi et al. [106, 107], respectively. Larger deviations of our self-broadening coefficients compared to the air-broadening coefficients confirm our preliminary conclusion that mainly synchrotron spectra with higher SNR produce better results than the globar ones. The deviation of the spectral parameters is calculated using the following equation[31]:

$$\text{Parameter deviation} = \left[\frac{\text{Present work} - \text{literature}}{\text{Present work}}\right] \times 100 \qquad (4.7)$$

---

[31] Present work is used as common denominator to facilitate the comparison of different literature studies simultaneously.
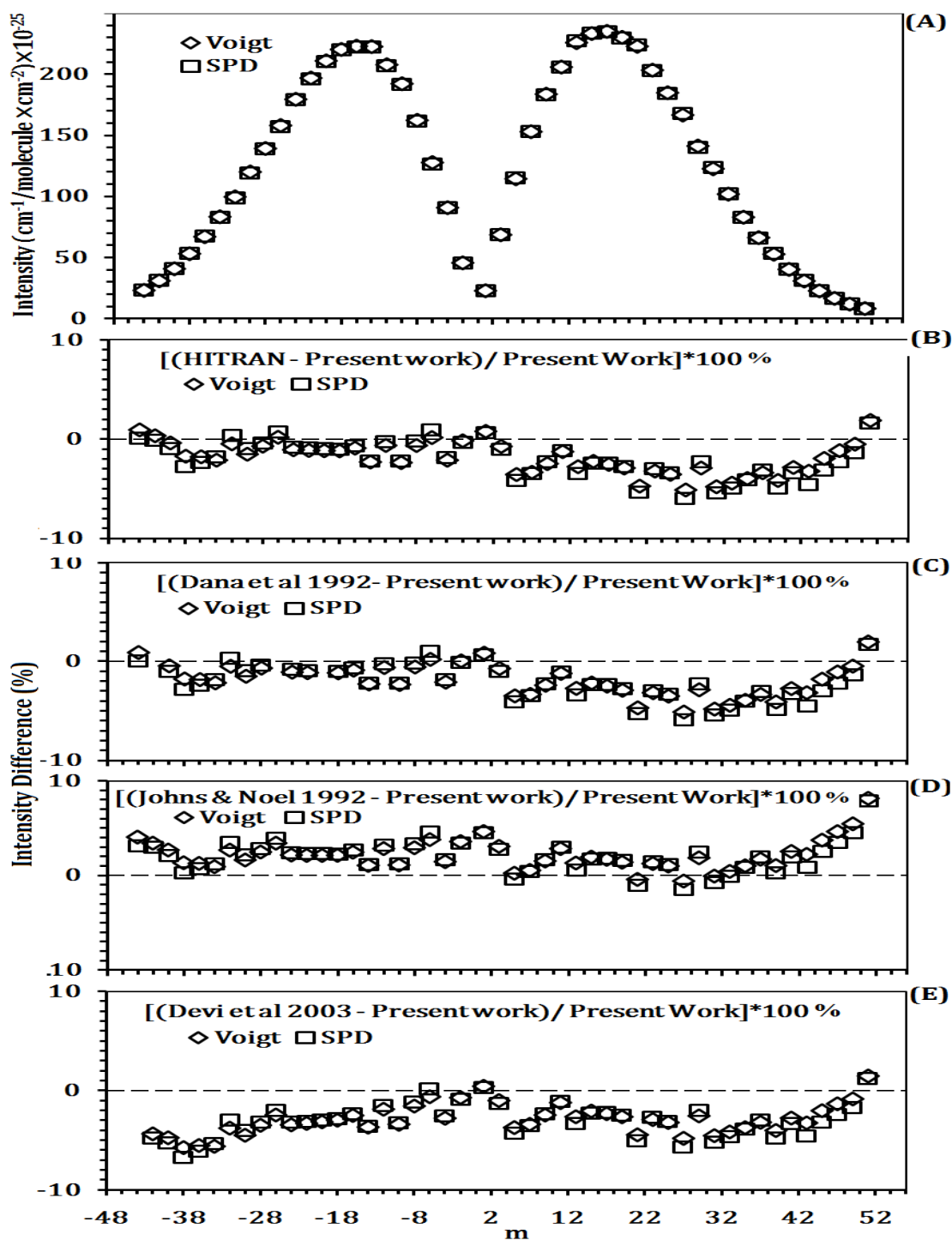
Figure (4.5): (A) Laser band I retrieved line intensities as a function of rotational quantum number index m, (B) difference from HITRAN08 [20], (C) difference from Dana et al [105], (D) difference from Johns &Noel [102] and (E) difference from Devi et al. [106, 107].
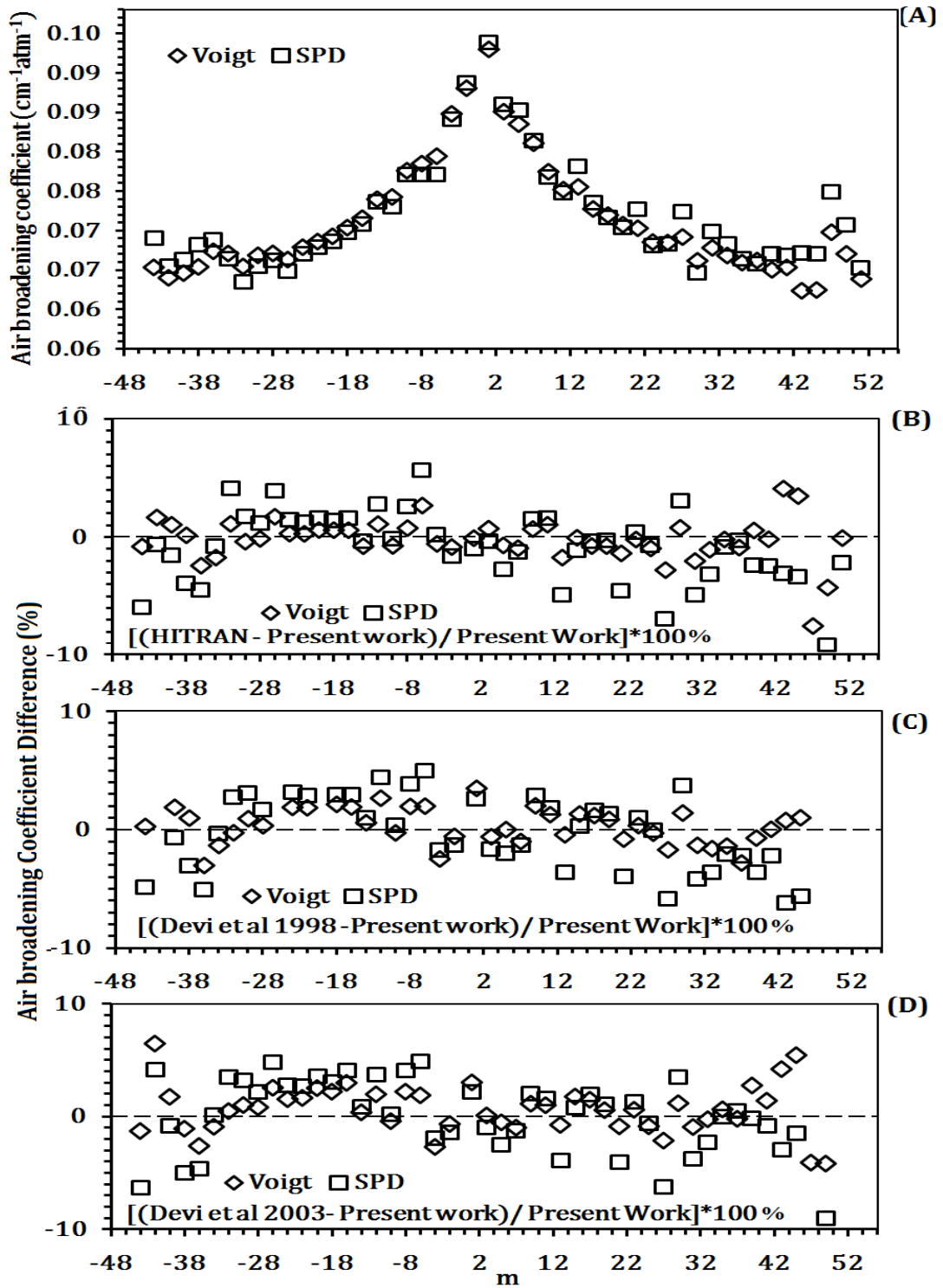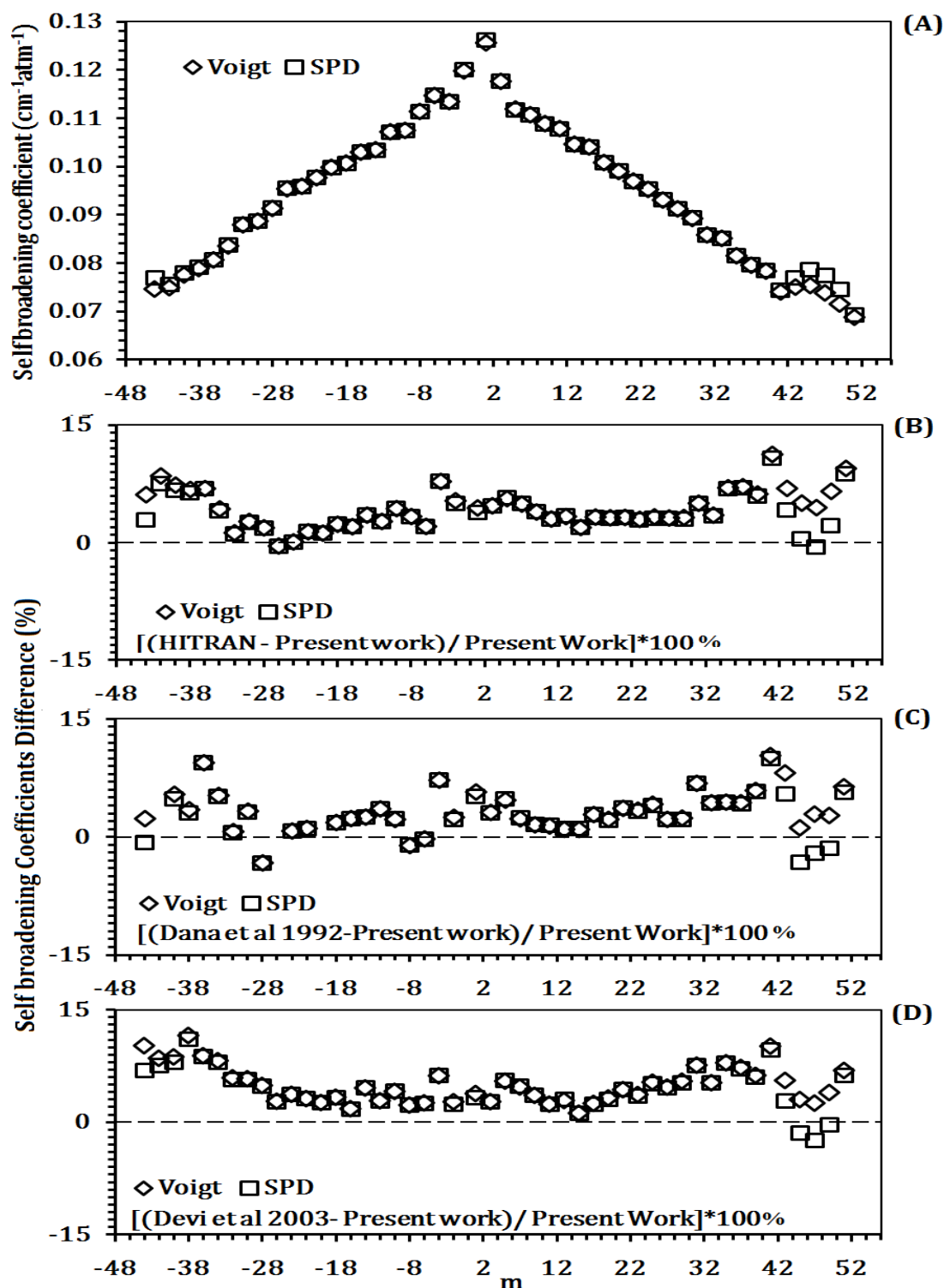
Figure (4.6): (A) Laser band I air-broadening coefficients as a function of rotational quantum number index m, (B) difference from HITRAN08 [20], (C) difference from Devi et al. [112] and (D) difference from Devi et al. [106, 107].

Figure (4.7): Laser band I self broadening coefficients as a function of rotational quantum number index m, (B) difference from HITRAN08 [20], (C) difference from Dana et al [105] and (D) difference from Devi et al. [106, 107].

4.5: Effect of Errors in Channel Parameters

In order to achieve error minimization using the channel fitting technique, channel parameters have to be floated (i.e. allowed to change in the fitting process). Because of the large number of channels needed to model a wide spectral range, the multispectrum fit can have a large number of channels (the last example had 142 channels). This large number of channels will impact the computational speed of the fit, especially when using the SPD profile. These slow processing times can be an obstacle if fitting parameters have to be changed occasionally. For these reasons, we performed an error analysis by introducing errors into the input channel spectra parameters and measuring their impact on the retrieved spectral line parameters. Since the channel amplitude has the most important influence on line parameters and since period and phase are determined relatively accurately, errors equal to 5, 10 and 15% were introduced in all 142 channel spectra amplitudes. The retrieved line parameters with these errors added are shown in figures (4.8), (4.9) and (4.10) for intensity, air-broadening, and self-broadening, respectively. These results showed that air-broadening is the most susceptible to channel errors in our fit, which can be attributed to the fact that the 13 air-broadened spectra in our fit are synchrotron ones and have severe channelling. However, line intensity and self-broadening were less affected since there are globar spectra in our fit with no or weak channel effects, which demonstrate another advantage of multispectrum fitting.
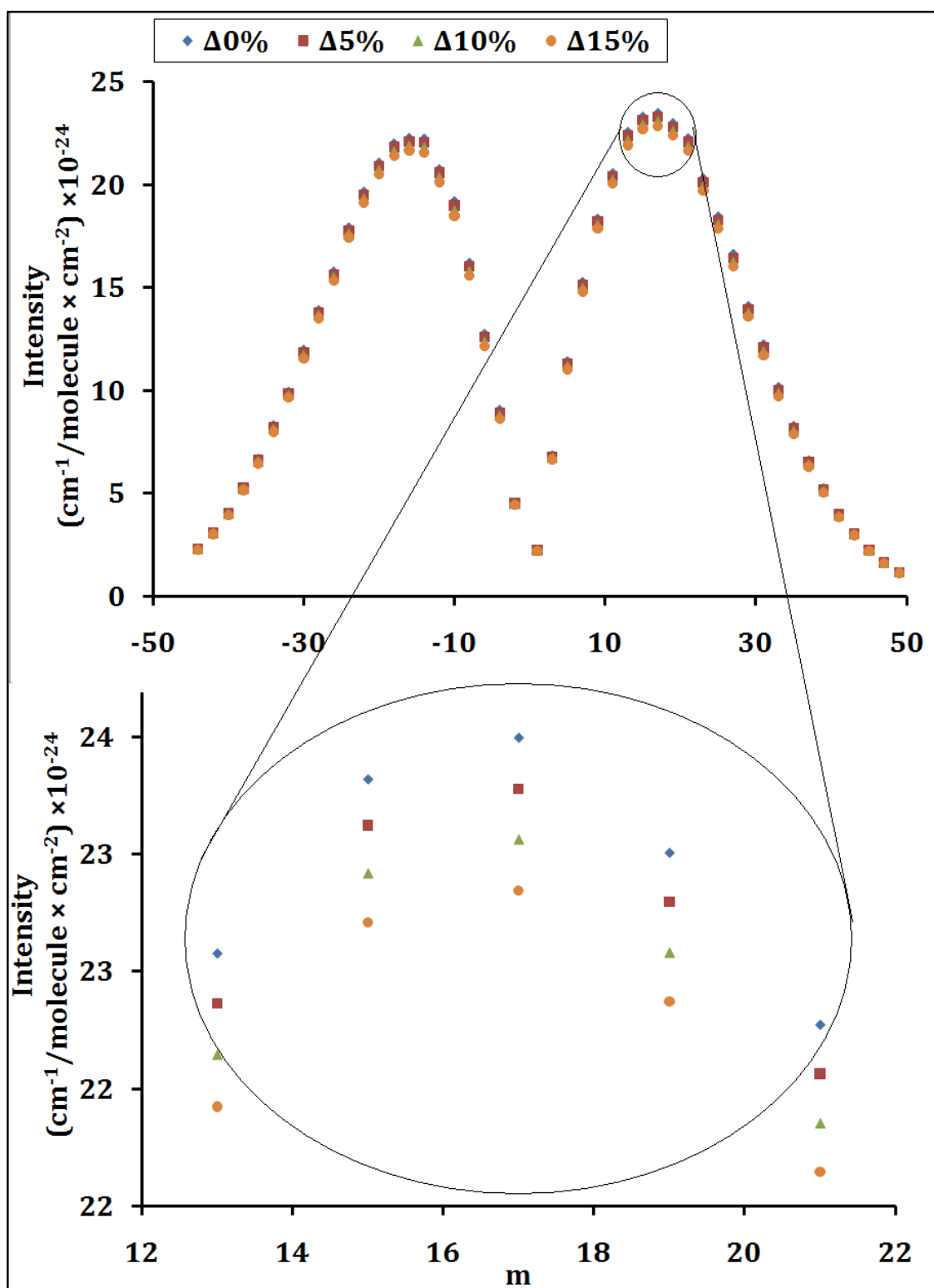
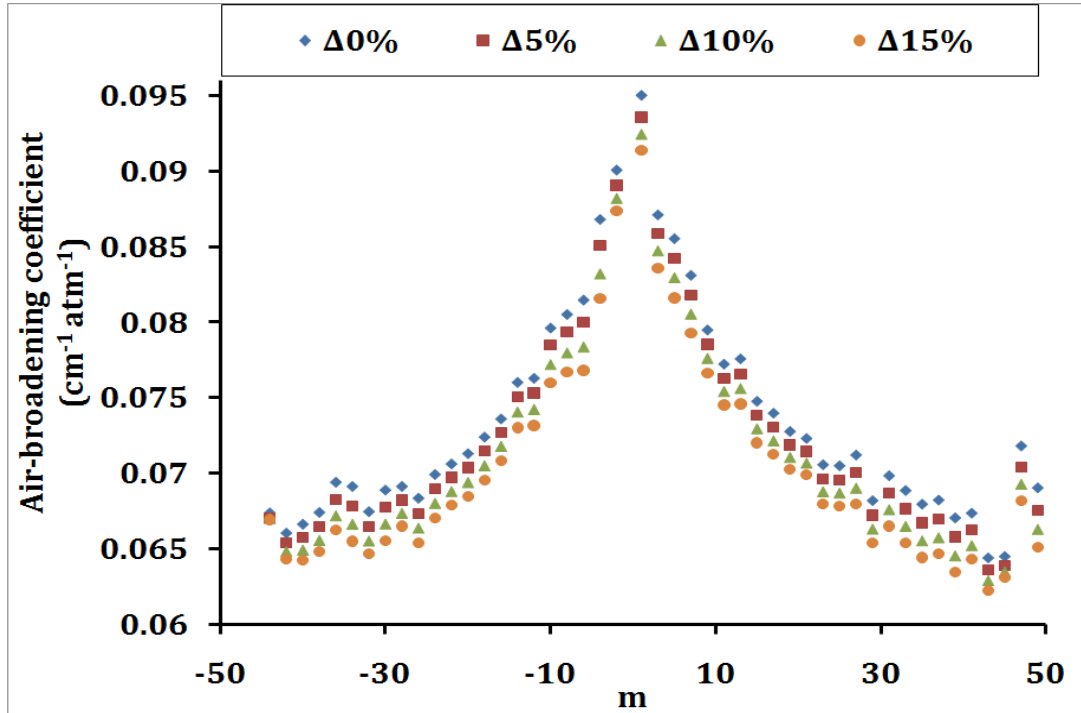Figure (4.7): Effect of channel spectra errors on calculated line intensities.

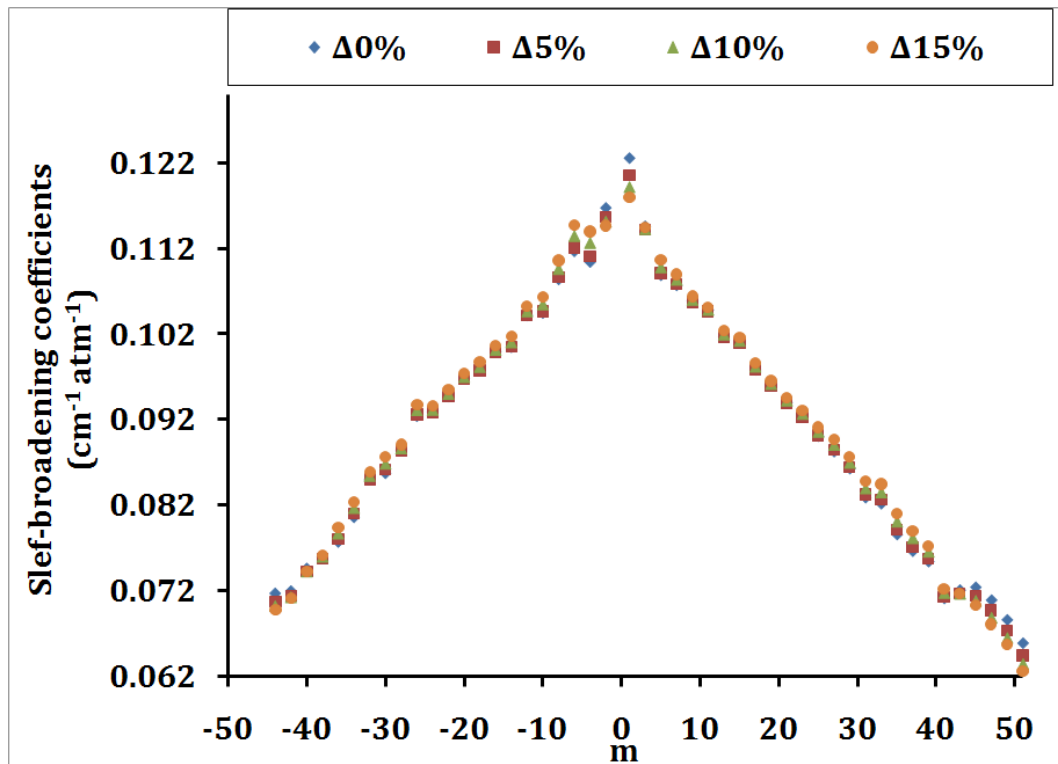Figure (4.8): Effect of channel spectra errors on calculated air-broadening coefficients.

Figure (4.9): Effect of channel spectra errors on calculated self-broadening coefficients.

4.6: Concluding Remarks

In this chapter we examined the improvement on quality of line parameter fits offered by the channel fitting technique. The tests were made on transitions belonging to the carbon dioxide laser band I ($00011 \leftarrow 10001$). The improvement was achieved using iterative fitting of channel spectra employed to better model the spectra, and ultimately to remove the structure from the residual of the Labfit fits. Twenty-four spectra were used for the tests, 20 of which had visible channel spectra. The line parameters were retrieved using both Voigt and speed-dependent (SPD) Voigt profiles. Results for intensities, air- and self-broadening coefficients were compared to HITRAN and other literature values. The average deviation of retrieved intensities ranged from 2.05% to 3.07% with respect to HITRAN and published results. The deviations observed for air-broadening coefficients were smaller due to the higher quality of synchrotron spectra used in the retrieval and they ranged from 1.23% to 1.72% compared to HITRAN and literature values. Although the globar spectra had less channelling effects than the synchrotron ones, the self-broadening coefficients retrieved from the globar spectra were less accurate due to the lower SNR of these spectra, compared to the synchrotron spectra. The air-broadening coefficients showed average deviations from 4.37% to 4.92% when compared to HITRAN data and previous published results. Given that HITRAN08's uncertainty limits for intensities are $\geq 2\%$ and $< 5\%$, and $\geq 5\%$ and $< 10\%$ for air- and self-broadening, these results indicate that the channel handling technique did not cause any degradation in the quality of retrieved spectral parameters.

The effect of errors in the fitted channel amplitudes was also investigated by introducing errors to the fitted channel amplitudes and fixing them in the fit process. Results showed that parameters that were completely derived from spectra affected by severe channel spectra are more susceptible to these errors than parameters that depend on a combination of channelled and channel-free spectra. For this reason, simultaneous fitting of synchrotron and globar spectra in the multispectrum fit is advantageous in mitigating the channelling effects on the retrieved spectral parameters.

Chapter 5: Conclusion

In the first chapter, we outlined the importance of having available accurate parameters for spectroscopic remote sensing of atmospheric greenhouse gases. The relationship between Beer's law and the spectral line shape was discussed. Several line shape profiles available in the literature and the line mixing effects on spectra were also discussed. Due to its versatility for both remote sensing applications and laboratory studies, the FTIR technique was chosen for this study. In chapter two, the aspects of improving the performance of FTIR spectrometers by using synchrotron sources were examined and discussed. Although synchrotron sources provide high radiance with small source size, which is suitable for high-resolution FTIR measurements, the increase of channel spectra due to the higher radiation coherency and the complicated transfer optics hinder its accuracy for given applications.

Seven different techniques for handling channel spectra were investigated in chapter 3. The techniques were applied separately to the same group of seven carbon dioxide spectra recorded using the synchrotron source. Analysis of the resulting spectra showed that the best way to improve SNR of spectra is to use background spectra with the same sample channel spectra in creating transmission spectra. However, examining the spectral accuracy of retrieved intensity and air-broadening coefficients for 21 spectral lines showed that the spectral fitting technique using small spectral ranges is more accurate. Using channel spectra fitting techniques resulted in much better modeling of the spectra. The average STDV of

the fit is reduced from 2.12% obtained without channel handling to 0.53% with channel handling by fitting small spectral segments about 5.5 cm^{-1} wide. Applying the spectral technique to a wider range of 33 cm^{-1} resulted in the STDV of the fit equal to 0.62%. This decrease in ability to fit the channel spectra over a wide spectral range is due to the change in parameters of channel spectra (amplitude, period and phase) with wavelength.

In order to overcome the limitation of the channel spectra fitting technique to narrow spectral ranges, an iterative procedure for channel spectra fitting was introduced and used to analyze the complete carbon dioxide laser band I. In this procedure, channels were fitted and the new residual of the fit was used to measure the remaining channel to include in the fit. The analysis used 24 spectra, 13 for carbon dioxide and air mixtures and 11 for pure carbon dioxide samples. All spectra of carbon dioxide and air mixtures and 3 of the pure carbon dioxide spectra were recorded using the synchrotron source, while the remaining 8 pure carbon dioxide spectra were recorded using the globar source. The deviations of retrieved line parameters from HITRAN were within the uncertainty range of the HITRAN database and the fitting residuals were overall improved. The retrieved parameters were also compared to parameters published in the literature. The agreement between our results and the literature values is within the uncertainty range of HITRAN data.

The effect of errors in channel spectra parameters (such as amplitude) used in the fitting process on the retrieved spectral parameters was examined. The

introduction of errors in the channel amplitudes used in the multispectral fitting resulted in errors in retrieved spectral parameters. The most susceptible to these errors were parameters derived from only spectra with spectral channels . However, when the parameter was derived from both spectra with spectral channels (synchrotron source) and channel-free spectra (Globar source), the impact of channel errors was mitigated. Therefore, using the multispectral program to remove channel spectra proved to be useful when spectra little or no channelling are included to help reduce the effect due to channel errors on the fit retrieved results.

In conclusion, testing and examining of channel spectra handling by spectral fitting showed many advantages such as:

1. It is able to reduce the effects of channel spectra without making any changes to the original measured spectra.

2. It is able to improve its effective range and efficiency by iterative fitting of channels.

3. It does not require information regarding the spectrometer, source, or measurement conditions to handle channels.

4. It is included in the spectral analysis directly, saving processing time and enabling the assessment of its effect on retrieved spectral parameters.

5. It can use channel-free spectra in the fitting process to help reduce the effect of errors caused by errors in channel spectra fitting.

References

[1] Lorius, C., J. Jouzel, D. Raynaud, J. Hansen, and H. Letreut, THE ICE-CORE RECORD - CLIMATE SENSITIVITY AND FUTURE GREENHOUSE WARMING. *Nature*, 1990. 347(6289): 139-145.

[2] Fleming, J.R., Joseph Fourier, the 'greenhouse effect', and the quest for a universal theory of terrestrial temperatures. *Endeavour*, 1999. 23(2): 72-75.

[3] Philipona, R., B. Durr, C. Marty, A. Ohmura, and M. Wild, Radiative forcing - measured at Earth's surface - corroborate the increasing greenhouse effect. *Geophysical Research Letters*, 2004. 31(3): L03202.

[4] Vazquez, G.J., Optical remote sensing of atmospheric compounds. *Proc. SPIE:Second Iberoamerican Meeting on Optics*, 1996. 2730: 2730131-149.

[5] Intergovernmental Panel on Climate Change (IPCC), The Physical Science Basis-Contribution of Working Group I, in *the Fourth Assessment Report of the Intergovernmental Panel on Climate Change(IPCC)*. 2007, Cambridge, UK, Cambridge University Press: 135.

[6] Flaud, J.M., A. Perrin, B. Picquet-Varrault, A. Gratien, J. Orphal, and J.-F. Doussin, Quantitative Spectroscopy and Atmospheric Measurements in *Remote sensing of the atmosphere for environmental security : [proceedings of the NATO Advanced Research Workshop on Remote Sensing of the Atmosphere for Environmental Security, Rabat, Morocco, 16-19 November 2005]*, A. Perrin, N. Ben Sari-Zizi, and J. Demaison, Editors. 2006, Dordrecht,

Springer, published in cooperation with NATO Public Diplomacy Division: 107 -121.

[7]   Committee on Methods for Estimating Greenhouse Gas Emissions. National Research Council., *Verifying greenhouse gas emissions : methods to support international climate agreements*. 2010, Washington, DC, National Academies Press: 93-101.

[8]   Crisp, D., The Orbiting Carbon Observatory: NASA's first dedicated carbon dioxide mission. **Proc. SPIE: Sensors, Systems, and Next-Generation Satellites XII**, 2008. 7106: 710604-7.

[9]   Crisp, D., C.E. Miller, and P.L. DeCola, NASA Orbiting Carbon Observatory: measuring the column averaged carbon dioxide mole fraction from space. **Journal of Applied Remote Sensing**, 2008. 2: 023508.

[10]   Hamazaki, T., Y. Kaneko, A. Kuze, and H. Suto, Greenhouse Gases Observation from Space with TANSO-FTS on GOSAT. **In Proc. of Fourier Transform Spectroscopy/ Hyperspectral Imaging and Sounding of the Environment, Optical Society of America Technical Digest Series**, 2007: FWB1.

[11]   Shiomi, K., S. Kawakami, T. Kina, Y. Mitomi, M. Yoshida, N. Sekio, F. Kataoka, and R. Higuchi, Calibration plan of GOSAT sensors. **Proc. SPIE: Sensors, Systems, and Next-Generation Satellites XI**, 2007. 6744: 67440G-11.

[12]   Noel, S., H. Bovensmann, J.P. Burrows, J. Frerick, K.V. Chance, A.P.H. Goede, and C. Muller, The SCIAMACHY instrument on ENVISAT-1. **Proc. SPIE: Sensors, Systems, and Next-Generation Satellites II**, 1998. 3498: 94-104.

[13]   Buchwitz, M., R. de Beek, S. Noël, J.P. Burrows, H. Bovensmann, H. Bremer, P. Bergamaschi, S. Körner, and M. Heimann, Carbon monoxide, methane and carbon dioxide columns retrieved from SCIAMACHY by WFM-DOAS: year 2003 initial data set. **Atmos. Chem. Phys.**, 2005. 5(12): 3313-3329.

[14]   Aumann, H.H., M.T. Chahine, C. Gautier, M.D. Goldberg, E. Kalnay, L.M. McMillin, H. Revercomb, P.W. Rosenkranz, W.L. Smith, D.H. Staelin, L.L. Strow, and J. Susskind, AIRS/AMSU/HSB on the Aqua mission: design, science objectives, data products, and processing systems. **Geoscience and Remote Sensing, IEEE Transactions on**, 2003. 41(2): 253-264.

[15]   Chahine, M.T., L. Chen, P. Dimotakis, X. Jiang, Q.B. Li, E.T. Olsen, T. Pagano, J. Randerson, and Y.L. Yung, Satellite remote sounding of mid-tropospheric CO_2. **Geophysical Research Letters**, 2008. 35(17): L17807.

[16]   Phulpin, T., D. Blumstein, F. Prel, B. Tournier, P. Prunet, and P. Schlussel, Applications of IASI on MetOp-A: first results and illustration of potential use for meteorology, climate monitoring, and atmospheric chemistry. **Proc. SPIE: Atmospheric and Environmental Remote Sensing Data Processing and Utilization III: Readiness for GEOSS**, 2007. 6684: 66840F-12.

[17]   Crevoisier, C., A. Chedin, H. Matsueda, T. Machida, R. Armante, and N.A. Scott, First year of upper tropospheric integrated content of CO_2 from IASI hyperspectral infrared observations. **Atmospheric Chemistry and Physics**, 2009. 9(14): 4797-4810.

[18]   Dufour, G., A. Valentin, A. Henry, D. Hurtmans, and C. Camy-Peyret, Concentration measurements of ozone in the 1200-300 ppbv range: an

intercomparison between the BNM ultraviolet standard and infrared methods*. **Spectrochimica Acta Part a-Molecular and Biomolecular Spectroscopy**, 2004. 60(14): 3345-3352.

[19]   Picquet-Varrault, B., J. Orphal, J.F. Doussin, P. Carlier, and J.M. Flaud, Laboratory intercomparison of the ozone absorption coefficients in the mid-infrared (10 mu m) and ultraviolet (300-350 nm) spectral regions*. **Journal of Physical Chemistry A**, 2005. 109(6): 1008-1014.

[20]   Rothman, L.S., I.E. Gordon, A. Barbe, D.C. Benner, P.E. Bernath, M. Birk, V. Boudon, L.R. Brown, A. Campargue, J.P. Champion, K. Chance, L.H. Coudert, V. Dana, V.M. Devi, S. Fally, J.M. Flaud, R.R. Gamache, A. Goldman, D. Jacquemart, I. Kleiner, N. Lacome, W.J. Lafferty, J.Y. Mandin, S.T. Massie, S.N. Mikhailenko, C.E. Miller, N. Moazzen-Ahmadi, O.V. Naumenko, A.V. Nikitin, J. Orphal, V.I. Perevalov, A. Perrin, A. Predoi-Cross, C.P. Rinsland, M. Rotger, M. Simeckova, M.A.H. Smith, K. Sung, S.A. Tashkun, J. Tennyson, R.A. Toth, A.C. Vandaele, and J. Vander Auwera, The HITRAN 2008 molecular spectroscopic database*. **Journal of Quantitative Spectroscopy & Radiative Transfer**, 2009. 110(9-10): 533-572.

[21]   Brown, L.R., M.R. Gunson, R.A. Toth, F.W. Irion, C.P. Rinsland, and A. Goldman, 1995 atmospheric trace molecule spectroscopy (ATMOS) linelist*. **Applied Optics**, 1996. 35(16): 2828-2848.

[22]   Jacquinet-Husson, N., N.A. Scott, A. Chédin, K. Garceran, R. Armante, A.A. Chursin, A. Barbe, M. Birk, L.R. Brown, C. Camy-Peyret, C. Claveau, C. Clerbaux, P.F. Coheur, V. Dana, L. Daumont, M.R. Debacker-Barilly, J.M. Flaud,

A. Goldman, A. Hamdouni, M. Hess, D. Jacquemart, P. Köpke, J.Y. Mandin, S. Massie, S. Mikhailenko, V. Nemtchinov, A. Nikitin, D. Newnham, A. Perrin, V.I. Perevalov, L. Régalia-Jarlot, A. Rublev, F. Schreier, I. Schult, K.M. Smith, S.A. Tashkun, J.L. Teffo, R.A. Toth, V.G. Tyuterev, J. Vander Auwera, P. Varanasi, and G. Wagner, The 2003 edition of the GEISA/IASI spectroscopic database. **Journal of Quantitative Spectroscopy and Radiative Transfer**, 2005. 95(4): 429-467.

[23] Coleman, M.D. and T.D. Gardiner, Sensitivity of model-based quantitative FTIR to instrumental and spectroscopic database error sources. **Vibrational Spectroscopy**, 2009. 51(2): 177-183.

[24] Bernath, P.F., *Spectra of atoms and molecules*. 2nd ed. 2005, New York, Oxford University Press: 160 - 200.

[25] Hollas, J.M., *Modern spectroscopy*. 4th ed. 2004, New Jersey, J. Wiley: 137-180.

[26] Morse, P.M., Diatomic Molecules According to the Wave Mechanics. II. Vibrational Levels. **Physical Review**, 1929. 34(1): 57-64.

[27] Griffiths, P.R., Introduction to vibrational Spectroscopy in *Handbook of vibrational spectroscopy*, J.M. Chalmers and P.R. Griffiths, Editors. 2002, New York, J. Wiley: 326-336.

[28] Rothman, L.S. and L.D.G. Young, Infrared energy levels and intensities of carbon dioxide--II. **Journal of Quantitative Spectroscopy and Radiative Transfer**, 1981. 25(6): 505-524.

[29]   Günzler, H. and H.M. Heise, *IR spectroscopy : an introduction*. 2002, Weinheim, Wiley-VCH: 25-30.

[30]   Fermi, E., Über den Ramaneffekt des Kohlendioxyds. **Zeitschrift für Physik A Hadrons and Nuclei**, 1931. 71(3): 250-259.

[31]   Hollas, J.M., *High resolution spectroscopy*. 2nd ed. 1998, Chichester ; New York, J. Wiley: 248.

[32]   Koelliker Delgado, J. (2006). *Amount of Carbon Dioxide Fraction Determination by TDLAS: Evidences for a Potential Primary Method Directly Applied in Gas Analysis.* PhD Thesis Technical University Carolo-Wilhelmina zu Braunschweig, Braunschweig. Retrieved from http://www.digibib.tu-bs.de/?docid=00000059

[33]   Herzberg, G., *Molecular spectra and molecular structure: II: infrared and Raman spectra of ployatomic molecules*. 2d ed. 1950, New York, Van Nostrand: 274.

[34]   López-Puertas, M. and F.W. Taylor, *Non-LTE radiative transfer in the atmosphere*. Series on atmospheric, oceanic and planetary physics. 2001, River Edge, NJ, World Scientific: 433-436.

[35]   Griffiths, P.R., Beer's Law, in *Handbook of vibrational spectroscopy*, P.R. Griffiths, Editor. 2002, New York, J. Wiley: 2225-2234.

[36]   Liu, Y.Y., J.L. Lin, G.M. Huang, Y.Q. Guo, and C.X. Duan, Simple empirical analytical approximation to the Voigt profile. **Journal of the Optical Society of America B-Optical Physics**, 2001. 18(5): 666-672.

[37]   D'Eu, J.F., B. Lemoine, and F. Rohart, Infrared HCN lineshapes as a test of galatry and speed-dependent voigt profiles. **Journal of Molecular Spectroscopy**, 2002. 212(1): 96-110.

[38]   Dicke, R.H., The Effect of Collisions upon the Doppler Width of Spectral Lines. **Physical Review**, 1953. 89(2): 472-473.

[39]   Galatry, L., Simultaneous Effect of Doppler and Foreign Gas Broadening on Spectral Lines. **Physical Review**, 1961. 122(4): 1218-&.

[40]   Rautian, S.G. and I.I. Sobelman, Effect of Collisions on Doppler Broadening of Spectral Lines. **Soviet Physics Uspekhi-Ussr**, 1967. 9(5): 701-716.

[41]   Wlodarczak, G., J.-M. Colmont, and F. Rohart, Quantitative Rotational Spectroscopy for Atmospheric Research, in *Remote sensing of the atmosphere for environmental security : [proceedings of the NATO Advanced Research Workshop on Remote Sensing of the Atmosphere for Environmental Security, Rabat, Morocco, 16-19 November 2005]*, A. Perrin, N. Ben Sari-Zizi, and J. Demaison, Editors. 2006, Dordrecht, Springer, published in cooperation with NATO Public Diplomacy Division: 221 - 235.

[42]   Berman, P.R., Speed-Dependent Collisional Width and Shift Parameters in Spectral Profiles. **Journal of Quantitative Spectroscopy & Radiative Transfer**, 1972. 12(9): 1331-1342.

[43]   Kochel, J.M., J.M. Hartmann, C. CamyPeyret, R. Rodrigues, and S. Payan, Influence of line mixing on absorption by CO_2 Q branches in atmospheric balloon-borne spectra near 13 mu m. **Journal of Geophysical Research-Atmospheres**, 1997. 102(11D): 12891-12899.

[44]   Hartmann, J.M., H. Tran, and G.C. Toon, Influence of line mixing on the retrievals of atmospheric CO2 from spectra in the 1.6 and 2.1 μm regions. **Atmos. Chem. Phys. Discuss.**, 2009. 9(1): 4873-4898.

[45]   Bernath, P.F., C.T. McElroy, M.C. Abrams, C.D. Boone, M. Butler, C. Camy-Peyret, M. Carleer, C. Clerbaux, P.F. Coheur, R. Colin, P. DeCola, M. DeMazière, J.R. Drummond, D. Dufour, W.F.J. Evans, H. Fast, D. Fussen, K. Gilbert, D.E. Jennings, E.J. Llewellyn, R.P. Lowe, E. Mahieu, J.C. McConnell, M. McHugh, S.D. McLeod, R. Michaud, C. Midwinter, R. Nassar, F. Nichitiu, C. Nowlan, C.P. Rinsland, Y.J. Rochon, N. Rowlands, K. Semeniuk, P. Simon, R. Skelton, J.J. Sloan, M.A. Soucy, K. Strong, P. Tremblay, D. Turnbull, K.A. Walker, I. Walkty, D.A. Wardle, V. Wehrle, R. Zander, and J. Zou, Atmospheric Chemistry Experiment (ACE): Mission overview. **Geophysical Research Letters**, 2005. 32(15): L15S01.

[46]   Payan, S., J. De La Noe, A. Hauchecorne, and C. Camy-Peyret, A review of remote sensing techniques and related spectroscopy problems. **Comptes Rendus Physique**, 2005. 6(8): 825-835.

[47]   Rosenkranz, P., Shape of the 5 mm oxygen band in the atmosphere. **Antennas and Propagation, IEEE Transactions on**, 1975. 23(4): 498-506.

[48]   Smith, M.A.H., Recent results on infrared molecular line broadening and shift parameters, in *Remote sensing of the atmosphere for environmental security : [proceedings of the NATO Advanced Research Workshop on Remote Sensing of the Atmosphere for Environmental Security, Rabat, Morocco, 16-19 November 2005]*, A. Perrin, N. Ben Sari-Zizi, and J. Demaison, Editors. 2006,

Dordrecht, Springer, published in cooperation with NATO Public Diplomacy Division: 185 - 201.

[49] Levy, A., N. Lacome, and C. Chackerian, Collisional line mixing, in *Spectroscopy of the Earth's atmosphere and interstellar medium*, K. Rao and A. Weber, Editors. 1992, Academic Press: 261-337.

[50] Moritz, R.E., *On mathematics and mathematicians*. 1958, New York, Dover Publications: 58.

[51] Smith, B.C., *Fundamentals of Fourier transform infrared spectroscopy*. 1996, Boca Raton, CRC Press: 9-10, 31-40.

[52] Buijs, H. *History of Fourier Transform Spectrometer Technology Development*. in *26th ISTS (International Symposium on Space Technology and Science)*. 2008. Hamamatsu City, Japan: 2008-o-4-06v

[53] Jongbloets, H.W.H.M., M.J.H. Vandesteeg, E.J.C.M. Vanderwerf, J.H.M. Stoelinga, and P. Wyder, Spectrum Distortion in Far-Infrared Fourier Spectroscopy by Multiple Reflections between Sample and Michelson Interferometer. **Infrared Physics**, 1980. 20(3): 185-192.

[54] Perkins, W.D., Topics in chemical instrumentation – Fourier transform infrared spectroscopy. Part II : FTIR advantages. **Journal of Chemical Education**, 1987. 64(11): A269-A271.

[55] Mozayeni, F., Applications of FT-IR Spectroscopy. **Journal of the American Oil Chemists' Society**, 1988. 65(9): 1420-1426.

[56] Wartewig, S., *IR and Raman spectroscopy : fundamental processing*. Spectroscopic techniques. 2003, Weinheim, Wiley-VCH: 37-40.

[57] Tripp, C.P. and R.A. Mcfarlane, Discussion of the Stray Light Rejection Efficiency of Ft-Ir Spectrometers - the Effects of Sample Emission on Ft-Ir Spectra. **Applied Spectroscopy**, 1994. 48(9): 1138-1142.

[58] Hsu, C.-P.S., Infrared Spectroscopy in *Handbook of instrumental techniques for analytical chemistry*, F.A. Settle, Editor. 1997, Upper Saddle River, NJ, Prentice Hall PTR: 247-283.

[59] Vernoud, L., H.A. Bechtel, F. Borondics, and M.C. Martin. *Reconciling FTIR Spectroscopy with Top-off Operations at the Advanced Light Source.* in ***WIRMS (2009) 5TH INTERNATIONAL WORKSHOP ON INFRARED MICROSCOPY AND SPECTROSCOPY WITH ACCELERATOR BASED SOURCES.*** 2010. Alberta (Canada): AIP: 36-38

[60] Born, M., E. Wolf, and A.B. Bhatia, *Principles of Optics: Electromagnetic Theory of Propagation, Interference and Diffraction of Light.* 2000, Cambridge University Press.

[61] Herres, W. and J. Gronholtz, Understanding FT-IR data processing. Part 3. **Instruments and Computers**, 1985. 3(10).

[62] Robinson, J.W., *Atomic spectroscopy.* 2nd ed. 1996, New York, Marcel Dekker: 27-28.

[63] White, J.U., Long optical paths of large aperture. **Journal of the Optical Society of America**, 1942. 32(5): 285-288.

[64] Herriott, D., R. Kompfner, and H. Kogelnik, Off-Axis Paths in Spherical Mirror Interferometers. **Applied Optics**, 1964. 3(4): 523-526.

[65] Mcmanus, J.B., P.L. Kebabian, and W.S. Zahniser, Astigmatic Mirror Multipass Absorption Cells for Long-Path-Length Spectroscopy. **Applied Optics**, 1995. 34(18): 3336-3348.

[66] Engel, G.S. and E.J. Moyer, Precise multipass Herriott cell design: Derivation of controlling design equations. **Opt. Lett.**, 2007. 32(6): 704-706.

[67] Stephens, E.R., Long-Path Infrared Spectroscopy for Air Pollution Research. **Infrared Physics**, 1961. 1(3): 80-84.

[68] Fried, A., J.R. Drummond, B. Henry, and J. Fox, Reduction of Interference-Fringes in Small Multipass Absorption Cells by Pressure Modulation. **Applied Optics**, 1990. 29(7): 900-902.

[69] Heard, D.E., *Analytical techniques for atmospheric measurement*. 2006, Oxford ; Ames, Iowa, Blackwell Pub.: 103-106.

[70] Griffiths, P.R. and C. Homes, Instrumentation for far-infrared spectroscopy, in *Handbook of vibrational spectroscopy*, J.M. Chalmers and P.R. Griffiths, Editors. 2002, New York, J. Wiley: 326-336.

[71] Williams, G.P., Synchrotron and free electron laser sources of infrared radiation, in *Handbook of vibrational spectroscopy*, J.M. Chalmers and P.R. Griffiths, Editors. 2002, New York, J. Wiley: 341-348.

[72] Griffiths, P.R. and J.A. De Haseth, *Fourier transform infrared spectrometry*. 2nd ed. Chemical analysis v. 171. 2007, Hoboken, New Jersey, Wiley-Interscience: 160-165.

[73] Duncan, W.D. and G.P. Williams, Infrared Synchrotron Radiation from Electron Storage-Rings. **Applied Optics**, 1983. 22(18): 2914-2923.

[74] Carr, G.L., M.C. Martin, W.R. McKinney, K. Jordan, G.R. Neil, and G.P. Williams, High-power terahertz radiation from relativistic electrons. **Nature**, 2002. 420(6912): 153-156.

[75] Roy, P., J.B. Brubach, P. Calvani, G. deMarzi, A. Filabozzi, A. Gerschel, P. Giura, S. Lupi, O. Marcouille, A. Mermet, A. Nucara, J. Orphal, A. Paolone, and M. Vervloet, Infrared synchrotron radiation: from the production to the spectroscopic and microscopic applications. **Nuclear Instruments & Methods in Physics Research Section a-Accelerators Spectrometers Detectors and Associated Equipment**, 2001. 467: 426-436.

[76] Carr, G.L., O. Chubar, and P. Dumas, Multichannel detection with a synchrotron light source: design and potential, in *Spectrochemical analysis using infrared multichannel detectors*, R. Bhargava and I. Levin, Editors. 2005, Ames, Iowa, Blackwell Pub.: 60.

[77] T. E. May, J. C. Bergstrom, L. O. Dallin, and D.R.T. Appadoo. *Coherent synchrotron radiation in the THz region at the CLS far infrared beamline.* in *33rd International Conference on Infrared, millimetre and Terahertz waves (IRMMW-THz).* 2008. Pasadena, CA 1-3

[78] May, T.E., Infrared facility at the Canadian Light Source. **Infrared Physics & Technology**, 2004. 45(5-6): 383-387.

[79] May, T., D. Appadoo, T. Ellis, and R. Reininger, Infrared Beamlines at the Canadian Light Source. **AIP Conference Proceedings**, 2007. 879(1): 579-582.

[80] Cutler, J., E. Hallin, M. de Jong, W. Thomlinson, and T. Ellis, The Canadian Light Source: The newest synchrotron in the Americas. **Nuclear Instruments**

& Methods in Physics Research Section a-Accelerators Spectrometers Detectors and Associated Equipment, 2007. 582(1): 11-13.

[81]   Bancroft, G.M., The Canadian Light Source - History and scientific prospects. **Canadian Journal of Chemistry-Revue Canadienne De Chimie**, 2004. 82(6): 1028-1042.

[82]   Nivellini, G., F. Tullini, A. Celli, and M. Becucci, Vibrational spectrum of 1,1,1-trifluoroethane. **Journal of the Chemical Society-Faraday Transactions**, 1998. 94(19): 2909-2912.

[83]   Predoi-Cross, A., A. Ibrahim, M. Herman, L. Fusina, G. Nivellini, and G. Di Lonardo, The high resolution infrared spectrum of the v4 band of 1,1,1-trifluoroethane. **Molecular Physics**, 2010. 108(18): 2303-2307.

[84]   Predoi-Cross, A., A. Ibrahim, and B. Billinghurst, *Spectroscopic Study of the v4 Band of CH3CF3 Using Synchrotron Based Fourier Transform Spectra*, in *2009 Activity Report, Canadian Light Source Inc.* 2010: Saskatoon. 82-83.

[85]   McKellar, A.R.W., High-resolution infrared spectroscopy with synchrotron sources. **Journal of Molecular Spectroscopy**, 2010. 262(1): 1-10.

[86]   Predoi-Cross, A., A. Ibrahim, A. Wismath, P.M. Teillet, V.M. Devi, D.C. Benner, and B. Billinghurst, Carbon Dioxide Line Shapes for Atmospheric Remote Sensing. **AIP Conference Proceedings**, 2010. 1214(1): 100-102.

[87]   Predoi-Cross, A., A. Ibrahim, and B. Billinghurst, *Spectroscopic Studies of Atmospheric Constituents Enabled by Synchrotron Techniques*, in *2008 Activity Report, Canadian Light Source Inc.* 2009: Saskatoon. 88-89.

[88]   Sheppard, N., The Historical Development of Experimental Techniques in Vibrational Spectroscopy, in *Handbook of vibrational spectroscopy*, P.R. Griffiths, Editor. 2002, New York, J. Wiley: 1-2.

[89]   Hirschfeld, T. and A.W. Mantz, Elimination of Thin-Film Infrared Channel Spectra in Fourier-Transform Infrared Spectroscopy. **Applied Spectroscopy**, 1976. 30(5): 552-553.

[90]   Hirschfeld, T., New Trends in Application of Fourier-Transform Infrared Spectroscopy to Analytical-Chemistry. **Applied Optics**, 1978. 17(9): 1400-1412.

[91]   Mellau, G.C. and B.P. Winnewisser, A method to remove fringing from FT-IR spectra. **Laboratory and Astronomical High Resolution Spectra**, 1995. 81: 138-139

[92]   Atakan, A.K., W.E. Blass, and D.E. Jennings, Elimination of Baseline Variations from a Recorded Spectrum by Ultralow Frequency Filtering. **Applied Spectroscopy**, 1980. 34(3): 369-372.

[93]   Faggin, M.F. and M.A. Hines, Improved algorithm for the suppression of interference fringe in absorption spectroscopy. **Review of Scientific Instruments**, 2004. 75(11): 4547-4553.

[94]   Naylor, D.A., A.A. Schultz, and T.A. Clark, Eliminating Channel Spectra in Fourier-Transform Spectroscopy. **Applied Optics**, 1988. 27(12): 2603-2607.

[95]   Pistorius, A.M.A. and W.J. DeGrip, Deconvolution as a tool to remove fringes from an FT-IR spectrum. **Vibrational Spectroscopy**, 2004. 36(1): 89-95.

[96]   Benner, D.C., C.P. Rinsland, V.M. Devi, M.A.H. Smith, and D. Atkins, A Multispectrum Nonlinear Least-Squares Fitting Technique. **Journal of Quantitative Spectroscopy & Radiative Transfer**, 1995. 53(6): 705-721.

[97]   Smith, M.A.H., D.C. Benner, A. Predoi-Cross, and V.M. Devi, Multispectrum analysis of (CH4)-C-12 in the nu(4) band: I. Air-broadened half widths, pressure-induced shifts, temperature dependences and line mixing. **Journal of Quantitative Spectroscopy & Radiative Transfer**, 2009. 110(9-10): 639-653.

[98]   Niple, E., W.G. Mankin, A. Goldman, D.G. Murcray, and F.J. Murcray, Stratospheric NO2 and H2O mixing ratio profiles from high resolution infrared solar spectra using nonlinear least squares. **Geophys. Res. Lett.**, 1980. 7(7): 489-492.

[99]   Max, J.-J. and C. Chapados, How to Deal with Some Spurious Fringes in Fourier Transform Infrared Spectrometers. **Applied Spectroscopy** 2008. 62(10): 1167-1171.

[100]   Devi, V.M., D.C. Benner, L.R. Brown, C.E. Miller, and R.A. Toth, Line mixing and speed dependence in CO2 at 6227.9 cm(-1) Constrained multispectrum analysis of intensities and line shapes in the 30013 <- 00001 band. **Journal of Molecular Spectroscopy**, 2007. 245(1): 52-80.

[101]   Churchill, W., *Thoughts and adventures*. 1932, London, Butterworth: 313.

[102]   Johns, J.W.C. and M. Noel, Absolute Intensities in Co2 - the Laser Bands near 10-Mu-M. **Journal of Molecular Spectroscopy**, 1992. 156(2): 403-414.

[103] Fischer, H., MIPAS experiment aboard ENVISAT, in *Observing Systems for Atmospheric Composition*, G. Visconti, et al., Editors. 2007, Springer New York: 71-81.

[104] Reid, J. and K. Siemsen, New Co2-Laser Bands in 9-11-Mum Wavelength Region. **Applied Physics Letters**, 1976. 29(4): 250-251.

[105] Dana, V., J.Y. Mandin, G. Guelachvili, Q. Kou, M. Morillonchapey, R.B. Wattson, and L.S. Rothman, Intensities and Self-Broadening Coefficients of (Co2)-C-12-O-16 Lines in the Laser Band Region. **Journal of Molecular Spectroscopy**, 1992. 152(2): 328-341.

[106] Devi, V.M., D.C. Benner, M.A.H. Smith, L.R. Brown, and M. Dulick, Multispectrum analysis of pressure broadening and pressure shift coefficients in the (CO2)-C-12-O-16 and (CO2)-C-13-O-16 laser bands. **Journal of Quantitative Spectroscopy & Radiative Transfer**, 2003. 76(3-4): 411-434.

[107] Devi, V.M., D.C. Benner, M.A.H. Smith, L.R. Brown, and M. Dulick, Absolute intensity measurements of the (CO2)-C-12-O-16 laser bands near 10 mu m. **Journal of Quantitative Spectroscopy & Radiative Transfer**, 2003. 76(3-4): 393-410.

[108] Olson, W.B., A.G. Maki, and W.J. Lafferty, Tables of N2O absorption lines for the calibration of tunable infrared lasers from 522 cm-1 to 657 cm-1 and from 1115 cm-1 to 1340 cm-1. **Journal of Physical and Chemical Reference Data**, 1981. 10(4): 1065-1084.

[109] Toth, R.A., Line Strengths of N2o in the 1120-1440-Cm-1 Region. **Applied Optics**, 1984. 23(11): 1825-1834.

[110] Smith, M.A.H., C.P. Rinsland, B. Fridovich, and K.N. Rao, Intensities and collision broadening parametes from infrared spectra, in *Molecular spectroscopy: modern research*, K.N. Rao and C.W. Mathews, Editors. 1972, New York, Academic Press: 111-143.

[111] Smith, M.A.H., C.P. Rinsland, V.M. Devi, L.S. Rothman, and K.N. Rao, Intensities and collision broadening parameters from infrared spectra: an update, in *Spectroscopy of the Earth's atmosphere and interstellar medium*, K.N. Rao and A. Weber, Editors. 1992, Boston, Academic Press: xi, 526 p.

[112] Devi, V.M., D.C. Benner, M.A.H. Smith, and C.P. Rinsland, Air- and N-2-broadening coefficients and pressure-shift coefficients in the (CO2)-C-12-O-16 laser bands. **Journal of Quantitative Spectroscopy & Radiative Transfer**, 1998. 59(3-5): 137-149.

Appendices

In the following appendices, the block diagrams for the LabVIEW programs used in this thesis are listed. Block diagrams are the equivalent of the program code in the LabVIEW language. LabVIEW is a graphical programming language, which instead of routines and functions has icons, while data are connected between them by wires, in a fashion similar to schematic diagrams.

In order to control the data flow in LabVIEW, many programmers rely largely on what are called structures. The structures in LabVIEW are frames in the block diagram that control the execution of the commands within its area according to a sequence or condition. Both sequence and condition structures are used in the thesis programs. Every sequence or conditional structure contains multiple frames; these frames are printed separately to show its programming code as in Appendix A. Appendix A contains the main program followed by all structure frames contained in this program in the following pages.

Another approach used to control LabVIEW data is to use subprograms performing specific routines in larger programs. These subprograms are either written by the programmer (customized) or a LabVIEW library is used. Appendix B has a program that contains many subprograms (called subVI in LabVIEW). The block diagram of each subprogram used in the main program in Appendix B is listed in Appendices B1 to B6.   Appendix C contains the program used to calculate SNR of the spectra to compare the effectiveness of each handling technique.
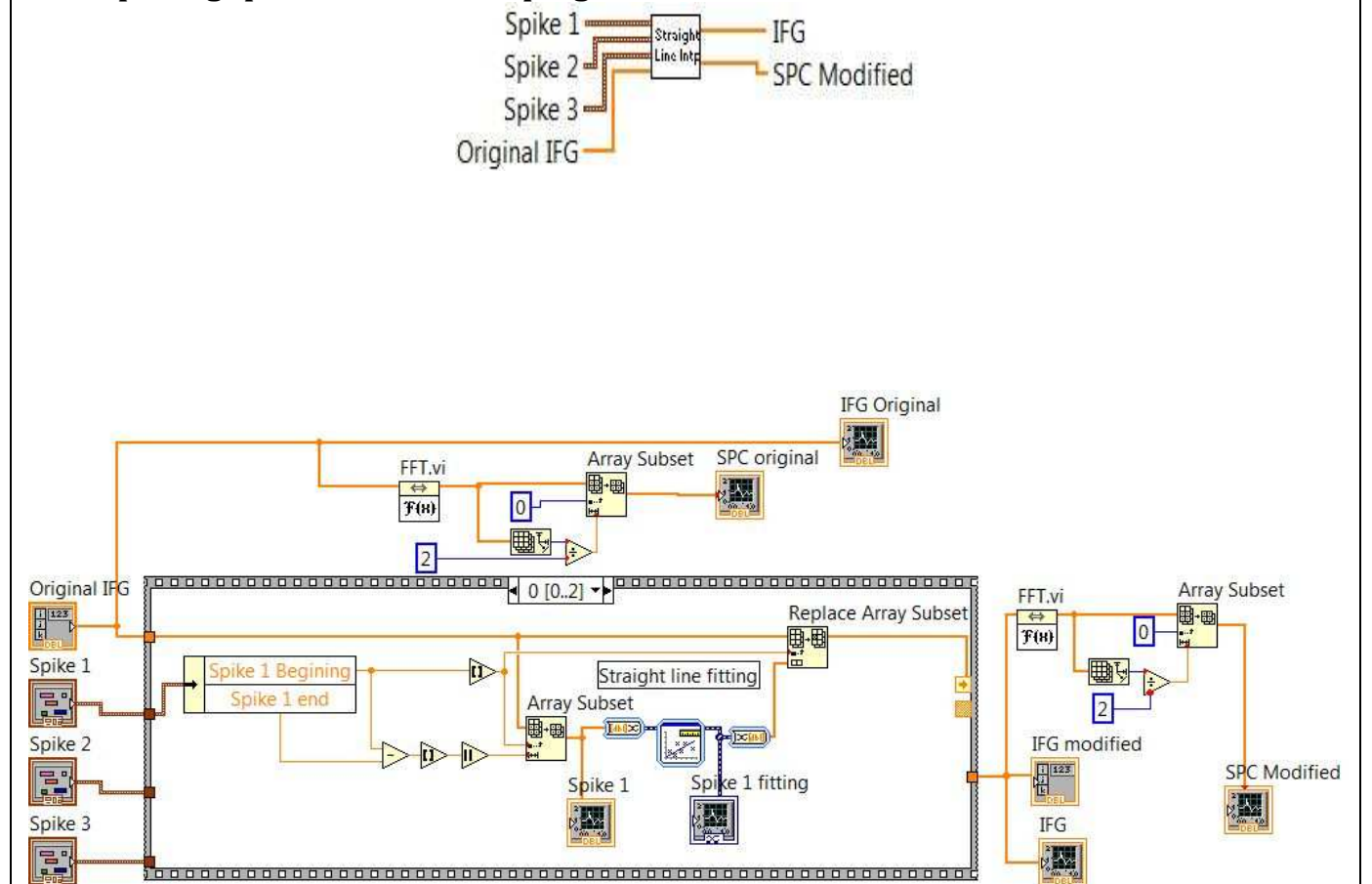
Appendix A: Spectral channel analysis program.
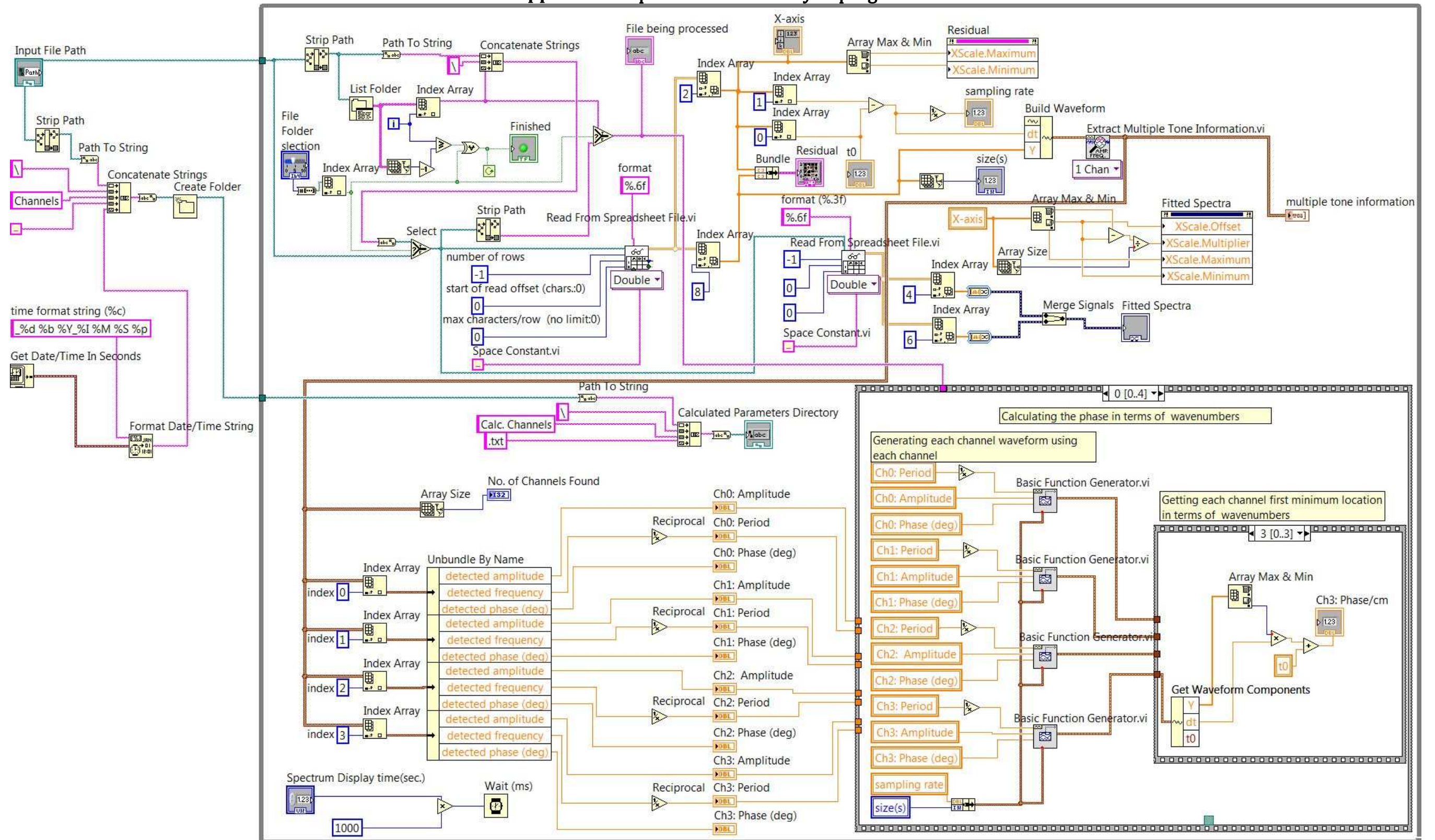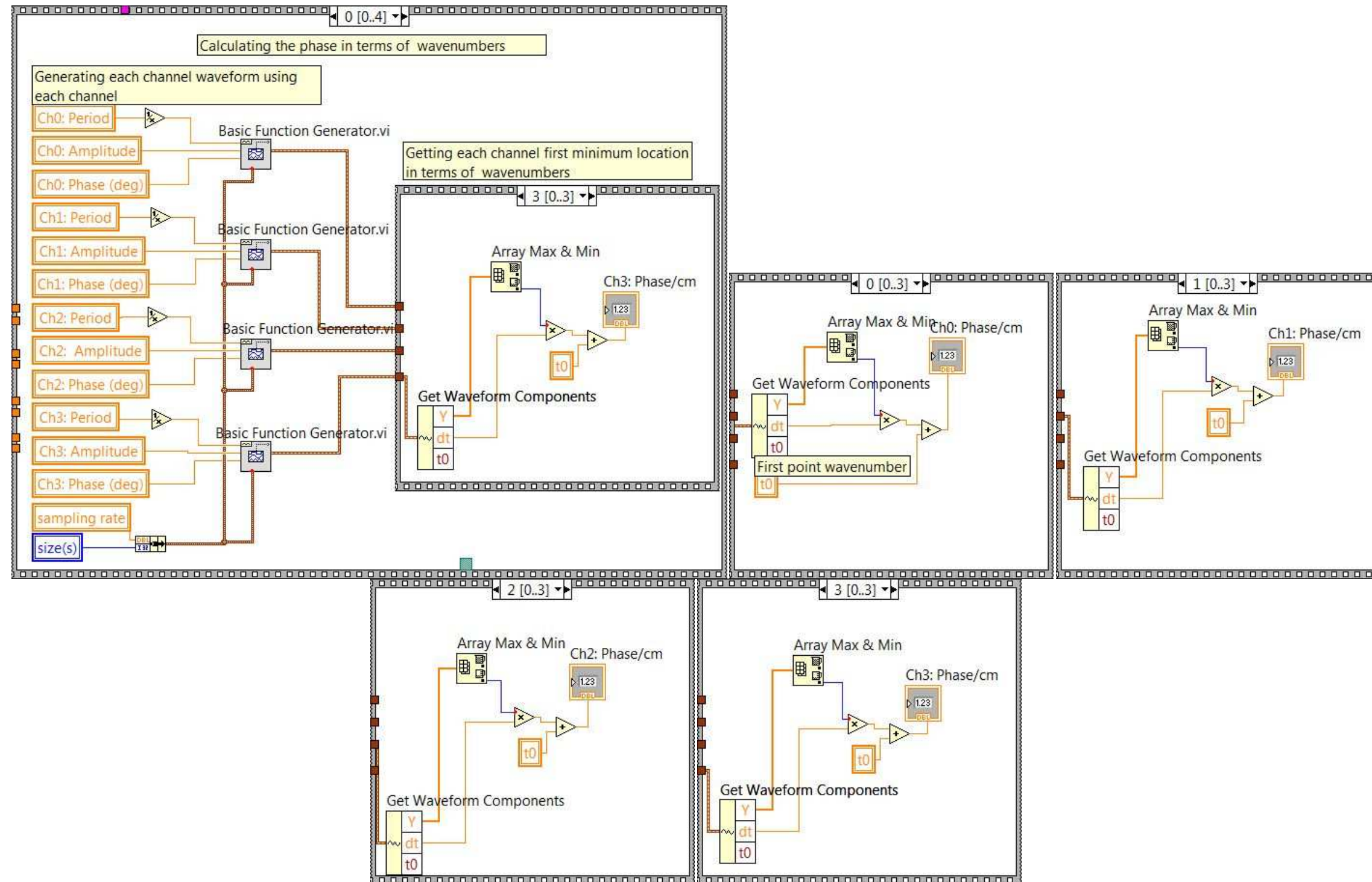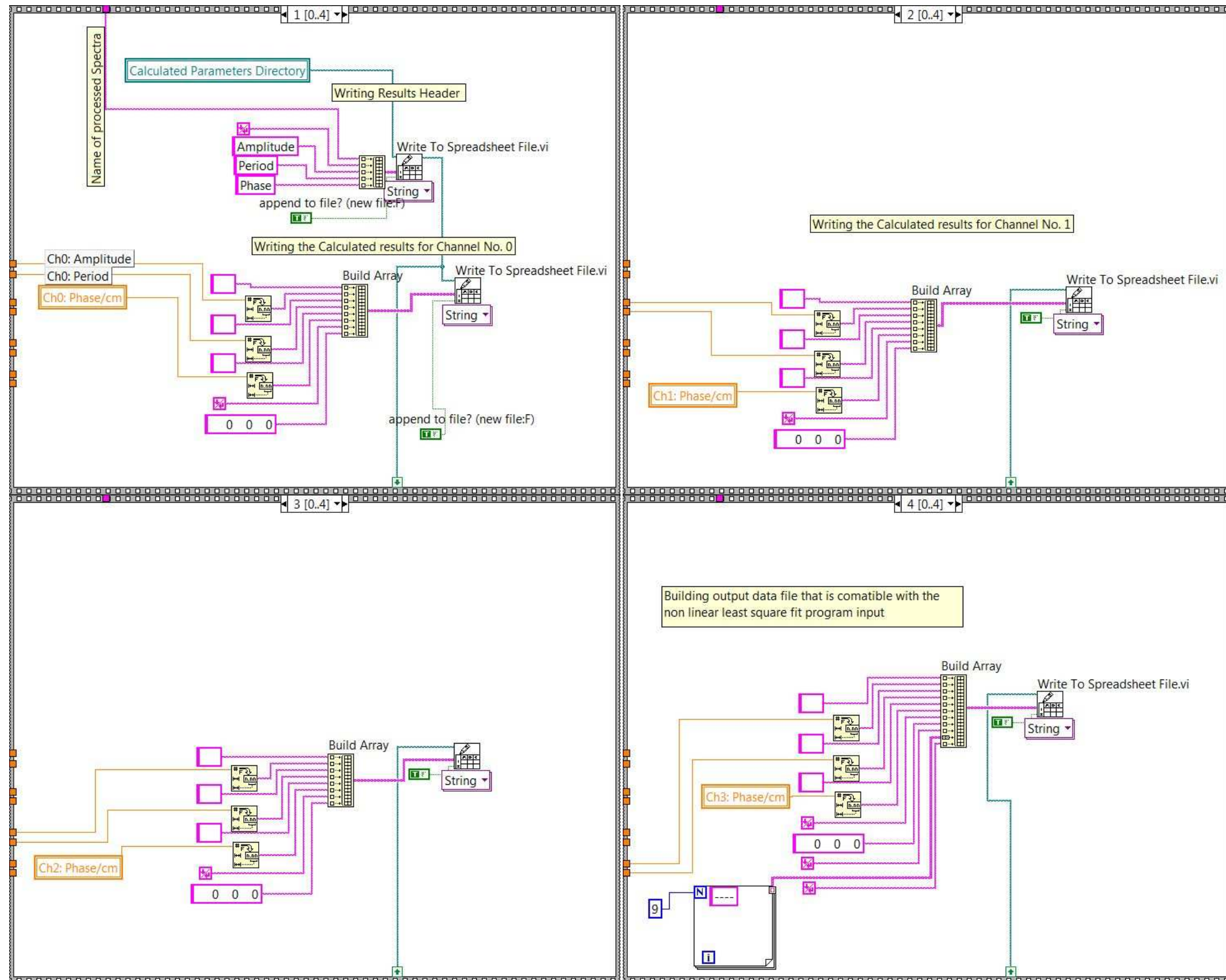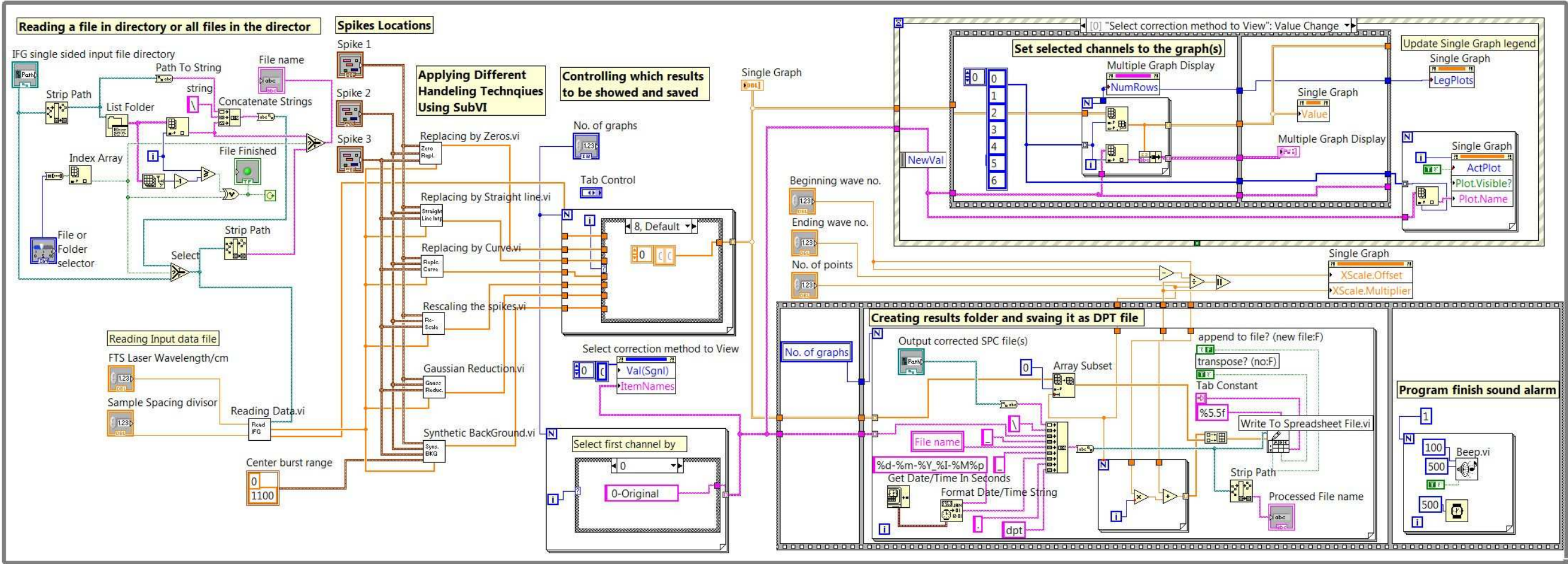
B1: Replacing spike with zeros subprogram[32,33]
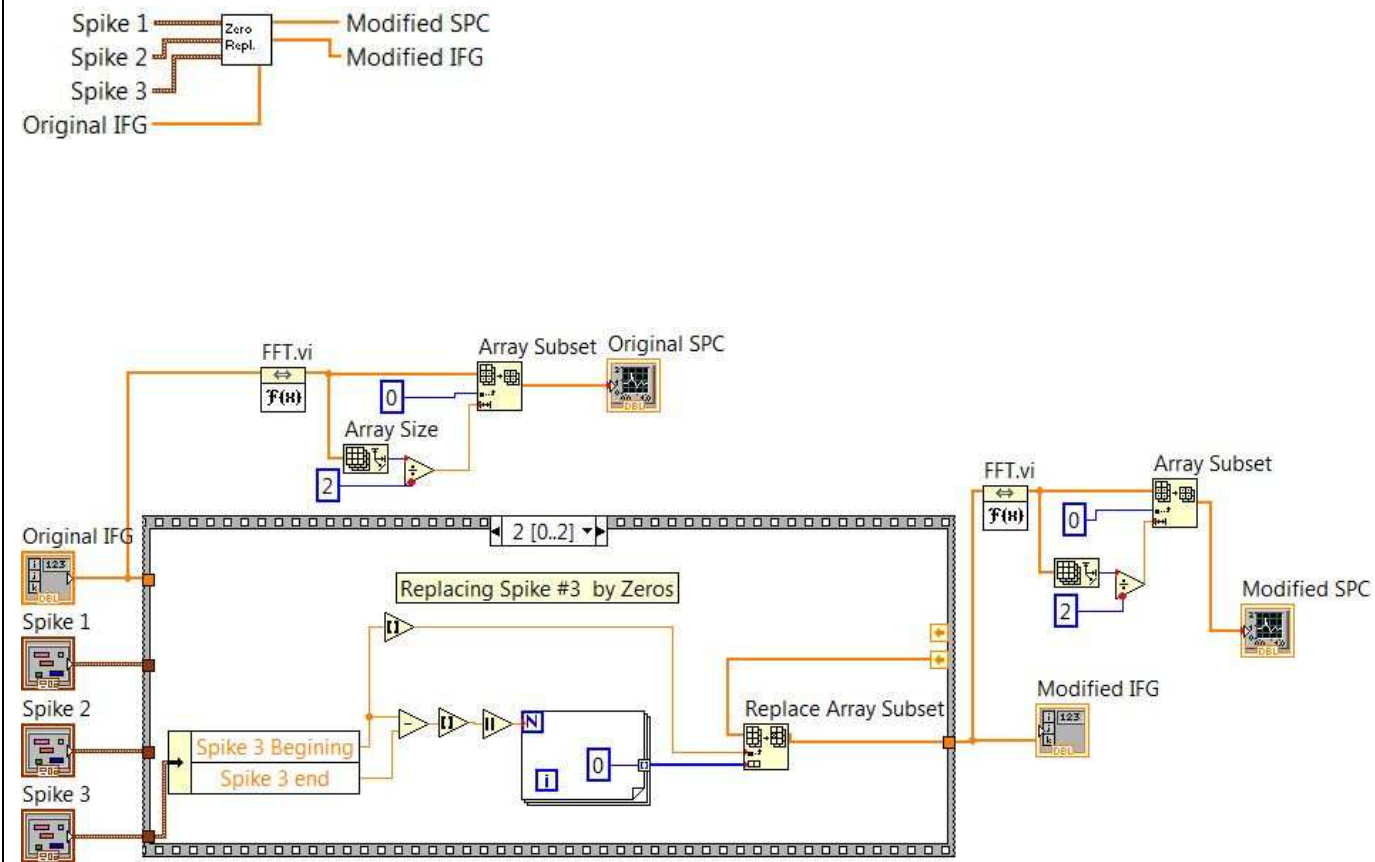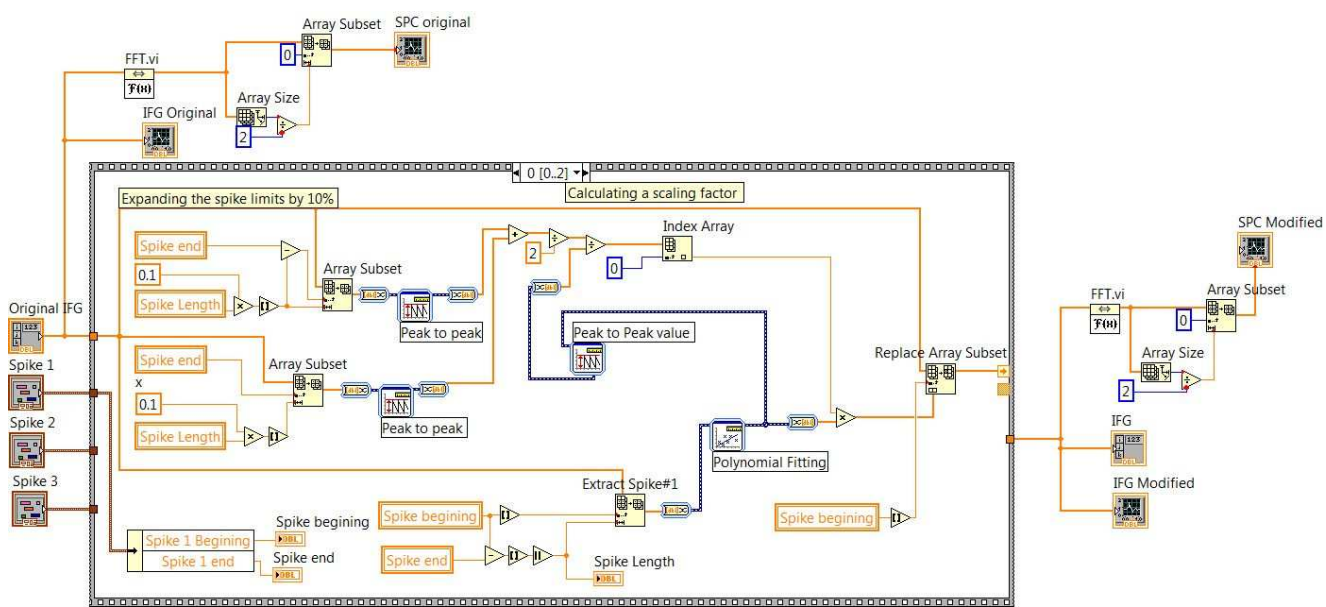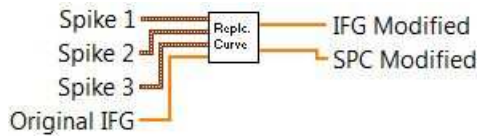

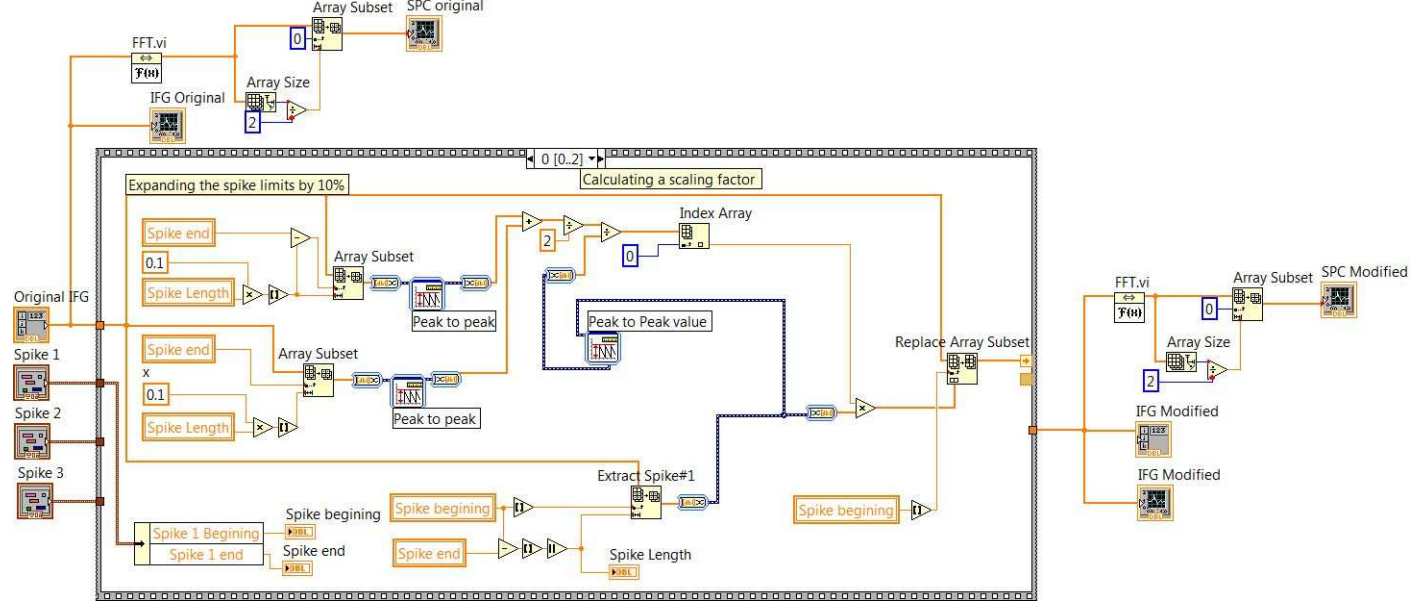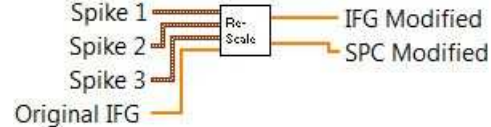**B2: Replacing spike with zeros subprogram**

---

[32] Subprogram and SubVI have the same meaning and are used interchangeably

[33] Only the first sequence structure handling the first spike is shown since the others are basically the same program.
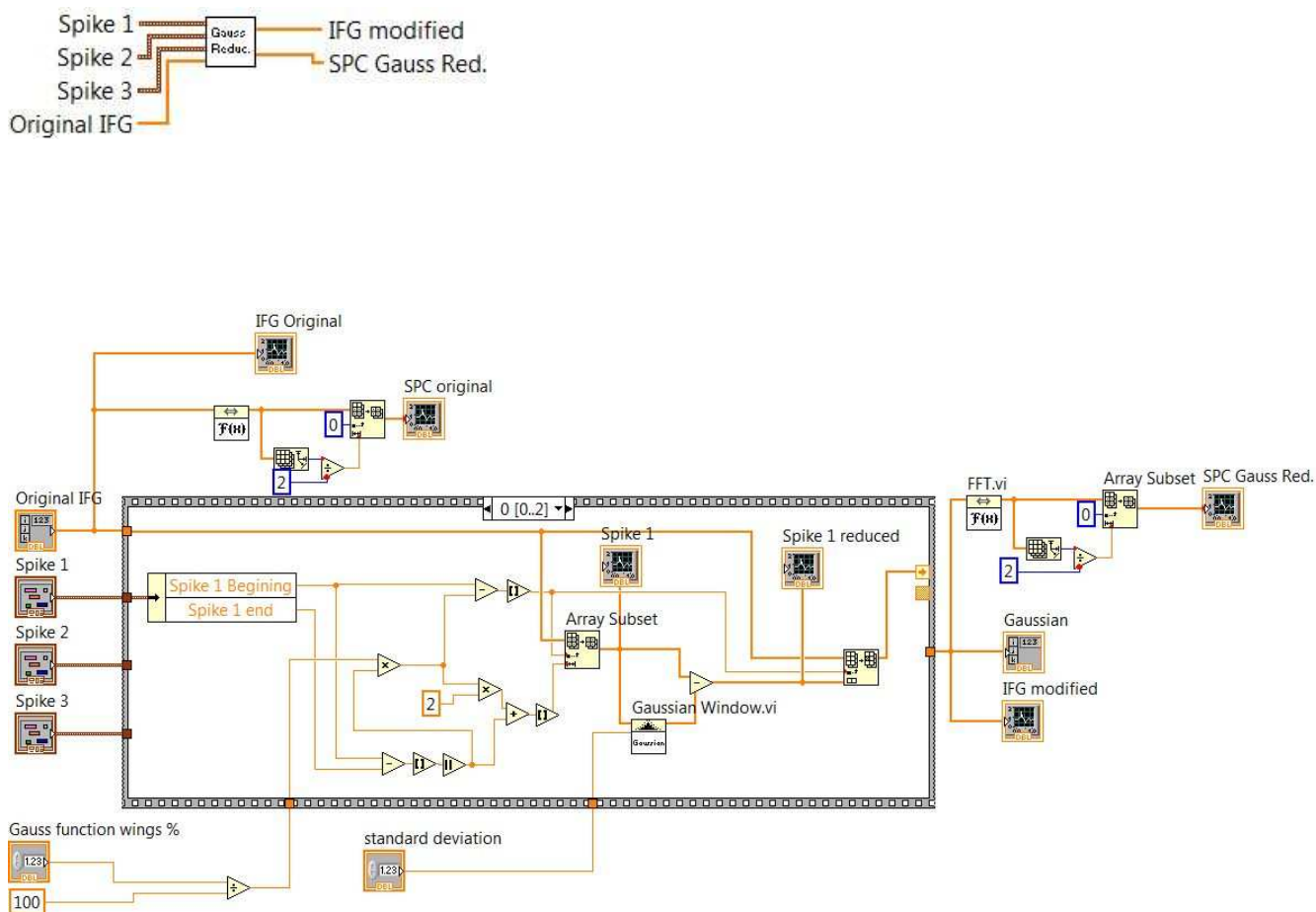
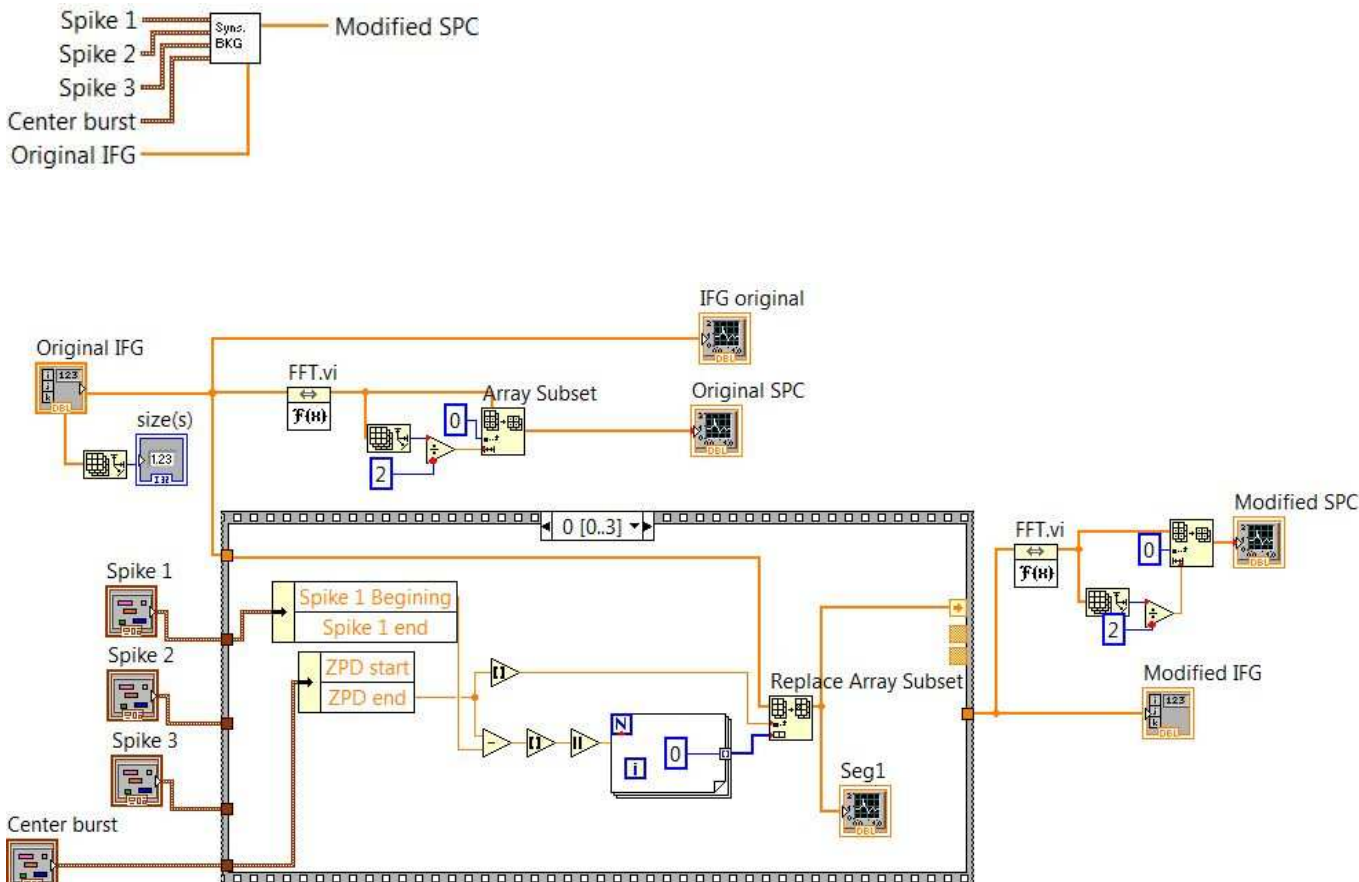**B3: Replacing spikes with polynomial curve subprogram**
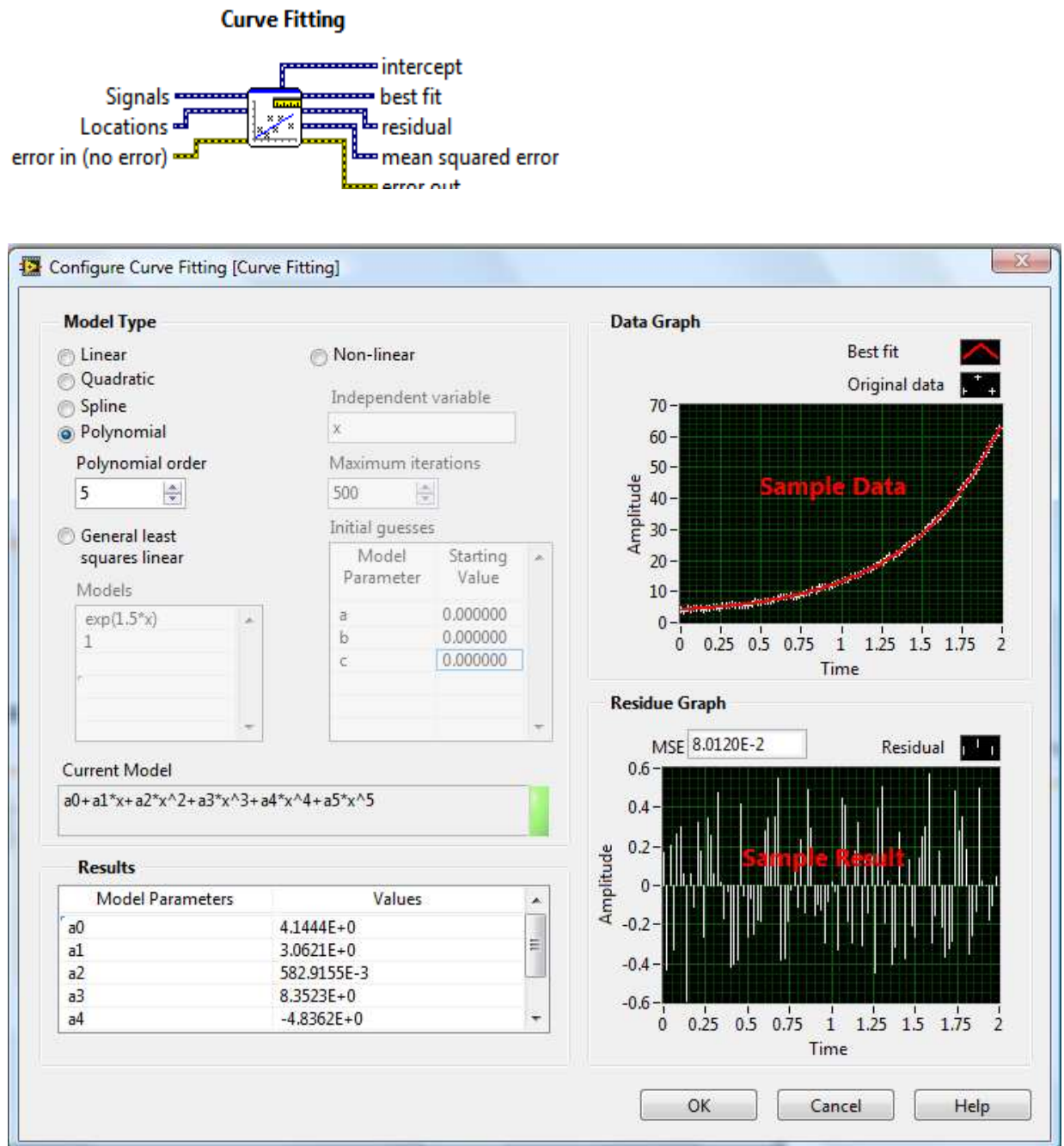

B4: Rescaling spikes subprogram

B5: Reducing spikes by Gauss function

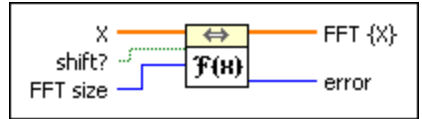**B6: Producing synthetic background spectrum subprogram**

B7: LabVIEW built in subprogram

Computes the coefficients that best represent the input data based on the chosen model type

FFT .vi

Computes the fast Fourier transform (FFT) of the input sequence **X**. The data type you wire to the **X** input determines the polymorphic instance to use.

Gaussian Window.vi

Applies an asymmetrical Gaussian window to the input sequence **X**. The data type you wire to the **X** input determines the polymorphic instance to use.

Write To Spreadsheet File.vi
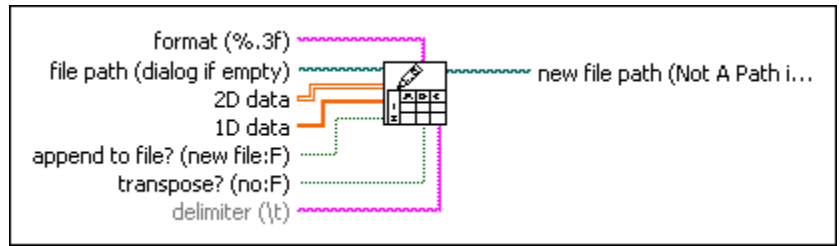
Converts a 2D or 1D array of strings, signed integers, or double-precision numbers to a text string and writes the string to a new byte stream file or appends the string to an existing file. The data type you wire to the **2D data** input or **1D data** input determines the polymorphic instance to use.